

# UNIVERSITÉ PARIS-SUD

ECOLE DOCTORALE 534 :  
MODELISATION ET INSTRUMENTATION EN PHYSIQUE,  
ENERGIES, GEOSCIENCES ET ENVIRONNEMENT  
LABORATOIRE: INSTITUT DE PHYSIQUE NUCLÉAIRE

DISCIPLINE : PHYSIQUE

## THÈSE DE DOCTORAT

Soutenue le 23 Septembre 2014 par

# Binsong Ma

## Simulation of electromagnetic channels for PANDA@FAIR

<b>Directrice de thèse :</b>	Mme Béatrice RAMSTEIN	Institut de Physique Nucléaire (Orsay)
<b>Co-directeur de thèse :</b>	M. Ermias ATOMSSA	Institut de Physique Nucléaire (Orsay)
<b>Composition du jury :</b>		
Président du jury :	M. Michel GUIDAL	Institut de Physique Nucléaire (Orsay)
Rapporteurs :	M. Eric VOUTIER	LPSC(Grenoble)
	M. Piotr SALABURA	Université Jagellonne (Cracovie)
Examineurs :	M. Stefano SPATARO	Universita degli studi (Torino)
	M. Kirill SEMENOV-TYAN-SHANSKIY	Institut d'Astrophysique et de Géophysique (Liège)

# Acknowledgment

Before all the aspects of my thesis, the physics, the experiment, the jobs... I will say thank you to all of you.

First of all, I would like to thank Mr. Faïçal Azaies and Mr. Fadi Ibrahim for welcoming me to a nice laboratory where I have spent three grateful years.

Then I would like to express my deepest and sincerest thanks to my supervisor Mrs. Béatrice Ramstein. During the past three years, her patient guide for my thesis works and kindly care for my daily life allow me to complete my PHD thesis easier. I have learned from her a serious attitude to the scientific research. Without her help and advice, this thesis will not have been finished as it looks like now.

The members of the PANDA and HADES groups have contributed immensely to my personal and professional time at IPN d'Orsay. The group has been a source of friendships as well as good advice and collaboration. Thierry, your wide knowledge and logical way of thinking are very helpful for me, during our discussion. Ermias, even we have worked together no more than one year, I have learned a lot from you, your deep knowledge of physics, your high capability of coding and so on. Jacques and Saro, thanks for giving me many helps in the physics. Dominique, Egle, Alaa, Gosia and Huber, thank you all for your helps in my works and life.

I will also thank to the Torino and Pavia groups for welcoming me each time I came to Italy. Special thanks to Stefano for the friendly collaboration and great help in the computing.

Kirill, thanks very much for your patient help in my work of TDA studies.

To my friends, Chengjun, Yingtao, Kunliang, Bo, Fei, ... .., thanks for the nice time with you in France.

Lastly, I would like to thank my family for all their love and encouragement, for my parents who raised me with a love of science and supported me in all my pursuits.

---

# Contents

<b>1</b>	<b>Introduction</b>	<b>1</b>
<b>2</b>	<b>FAIR and <math>\bar{\text{P}}\text{ANDA}</math></b>	<b>5</b>
2.1	Facility for Antiproton and Ion Research . . . . .	5
2.2	The scientific goal of $\bar{\text{P}}\text{ANDA}$ . . . . .	7
2.3	$\bar{\text{P}}\text{ANDA}$ set up . . . . .	9
2.3.1	Target spectrometer . . . . .	10
2.3.1.1	Target . . . . .	10
2.3.1.2	Magnet . . . . .	11
2.3.1.3	Tracking system . . . . .	11
2.3.1.4	Electromagnetic calorimeter . . . . .	14
2.3.1.5	Cerenkov detector . . . . .	16
2.3.1.6	Time of flight . . . . .	16
2.3.1.7	Muon detector . . . . .	17
2.3.2	Forward spectrometer . . . . .	17
2.3.2.1	Forward tracker . . . . .	17
2.3.2.2	Forward Cerenkov and TOF Detectors . . . . .	18
2.3.2.3	Forward calorimeter . . . . .	18
2.3.2.4	Forward muon system . . . . .	18
2.3.3	Luminosity detector . . . . .	18
2.3.4	Data acquisition and trigger . . . . .	18
<b>3</b>	<b>Electromagnetic channels for nucleon structure studies with <math>\text{PANDA}</math></b>	<b>21</b>
3.1	Different observables accessible with $\text{PANDA}$ . . . . .	21
3.2	Electromagnetic form factors of proton . . . . .	23
3.2.1	Kinematics . . . . .	23
3.2.2	General properties of the proton form factors . . . . .	23
3.2.3	Asymptotic behaviour . . . . .	25
3.2.4	Proton electromagnetic form factors in the Space-Like region. . . . .	25
3.2.4.1	Rosenbluth method . . . . .	25
3.2.4.2	Polarization transfer experiment . . . . .	26
3.2.4.3	Two-photon contribution . . . . .	27
3.2.4.4	Proton charge radius . . . . .	28
3.2.5	Proton electromagnetic form factors in the Time-Like region . . . . .	28
3.2.5.1	Experimental access to the Time-Like form factors . . . . .	28
3.2.5.2	Existing data . . . . .	29
3.2.6	Time-Like proton form factors with $\bar{\text{P}}\text{ANDA}$ . . . . .	30
3.3	Transition Distribution Amplitudes . . . . .	31

---

3.3.1	Definition . . . . .	31
3.3.2	Factorization approach and experimental access to TDAs . . . . .	33
3.3.3	Mathematical description of TDA . . . . .	34
3.3.4	Predictions from TDA models for different reactions . . . . .	35
3.3.5	Feasibility study of the TDA measurement in the $\bar{p}p \rightarrow e^+e^-\pi^0$ for $\bar{P}$ PANDA . . . . .	37
<b>4</b>	<b>Simulation and Reconstruction</b> . . . . .	<b>39</b>
4.1	Simulation tools . . . . .	39
4.1.1	External packages . . . . .	40
4.1.2	PandaRoot main code . . . . .	40
4.2	Simulation steps . . . . .	40
4.2.1	Event generation . . . . .	41
4.2.2	Physics lists from GEANT . . . . .	41
4.2.3	Digitization . . . . .	42
4.2.3.1	MVD readout . . . . .	42
4.2.3.2	STT readout . . . . .	43
4.2.3.3	GEM readout . . . . .	44
4.2.3.4	DIRC detectors readout . . . . .	44
4.2.3.5	EMC readout . . . . .	44
4.2.4	Reconstruction . . . . .	45
4.2.4.1	Charged particle tracking . . . . .	45
4.2.4.2	Cluster reconstruction EMC . . . . .	50
4.2.5	Particle identification . . . . .	52
4.2.5.1	dE/dx measurement in STT and MVD . . . . .	52
4.2.5.2	PID in DIRC . . . . .	53
4.2.5.3	PID in EMC . . . . .	53
4.2.5.4	Global PID . . . . .	57
4.3	Tracking acceptance and efficiency studies . . . . .	57
4.3.1	STT acceptance . . . . .	58
4.3.2	Track finder purity study . . . . .	59
4.3.3	Tracking efficiency . . . . .	60
4.4	Conclusion . . . . .	62
<b>5</b>	<b>Electron bremsstrahlung correction method</b> . . . . .	<b>63</b>
5.1	Electron momentum reconstruction in the PANDA central tracking system . . . . .	63
5.1.1	Bremsstrahlung effect in the PANDA central tracking system . . . . .	64
5.1.1.1	Bremsstrahlung description in Geant . . . . .	64
5.1.1.2	Material budget in the central tracker . . . . .	64
5.1.1.3	Electron energy loss . . . . .	65
5.1.1.4	Bremsstrahlung photon angular distributions . . . . .	66
5.1.1.5	Photon multiplicities . . . . .	66
5.1.1.6	Photon emission point . . . . .	67
5.1.2	Electron tracking resolution . . . . .	67
5.1.2.1	General results . . . . .	67
5.1.2.2	The influence of bremsstrahlung emission point . . . . .	70
5.1.2.3	Comparison of reconstructed momentum and momentum after photon emission . . . . .	70
5.1.3	The problem of bremsstrahlung treatment in the Kalman filter . . . . .	71
5.2	Electron bremsstrahlung correction method . . . . .	71

5.2.1	General idea . . . . .	72
5.2.2	Description of the method . . . . .	72
5.2.2.1	First step: separated photon and electron Bumps . . . . .	73
5.2.2.2	Second step: merged photon and electron Bumps . . . . .	74
5.2.3	Implementation of the method in PANDARoot . . . . .	76
5.3	Result of the correction method . . . . .	77
5.3.1	Electron momentum resolution after using the correction method . . . . .	77
5.3.2	Efficiency and purity of the bremsstrahlung photon reconstruction . . . . .	82
5.3.3	Limitations of the method . . . . .	83
5.4	Applications of the new method for different electromagnetic channels . . . . .	85
5.5	Conclusion . . . . .	85
<b>6</b>	<b>Feasibility studies of <math>\pi</math>-N TDAs for PANDA experiment</b>	<b>87</b>
6.1	The $\pi$ -N TDA in the $\bar{p} \rightarrow J/\Psi\pi^0$ reaction . . . . .	87
6.1.1	The model . . . . .	87
6.1.2	Cross section estimation . . . . .	89
6.1.2.1	Numerical results . . . . .	89
6.1.2.2	Comparison with the data . . . . .	89
6.1.3	Alternative models . . . . .	90
6.2	Feasibility study for $\bar{P}$ ANDA . . . . .	91
6.2.1	Event generator . . . . .	91
6.2.2	Counting rate study . . . . .	93
6.2.3	Kinematics consideration . . . . .	94
6.2.4	Effect of bremsstrahlung correction method on the signal detection . . . . .	95
6.2.5	Background consideration . . . . .	97
6.2.5.1	Total cross section of the $\pi^+\pi^-\pi^0$ background . . . . .	97
6.2.5.2	Reconstruction efficiency . . . . .	97
6.2.5.3	PID efficiency . . . . .	98
6.2.5.4	Effect of the $e^+e^-$ invariant mass cut . . . . .	99
6.2.5.5	Numerical application . . . . .	101
6.2.5.6	Angular distribution . . . . .	101
6.3	Conclusion . . . . .	101
<b>7</b>	<b>Conclusions and outlook</b>	<b>103</b>
<b>8</b>	<b>Abstract</b>	<b>111</b>
<b>9</b>	<b>Résumé</b>	<b>113</b>



---

# Chapter 1

## Introduction

Being the constituents of the atomic nuclei, nucleons play a fundamental role in the structure of the matter. About 99% of the mass of the visible matter is due to the nucleons. The proton was discovered in 1919 by E. Rutherford [1] and the neutron in 1932 by Chadwick [2]. The first evidence of the proton internal structure was given by the measurement of the magnetic moment of the proton in 1933, by O. Stern [3] which was found to be 2.8 times larger than expected for a spin 1/2, point-like particle. Twenty years later, the elastic electron proton scattering experiments at the Stanford High Energy Physics Laboratory by Hofstadter and collaborators [4, 5] opened the way for an investigation of the electromagnetic structure of the nucleon at different energy scales, by measuring the electromagnetic form factors, a field which is today still very active.

The quark model, developed in 1964 by M. Gell-Mann [6] and G. Zweig [7], provided a framework to classify the hadrons (i.e. all particles undergoing the strong interaction). It put forward a picture of the proton as made of three particles, the valence quarks. A more dynamical picture was provided a few years later by the parton model [8, 9] where the nucleon, and more generally the hadron is made of point-like constituents (quarks and gluons) with a description depending on the scale  $1/Q^2$  at which the nucleon is probed (fig. 1.1).

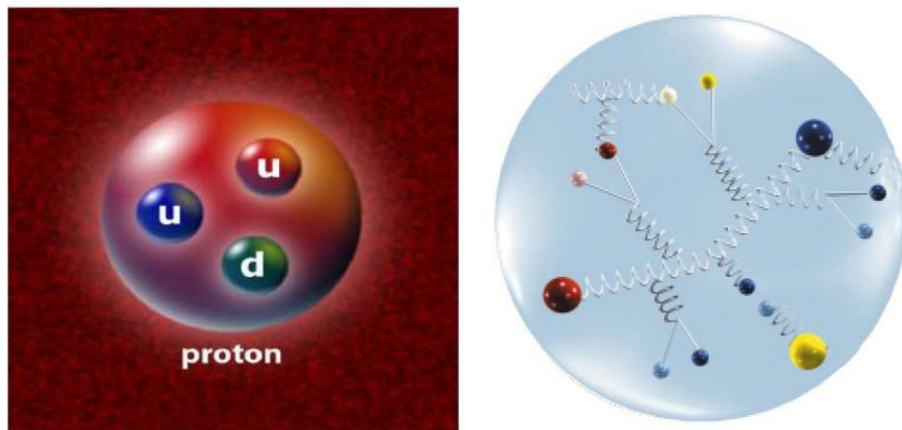


Figure 1.1: Schematic picture of a nucleon in the quark model (left) and parton model (right).

The understanding of the nucleon structure, in terms of strongly interacting quarks and gluons, is still the central question of the modern hadronic physics. The fundamental theory

---

## Strong interaction coupling constant

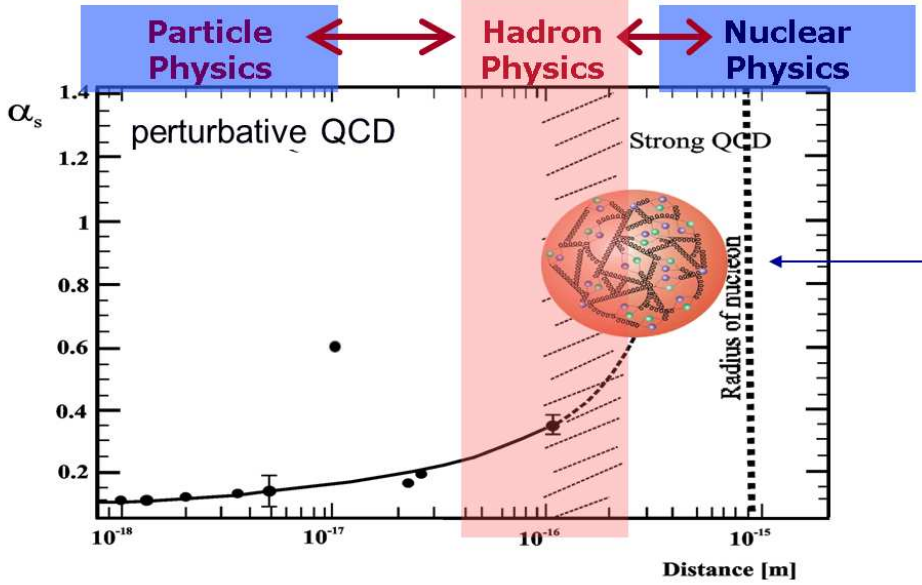


Figure 1.2: Dependence of the strong coupling constant  $\alpha_s$  as a function of the distance between partons illustrating the perturbative QCD regime and the strong coupling regime.

that describes the strong interaction is the Quantum Chromodynamics (QCD), the quantum field theory of interacting quarks and gluons. Together with the electroweak theory, QCD forms the standard model of particle physics. One particularity of QCD, which makes a fundamental difference with QED, consists in the fact that gluons carry color charge and therefore interact among themselves. As shown in fig 1.2, the interaction is strong and attractive at large distances. More precisely, the coupling constant ( $\alpha_s$ ) decreases with  $Q^2$  as  $\sim 1/\log(Q^2/\Lambda^2)$ , where  $\Lambda \sim 200$  MeV is the QCD scale. Two fundamental manifestations of QCD are related to this property. The first is asymptotic freedom, i.e. the fact that partons have a weak interaction at very small distances. The second is confinement, which prevents partons to separate and to appear individually, as illustrated schematically in fig. 1.3. QCD is well tested at high energies, where the strong coupling constant is small and perturbation theory applies. In the low-energy regime, however, the coupling constant is large and perturbative calculations are no longer possible.

At the lowest energies, a very complex many-body problem has to be solved, due to the presence of gluons and quark and anti-quark pairs, in addition to the three valence quarks. The ultimate challenge is a description of the nucleon in terms of its constituents, but this task is difficult. Indeed, in the non perturbative regime, it is very hard to make quantitative predictions starting from the QCD Lagrangian. Two ways of solving this problem are proposed by theoreticians: effective field theories or lattice QCD calculations. Besides, precise data, ranging from the low energy regime to the region where perturbative QCD holds, are needed to solve the still open questions.

The goal of the experimental hadronic physics is to provide measurements to improve the understanding of QCD manifestations in the non-perturbative regime. Information can be gained, by measuring nucleon properties at different scales, by investigating the spectrum of QCD states (baryons, mesons or new states of matter) or by studying reaction mechanisms.

The new FAIR (Facility for Antiproton and Ion research) in construction at Darmstadt

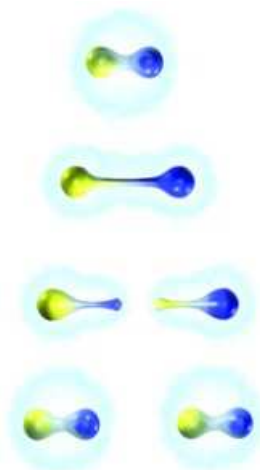


Figure 1.3: Illustration of the confinement: if energy is given to the quark-antiquark pair, they cannot be separated. Instead, the gluon field increases and new particles are created.

will provide high precision data in the field of hadronic physics. The  $\bar{\text{P}}\text{ANDA}$  (Antiproton ANnihilation at DArmastadt) will be installed on the High Energy Storage Ring (HESR) which will provide antiproton beams with momenta from 1.5 to 15 GeV/c. That experiment has a large experimental program, of which the study of the structure of the proton is one aspect. In particular, the structure of the proton can be explored in proton-antiproton annihilation into a lepton pair in a kinematical regime which is inaccessible with the electron-proton scattering experiments. The aim of this thesis is to provide simulation, reconstruction and analysis tools to prepare this experiment.

My work consisted in two main tasks:

- First, I worked on the improvement of the performance of electron reconstruction in  $\bar{\text{P}}\text{ANDARoot}$ , the simulation and analysis software of  $\bar{\text{P}}\text{ANDA}$ . The electromagnetic channels that contain information on the proton structure indeed need an optimized electron momentum resolution to reject the huge hadronic background. But there is a limitation due to the Bremsstrahlung effect in the detectors, which leads to a bad efficiency in signal selection. I developed a new method of Bremsstrahlung correction based on an event by event treatment and using the detection of Bremsstrahlung photon in electromagnetic calorimeter.
- The second part consists in a feasibility study of the measurement with  $\bar{\text{P}}\text{ANDA}$  of the  $\bar{p}p \rightarrow J/\Psi \pi^0$  ( $J/\Psi \rightarrow e^+e^-$ ) reaction which should give access to the  $\pi$ -N Transition Distribution Amplitudes (TDA). TDAs are universal non-perturbative objects describing the transition between two different particles. For instance, the  $\pi$ -N TDAs parametrize the pionic content of the nucleon wave function. My main task consisted in the design and implementation of a new event generator based on the theoretical model [10] in  $\bar{\text{P}}\text{ANDARoot}$ . I then provided counting rate estimates and started a background study which will be useful for a future experiment proposal.

The next chapter of this manuscript will be devoted to the description of the FAIR facility and the  $\bar{\text{P}}\text{ANDA}$  detector, including a presentation of the main scientific objectives of these projects.

Chapter 3 is devoted to an introduction to the concept of electromagnetic form factors and Transition Distribution Amplitudes. In Chapter 4, I will introduce the simulation and analysis framework of PANDA. I will insist on specific inputs which are crucial to perform realistic simulations. I will also give some results concerning acceptance and reconstruction efficiency. In Chapter 5, I explain the method I developed to improve the electron momentum reconstruction by measuring the Bremsstrahlung photon and present the results. Chapter 6 consists in a feasibility study of the  $\pi$ -N Transition Distribution Amplitude measurements in the  $\bar{p}p \rightarrow J/\Psi \pi^0$  ( $J/\Psi \rightarrow e^+e^-$ ) reaction. In chapter 7, I present a conclusion from this work and an outlook.

---

## Chapter 2

# FAIR and $\bar{P}$ ANDA

### 2.1 Facility for Antiproton and Ion Research

The Facility for Antiproton and Ion Research (FAIR, see figure 2.1) [11] which has been developed in cooperation with an international community of 45 countries and about 2500 scientists and engineers is under construction at Helmholtzzentrum für Schwerionenforschung (GSI) in Darmstadt (Germany).

The goal of this new facility is to provide Europe with a state of the art accelerator system for research in nuclear physics and connected fields [13] [14]. FAIR is designed to deliver primary beams of different ion species from Hydrogen to Uranium with energies up to a few tens of GeV per nucleon and, in the same range of energies, secondary beams including both rare-isotope nuclei and antiprotons with unprecedented quality and intensity.

This project will use the current upgraded accelerators available at GSI as injectors for the new installations. Once upgraded for high intensities, the existing GSI accelerators UNILAC (UNiversal Linear ACcelerator) and SIS18 (synchrotron with a maximum magnetic rigidity of 18 Tm) as well as a proton LINAC (to be built) will serve as pre-accelerators and injectors for the new complex. The heart of the FAIR facility is the SIS100 synchrotron [15] with a 1100 m circumference and with maximum magnetic rigidity of 100 Tm. Coupled with a cooler system and storage rings, the synchrotron will deliver high intensity and high energy beams from protons to heavy ions.

The SIS100 is designed to fulfill the requirement for very intense primary pulsed heavy ion and proton beams. The high bending power of magnets makes it possible to use ions with low charge state, thus reducing the space charge effects. At the same time, repetition rates of 1 Hz will be achieved and ramp rates up to 4 T/s will be used to maximize the number of particles per bunch. In this way, 1.5 GeV/nucleon  $U^{238+}$  beams can be accelerated with intensities of  $5 \cdot 10^{11}$  ions per pulse and 30 GeV protons with intensities reaching  $4 \cdot 10^{13}$  per pulse.

Antiprotons will be produced on a target bombarded system with 29 GeV/c proton beams. They will be collected and transferred in a Collector Ring (CR) to be accumulated and cooled down. Then they are injected at 3.8 GeV/c either in the High Energy Storage Ring (HESR) [16] which is used for high energy antiproton physics experiment like  $\bar{P}$ ANDA or in the New Experimental Storage Ring (NESR) [17]. The latter cools and decelerates stable and radioactive ions as well as antiprotons for low energy experiments and trap experiment at FLAIR (Facility for Low Antiproton and Ion physics). The HESR will be equipped with both stochastic and electron cooling to provide high luminosity and high resolution beams. It consists of two 180° arcs and two straight sections. The electron cooling is based on the Coulomb scattering with a monoenergetic electron beam, while stochastic cooling is based on electric field pulses triggered

---

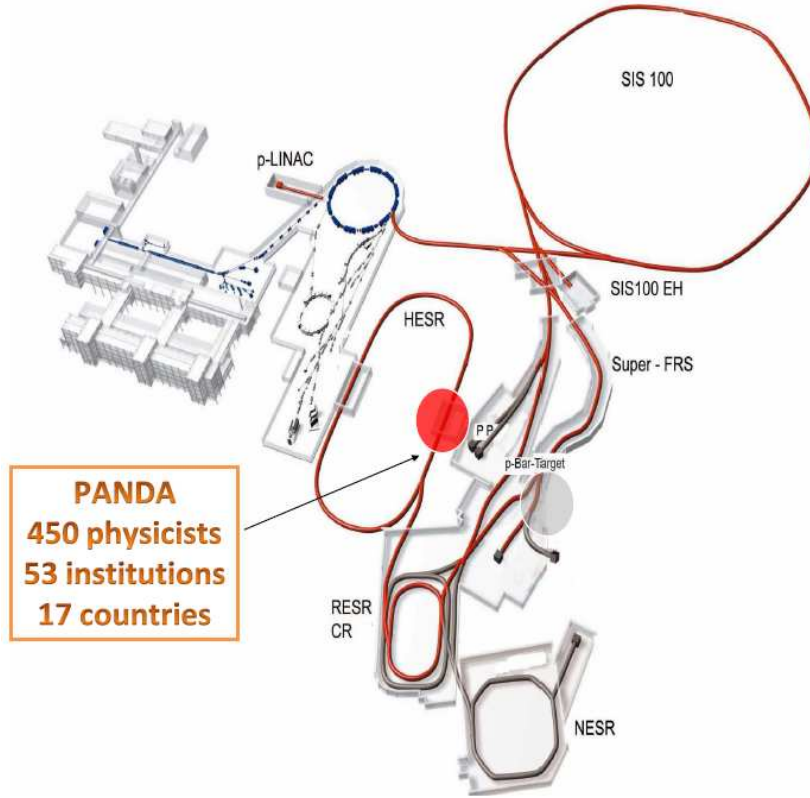


Figure 2.1: Facility for Antiproton and Ion Research (FAIR). Blue color stands for the existing GSI facility (UNILAC, SIS18, ESR). The planned FAIR facility is plotted in red color (SIS100/300 synchrotrons, the collector and accumulator rings CR and RESR respectively, the new experimental storage ring NESR, the rare isotope production target and the superconducting fragment separator Super-FRS, the proton linac, the antiproton production target and the high energy storage ring HESR). From [12].

by feedback loops. One straight section will be occupied by the  $\bar{\text{P}}\text{ANDA}$  detector investigating antiproton annihilation reactions from an internal hydrogen target [18] and the other one by the electron cooling (figure 2.2). Table 2.1 presents the specifications and the operating modes of the HESR.

The antiproton production rate is  $2 \cdot 10^7/\text{s}$ . After stochastic cooling in the CR ring and collection in the Recuperated Experimental Storage Ring (RESR) [19], the 3.8 GeV/c antiprotons are injected by bunches of  $10^{11}$  in the HESR. After pre-cooling, they are then accelerated or decelerated to the desired momentum. At the highest momenta, the main origin of luminosity loss during the cycle are the hadronic interactions in the target, which only slightly depend on the beam momentum, while at lower momenta, the Coulomb interaction contribution is also important. The combination of both effects yields beam lifetimes of the order of 30 mn at 1.5 GeV/c and 2h at 15 GeV/c.

Taking into account these losses, a luminosity of  $1.6 \cdot 10^{32} \text{ cm}^{-2} \text{ s}^{-1}$  averaged over one cycle in the storage ring can be obtained at 15 GeV/c, and  $0.7 \cdot 10^{32} \text{ cm}^{-2} \text{ s}^{-1}$  at 1.5 GeV/c, with a target thickness of  $4 \cdot 10^{15} \text{ atoms/cm}^2$ .

Electron cooling is provided for antiprotons up to 8 GeV and stochastic cooling between 3

HESR specifications	
Ion species	Antiprotons
$\bar{p}$ production rate	$2 \cdot 10^7 \text{ s}^{-1}$ ( $1.2 \cdot 10^{10}$ per 10 min)
Momentum range	1.5 to 15 GeV/c
HESR operation modes	
High resolution	Luminosity of $2 \cdot 10^{31} \text{ cm}^{-2} \text{ s}^{-1}$ for $10^{10} \bar{p}$ momentum spread $\sigma_p/p \leq 2 \cdot 10^{-5}$ 1.5 to 9 GeV/c, electron cooling up to 9 GeV/c
High luminosity	Luminosity of $2 \cdot 10^{32} \text{ cm}^{-2} \text{ s}^{-1}$ for $10^{11} \bar{p}$ momentum spread $\sigma_p/p \sim 10^{-4}$ 1.5 to 15 GeV/c, stochastic cooling above 3.8 GeV/c

Table 2.1: HESR specifications and operation modes

GeV and 14 GeV. Two different operation modes are foreseen for the HESR: the high intensity mode, which will provide a maximum luminosity of  $2 \cdot 10^{32} \text{ cm}^{-2} \text{ s}^{-1}$  with a beam momentum resolution  $\delta p/p$  of  $10^{-4}$  and the high resolution mode, limited to 8 GeV, using electron cooling to reach momentum precisions down to  $10^{-5}$ , with a maximum luminosity of  $2 \cdot 10^{31} \text{ cm}^{-2} \text{ s}^{-1}$ . However, since the funding of the RESR is not yet ensured,  $\bar{\text{P}}\text{ANDA}$  will firstly operate with low luminosity mode.

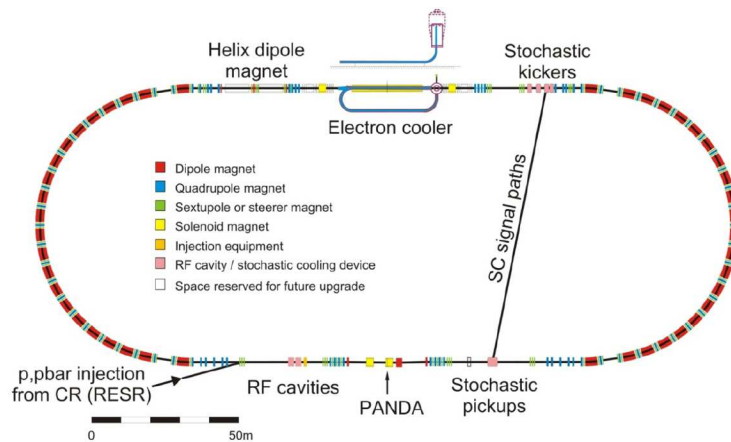


Figure 2.2: Schematic view of the HESR. Tentative positions for injection, cooling devices and experimental installations are indicated. [12]

## 2.2 The scientific goal of $\bar{\text{P}}\text{ANDA}$

The  $\bar{\text{P}}\text{ANDA}$  experiment will use the antiproton beam with a momentum range from 1.5 GeV/c to 15 GeV/c from the HESR hitting an internal proton or nuclear target. It is a general purpose set-up designed to carry out a rich and diversified hadron physics program [18]. The range of energies allows for the production of strange and charmed mesons and baryons and the production of gluonic excitations, as illustrated in figure 2.3. A major part of the physics

program therefore consists in collecting high precision data about hadronic states to understand the manifestations of QCD in the non-perturbative region. In particular, one fundamental question is the understanding of the origin of confinement of quarks and gluons in hadrons. Some important fields of research that  $\bar{P}$ ANDA will cover are exposed very briefly in the following.

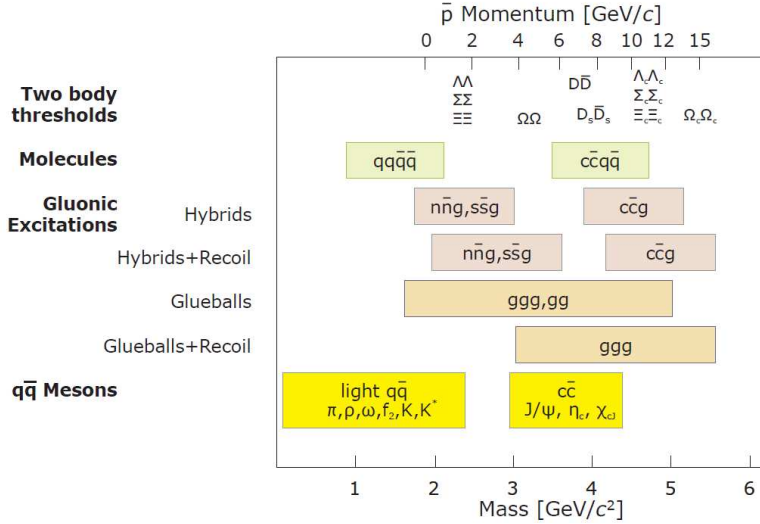


Figure 2.3: Mass range of hadrons accessible at the HESR with antiproton beams. The figure indicates the antiproton momenta required for charmonium spectroscopy, the search for charmed hybrids and glueballs, the production of D meson pairs and the production of  $\Sigma$  baryon pairs for hypernuclear studies. From [18].

- QCD Bound States.

The goal is to perform high precision charmonium ( $c\bar{c}$ ), D meson and baryon spectroscopy. Below the  $D\bar{D}$  threshold, at 3.73 GeV, most of the predicted states have been observed in experiments at  $e^+e^-$  colliders (Cornell, SLAC, BES, KEK,...) or in  $\bar{p}p$  reactions at Fermilab. However, while the precision on the measurement of the triplet states ( $J/\psi$ ,  $\chi_{c0}$ ,  $\chi_{c1}$ ,  $\chi_{c2}$ ) is very good, this is not the case for the singlet states ( $\eta_c$ ,  $h_c$ ) for which better measurements of the masses, widths and branching ratios are needed.

In addition,  $\bar{P}$ ANDA will look for new states of matter, such as gluonic hadrons (hybrid and glueballs), multiquark and molecular states.

- Non-perturbative QCD Dynamics.

Hyperon pair production reaction  $\bar{p}p \rightarrow \bar{Y}Y$ , which can be studied for hyperons with different flavors, are suitable to study the mechanism of quark-antiquark pair creation and their rearrangement into hadrons. The polarization accessible via the  $\Lambda \rightarrow p\pi$  decay can also be measured with  $\bar{P}$ ANDA.

- Hadrons in the nuclear medium.

The study of medium modifications of hadrons embedded in hadronic matter is directed at understanding the origin of hadron masses in the context of spontaneous chiral symmetry breaking in QCD and its partial restoration in a hadronic environment. So far experiments have been focused on the light-quark sector. The high-intensity  $\bar{p}$  beam of up to 15 GeV/c will allow an extension of this program to the charm sector for hadrons with hidden and open charm. The in-medium masses of these states are expected to be affected primarily by the gluon condensate. The extremely narrow states in the charm sector, for example the  $J/\Psi$  will increase the sensitivity for such medium modifications enormously.

- Hypernuclear physics.

Efficient production of hypernuclei with more than one strange hadron will be possible and will open new perspectives for nuclear structure spectroscopy and for studying the interaction between hyperons and nucleons.

- The Structure of Nucleon Using Electromagnetic Processes.

$\bar{\text{P}}\text{ANDA}$  will be able to investigate the structure of nucleon using the electromagnetic processes, such as the process  $\bar{p}p \rightarrow e^+e^-$  or  $\bar{p}p \rightarrow \mu^+\mu^-$  which will allow the determination of the electromagnetic time-like form factors of the proton in an extended  $q^2$  region. In addition, the process  $\bar{p}p \rightarrow \gamma\gamma$  will be used for the study of Generalized Distribution Amplitude (GDA), the process  $\bar{p}p \rightarrow \mu^+\mu^-X$  or  $\bar{p}p \rightarrow e^+e^-X$  for the study of Drell-Yan, and the  $\bar{p}p \rightarrow e^+e^-\pi^0$  or  $\bar{p}p \rightarrow J/\psi\pi^0$  reactions can access the pion nucleon Transition Distribution Amplitude (TDA). More details about nucleon structure studies with  $\bar{\text{P}}\text{ANDA}$  will be given in Chapter 3.

- Electroweak Physics.

The goal here is to take advantage of the high number of produced D-mesons to investigate their rare weak decays in order to test the Standard Model predictions and alternative models.

## 2.3 $\bar{\text{P}}\text{ANDA}$ set up

The physics program poses significant challenges to the PANDA detector. The tasks are summarized for the individual detectors:

- full angular coverage and good angular resolution for both charged and neutral particles
- particle identification in a large range of particles (electrons, muons, kaons, etc.) and energies
- high resolution in a wide range of energies
- high rate compatibility especially for the detectors close to target and the forward detectors.

The detector is split up into two spectrometers. A target spectrometer (TS) surrounds the interaction region and a forward spectrometer (FS) with a second magnet provides angular coverage for the most forward angles.

Conceptual designs of the detector are shown in figure 2.4.

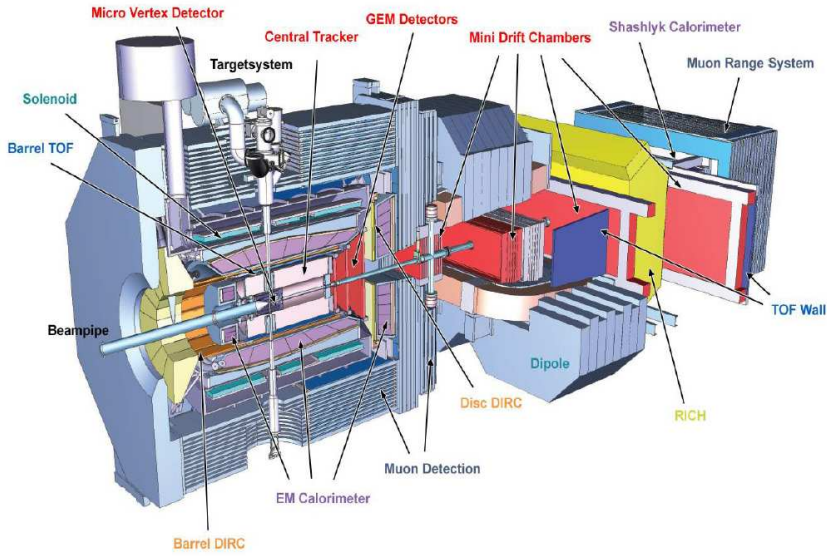


Figure 2.4: Side view of the  $\bar{\text{P}}\text{ANDA}$  detector with both target and forward spectrometers [12].

### 2.3.1 Target spectrometer

The anti-proton beam will interact with the target at the cross point with the target pipe which is located inside the solenoid. Particles emitted with laboratory polar angles larger than  $10^\circ$  in horizontal plane and  $5^\circ$  in vertical plane are measured in the target spectrometer. Surrounding the interaction volume will be a silicon micro-vertex detector (MVD) [20] including a barrel of five layers around the interaction region and six disks in the forward direction. Starting from a distance of 15 cm from the beam line up to 42 cm a second tracking detector will be situated. It will consist of 24 to 26 layers of straw tubes (STT) [12]. Particle identification with a ring-imaging Cerenkov (DIRC) counter realized by the detection of internally reflected Cerenkov light detector follows at a radial distance of 45 cm. The forward region will be covered by three sets of gas electron multiplier (GEM) and the forward Cerenkov detector. The inner detectors are surrounded by an electromagnetic calorimeter (EMC) [21] consisting of about 19 000 crystals read out with avalanche photodiodes. The detectors are contained within the coils of a solenoid providing a homogeneous magnetic field. Mini Drift Tubes (MDT) for muon identification will be mounted inside the return yoke.

#### 2.3.1.1 Target

The design of the solenoid magnet allows for an implementation of different target systems.  $\bar{\text{P}}\text{ANDA}$  will use both gaseous and non-gaseous targets. Hydrogen targets will be used for the study of antiproton-proton reactions. A high effective target density of about  $4 \cdot 10^{15}$  hydrogen atoms  $/\text{cm}^2$  must be achieved to fulfill the design goals of the high luminosity mode. An extension to heavier gases such as deuterium, nitrogen or argon is planned for complementary studies with nuclear targets. At present, two different solutions are under development: a cluster-jet and a pellet target. Both will potentially provide sufficient target thickness but exhibit different properties concerning their effect on the beam quality and the definition of the interaction point.

In the cluster jet target, clusters of hydrogen molecules are produced by the expansion of

pressurized cold hydrogen gas into vacuum forming a very diluted, homogenous target. The advantage of this technique is the stability in time of the density profile.

The pellet target is a stream of frozen hydrogen micro-spheres traversing the beam transversely with a velocity of about 60 m/s. This technique provides the desired average luminosity, its drawback is however the variable inter-spacing ( $\sigma \sim 0.5\text{-}5$  mm), leading to counting rate fluctuations, which the current R&D aims at reducing.

Both techniques allow the use of heavier gases, like deuterium, nitrogen or argon.

Solid targets are foreseen for hyper-nuclear studies and the study of antiproton-nucleus interaction using heavier nuclear targets.

### 2.3.1.2 Magnet

The solenoid magnet of the TS [22] will deliver a very homogeneous solenoid field of 2 T with fluctuations of less than  $\pm 2\%$ . In addition, a limit of  $\int B_r/B_z dz < 2\text{mm}$  is specified for the normalized integral of the radial field component. The superconducting coil of the magnet has a length of 2.8 m and an inner radius of 90 cm, using a laminated iron yoke for the flux return. The cryostat for the solenoid coils is required to have two warm bores of 100 mm diameter, one above and one below the target position, to allow for the insertion of internal targets. The integrated inner sub systems are attached to the magnet at several fixation points that take up the load.

### 2.3.1.3 Tracking system

The tracking system of the target spectrometer (TS) of PANDA will consist of three sub-detector systems. The MVD surrounded by the STT in the central part of the TS and in the forward direction completed with a detector based on gas electron multiplier (GEM) stations.

- Micro Vertex Detector

The design of the Micro Vertex Detector (MVD) [20] for the TS is optimized for the detection of secondary decay vertices from charmed and strange hadrons and for a maximum acceptance close to the interaction point. It will also strongly improve the transverse momentum and angular resolution. The setup is depicted in figure 2.5.

The concept of the MVD is based on radiation hard silicon pixel detectors with fast individual pixel readout circuits and silicon strip detectors. The layout foresees a four layer barrel detector with an inner radius of 2.5 cm and an outer radius of 13 cm. The two innermost layers will consist of pixel detectors and the outer two layers will be equipped with double-sided silicon strip detectors.

Six detector disks arranged perpendicular to the beam will achieve the best acceptance for the forward part of the particle spectrum. While the inner four layers will be made entirely of pixel detectors, the following two will be a combination of strip detectors on the outer radius and pixel detectors closer to the beam pipe.

Light weight and low Z material are used in order to keep the material budget of the MVD below 10% of a radiation length.

Electronically, the charge collected in the sensors is measured in the front-end electronics with the Time-over-Threshold method (ToT): the charge is integrated in a Charge Sensitive Amplifier (CSA), at the same time the capacitor of the CSA is discharged by a constant current source. The output of the CSA then is compared with a threshold voltage. The time the amplifier output is above this threshold is proportional to the deposited charge.

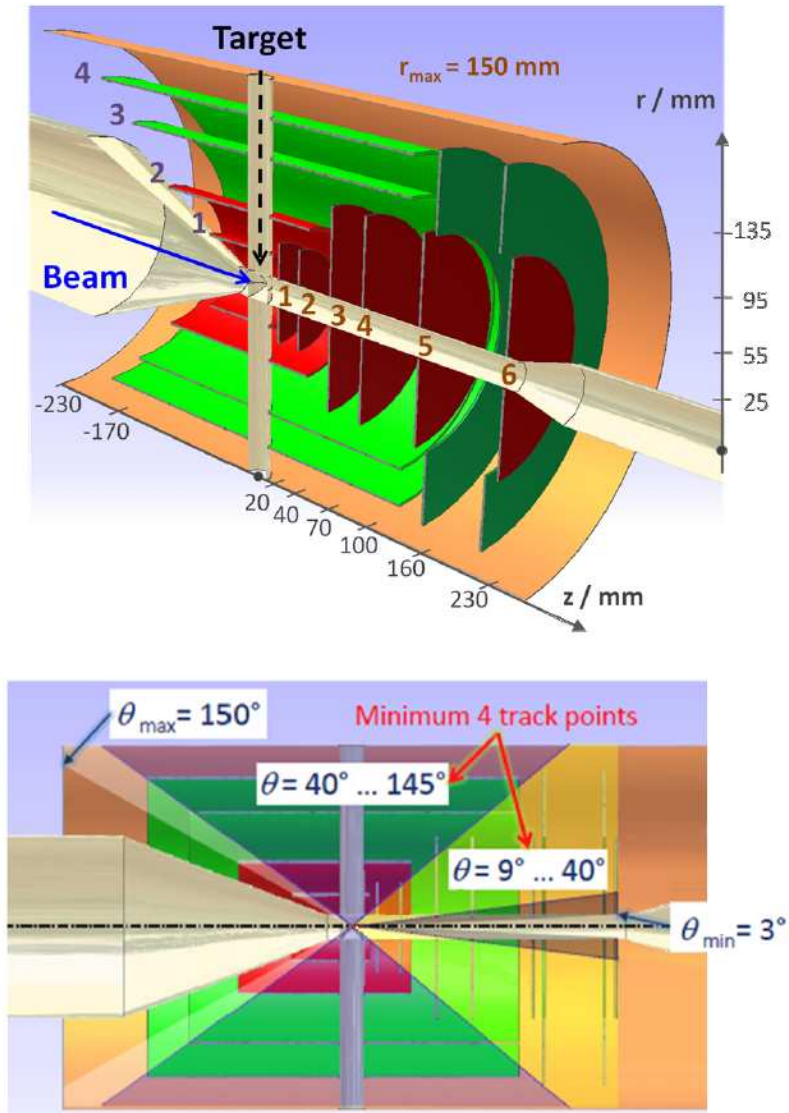


Figure 2.5: Schematic view of the MVD layer structure. Top: Four pixel disks at 2, 4, 7, and 10 cm, and two pixel/strip disks at 16 and 23 cm. Two pixel barrels at 2.5 and 5.5 cm, and two strip barrels at 9.5 and 13.5 cm; Bottom: Polar angle coverage. In a range of  $9^\circ < \theta < 145^\circ$  tracks leave at least four hits in the MVD. Down to  $3^\circ$  and up to  $150^\circ$  the MVD contributes with less hits per tracks [20]

A good position resolution of each hit on a sensor is mandatory for a good momentum and vertex reconstruction. In case of one digit per cluster, the resolution is limited by the readout layout size ( $100\ \mu\text{m}$  in  $z$ , a few tens of  $\mu\text{m}$  in  $x$  and  $y$ ).

- Straw Tube Tracker

The STT [12] is the main tracking detector for charged particles in the PANDA TS and consists of 4636 single straw tubes, arranged in a large cylindrical volume around the beam-target interaction point. It encloses the MVD for the inner tracking and is followed in beam direction by a vertical setup of GEM disks for adding track points in the forward polar angle range, as discussed in the previous section. (see figure 2.6)

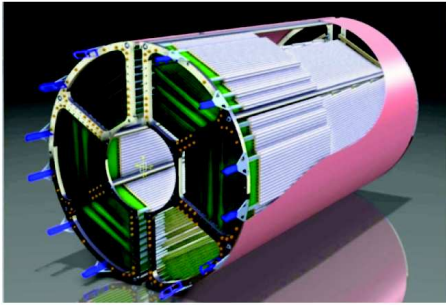


Figure 2.6: Schematic view of the STT detector. [12].

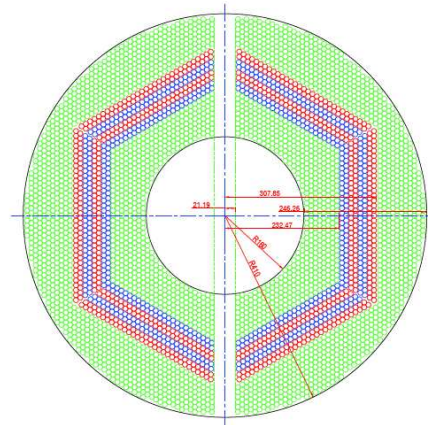


Figure 2.7: Layout of the straw tubes in the STT in  $xy$ -view. The green ones are parallel to the beam axis and the blue and red ones are skewed by  $\pm 2.9^\circ$  [12].

The layers in each of the six hexagonal sectors are arranged as follows. In radial direction and starting from the inner radius in a sector there are 8 straw layers parallel to the beam axis, followed by a block of 4 stereo double-layers, alternately skewed by  $\pm 2.9^\circ$  relative to the axially aligned straw layers, and again a block of 4 layers parallel to the beam axis. Then, there are another 7 layers aligned parallel to the beam with a decreasing number of straws per layer to achieve the outer cylindrical shape of the STT. The inner cylindrical shape is reached by placing a few axially aligned straws in the inner corner region of each hexagon sector (see figure 2.7).

All straws have the same inner diameter of 10 mm and length of 1500 mm, except a few outer straws in the border region of each skewed layer, which have different, reduced lengths. The film wall thickness of all straws is  $27\ \mu\text{m}$  Mylar, aluminized on the inner side and outer side of the tube. The close-packaging of the straws with less than  $20\ \mu\text{m}$  gaps between adjacent tubes yields the highest straw density with up to 27 layers in radial direction for the 3- dimensional track reconstruction. The  $x$ - $y$  projection of the track is obtained using up to 19 isochrone radii measured with a resolution of about  $150\ \mu\text{m}$  ( $\sigma_r$ ) for the layers with straws parallel to the beam axis, which are used for an helix fit. The 8 stereo layers provide the  $z$ -coordinates of the track with a single hit resolution of slightly better than 3 mm ( $\sigma_z$ ), which is determined by the isochrone resolution and the skew

angle ( $\alpha$ ) of  $\pm 2.9^\circ$  ( $\sigma_z = \sigma_r / \sin(\alpha)$ ). By measuring the drift time of the earliest arriving electrons, one gets the information about the minimum particle track distance from the wire. The isochrone contains all space points corresponding to the same electron drift time and describes a cylinder around the wire axis. The characteristic relation between drift time and isochrone is given by the electron drift velocity, depending on specific gas parameters, electric and magnetic field. Therefore, this fundamental relation has to be calibrated using reference tracks with known space and drift time information. The particle track is reconstructed by a best fit to the isochrones measured in a series of several straw tubes with the same orientation. Additional skewed straw layers provide a full stereo view of the particle trajectory.

The straws are gas-filled cylindrical tubes with a conductive inner layer as cathode and an anode wire stretched along the cylinder axis. An electric field between the wire and the outer conductor separates electrons and positive ions produced by a charged particle along its trajectory through the gas volume.

- Gas Electron Multipliers

Particles emitted at angles below  $22^\circ$  which are not covered fully by the STT will be tracked by three planar stations placed approximately 1.1 m, 1.4 m and 1.9 m downstream of the target. Each of the station consists of double planes with two projections per plane. The stations will be equipped with Gaseous micro-pattern detectors based on Gas Electron Multiplier (GEM) foils as amplification stages. The chambers have to sustain a high counting rate of particles peaked at the most forward angles due to the relativistic boost of the reaction products as well as due to the small angle  $\bar{p}p$  elastic scattering. The maximum expected particle flux in the first chamber in the vicinity of the 5 cm diameter beam pipe will be about  $3 \cdot 10^4 \text{ cm}^{-2} \text{ s}^{-1}$ .

### 2.3.1.4 Electromagnetic calorimeter

The EMC is used to measure the energy of  $\gamma$  and  $e^\pm$  by detecting the deposited electromagnetic shower over a dynamic range from few MeV up to 15 GeV [21]. In association with the tracking system, the electromagnetic calorimeter will help for particle identification of charged particles.

The EMC consists of one central barrel and two end caps (backward and forward). Figure 2.8 displays the barrel and the forward endcap. The central barrel is composed of 11360 crystals for a weight of 11 186 kg, a length of 2.50 m and an entrance radius of 0.57 m. It is divided into 16 identical sectors. To avoid photons going between two crystals, their axes are tilted by  $4^\circ$  which corresponds to a 4 cm shift of the focus point. Taking into account the barrel dimensions and crystal orientations, the barrel covers from  $22^\circ$  up to  $140^\circ$  polar angle. 6864 crystals form the forward end cap and 816 crystals compose the backward end cap. Both end caps are divided in 4 sectors. In a similar way to the central barrel, crystals are not pointing directly to the interaction point. Furthermore, the forward (backward) end cap covers the angles from  $5^\circ - 10^\circ$  up to  $22^\circ$  (from  $147.5^\circ$  up to  $\sim 165^\circ$ ).

Expected high count rates and a geometrically compact design of the TS require a fast scintillator material with a short radiation length and Moliere radius for the construction of the EMC. Lead tungstate ( $\text{PbWO}_4$ ) is a high density inorganic scintillator with sufficient energy and time resolution for photon, electron, and hadron detection even at intermediate energies. For high energy physics  $\text{PbWO}_4$  has been chosen by the CMS collaboration at CERN and optimized for large scale production [23].  $\text{PbWO}_4$  has been chosen due to its attractive characteristics (see Table 2.2 ). Its high density permits to have a relatively compact detector and its fast decay

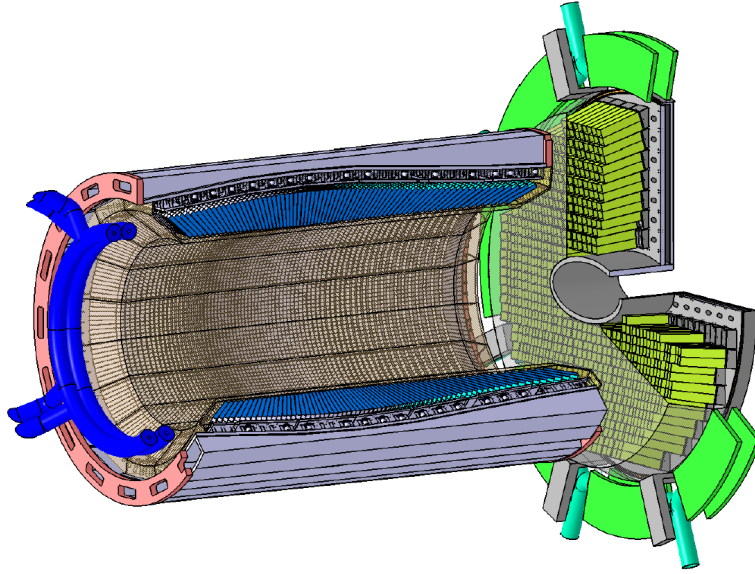


Figure 2.8: The barrel and forward end cap EMC. [21]

time of 6 ns (dominant at 97%) to allow the high counting rate especially at forward angle ( $10^7$  annihilations per second are expected at  $\bar{P}$ ANDA). The length of a crystal is about  $22X_0$  which permits to stop over 95% of the shower.

On the one hand, the average temperature gradient of the light yield amounts to  $\sim -3\%^\circ\text{C}^{-1}$ . The energy resolution will therefore be better with a lower temperature. On the other hand, the ratio of damage by radiation will be increased by a low temperature. To balance these effects, the working temperature of  $\text{PbWO}_4$  is chosen at  $-25^\circ\text{C}$ .

Parameter	$\text{PbWO}_4$
Density( $\rho$ )	$8,28 \text{ g.cm}^{-3}$
Radiation length ( $X_0$ )	0,89 cm
Energy loss (dE/dx) at MIP	$10.2 \text{ MeV.cm}^{-1}$
Decay time ( $\tau_{decay}$ )	6 ns
Light yield (LY)	0,6 (fast)% of NaI 0,1 (slow)% of NaI
$d(\ln(\text{LY}))/dT$	$-3\%.\text{C}^{-1}$

Table 2.2: Relevant  $\text{PbWO}_4$  properties.

Large Area Silicon avalanche photodiodes (LAAPDs) is used to detect the scintillation light of  $\text{PbWO}_4$ . For each scintillator, there are two APDs. It has several advantages as insensitivity to magnetic fields and low energy consumption. The size of each APD of  $7 \times 14 \text{ mm}^2$  will cover a large area of the rear crystal face.

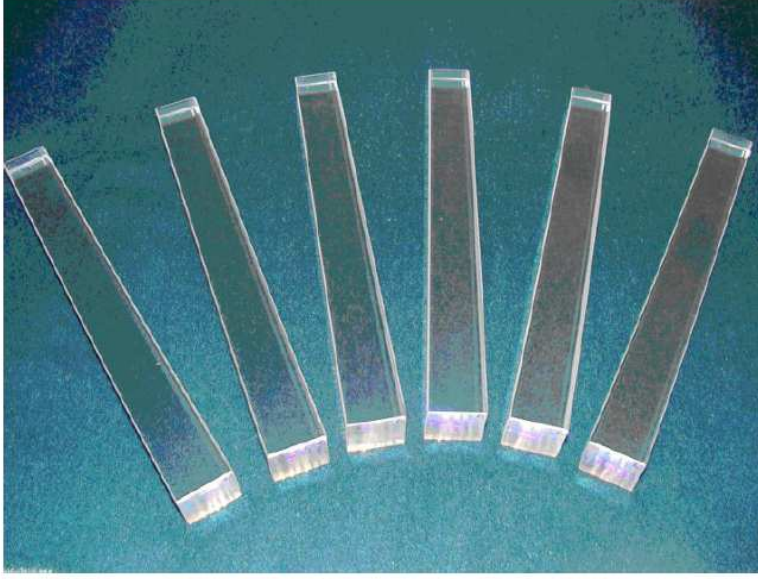


Figure 2.9: The PbWO4 used in  $\bar{P}$ ANDA EMC. [21]

### 2.3.1.5 Cerenkov detector

Cerenkov detector combined with the central tracker can help to identify particles with momenta from 0.8 GeV/c up to about 5 GeV/c. For slower particles, Time of Flight detectors can provide this information. The particle identification is really important to remove background from a channel of interest. Crossing a radiator with a refraction index  $n$ , a charged particle with a velocity  $\beta > \beta_{threshold}$  (with  $\beta_{threshold}=1/n$ ) emits radiations with a  $\theta$  angle following the formula  $\cos\theta = 1/(\beta n)$ . Knowing the particle momenta (from the central tracker) and measuring the  $\theta$  angle, the particle can be identified.

The Cerenkov detector is composed by one barrel for angles above  $22^\circ$  and a forward end cap for angles from  $5^\circ$  to  $22^\circ$ . The barrel DIRC (Detection of Internally Reflected Cerenkov light) [24] covers angles from  $22^\circ$  to  $140^\circ$  and surrounds the beam line at a radial distance from 45 to 54 cm i.e. just in front of the EMC crystals. Fused silica (i.e.: artificial quartz) with a refractive index of 1.47 was chosen as radiator material. The advantage of the use of fused silicon is the small thickness of the quartz slabs, only 1.7 cm. The slabs limit the creation of pre-shower electrons and gammas, which is a problem as the DIRC is located just in front of the EMC. The imaging will be achieved by lenses focusing on micro-channel plate photomultiplier tubes (MCP PMTs) which are insensitive to magnetic fields. In addition, the MCP PMTs provide good time resolution. For the forward end cap DIRC, the same concept is used: the radiator material consists of fused silica and MCP PMTs for the imaging. The forward end cap is a 2 cm thick disk and fits within a 110 cm radius.

### 2.3.1.6 Time of flight

Time of Flight information combined with the momentum measured in the tracker is helpful for the identification of slow particles at polar angles from  $22^\circ$  to  $140^\circ$ . The barrel time-of-flight is planned as a scintillator tile hodoscope using 8000 small scintillator tiles coupled with Silicon Photomultipliers with a resolution of 100 ps. It will be located between the central tracker and the DIRC.

### 2.3.1.7 Muon detector

The goal of the muon detector is to separate primary muons from pions and from secondary muons coming from pion decays. A segmentation of the yoke of the solenoid magnet acts as absorber with interleaved tracking detectors to measure energy losses and decays. The barrel part is segmented in a first layer of 6 cm iron followed by 12 layers of 3 cm thickness with 3 cm gap for tracking detectors. The end cap is divided into 5 layers of 6 cm iron plus a removable muon filter of 5 additional layers of 6 cm iron. Aluminium drift tubes with read out on both ends (to obtain longitudinal coordinate) are used as detectors.

### 2.3.2 Forward spectrometer

Particles emitted with polar angles below  $10^\circ$  and  $5^\circ$  in the horizontal and vertical direction, respectively, are detected with the forward-spectrometer (FS). The current design includes a 1 m gap dipole and tracking detectors for a momentum analysis of charged particles, i.e. mini drift chambers (MDC) and straw-tube trackers. A shashlyk-type calorimeter consisting of lead scintillator sandwiches (EMC) will identify photons and electrons, but also high energy hadrons and muon counters will also be installed (see figure 2.10).

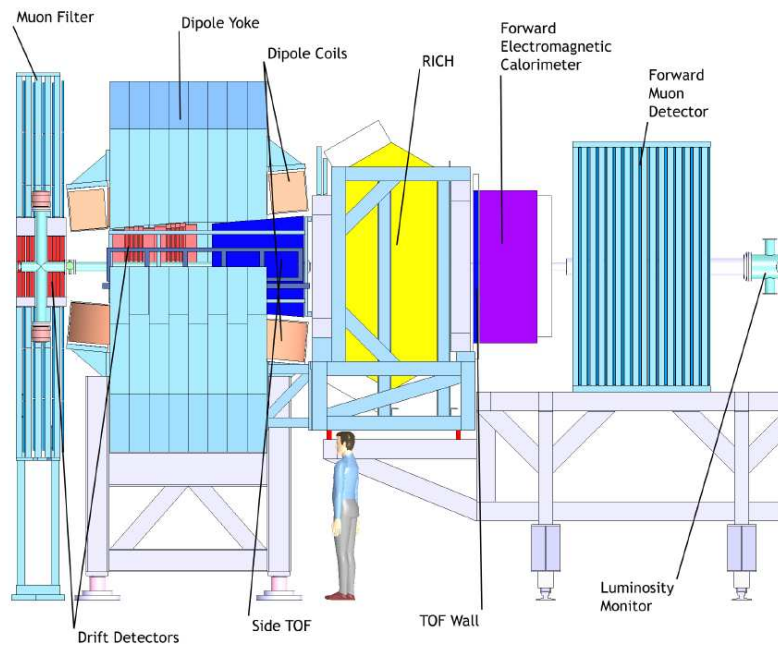


Figure 2.10: Artistic side view of the Forward Spectrometer (FS) of  $\bar{P}$ ANDA. [12]

#### 2.3.2.1 Forward tracker

The particle trajectories in the field of the dipole magnet will be measured with three pairs of tracking drift detectors. The first pair will be placed in front, the second within and the third behind the dipole magnet. Each pair will contain two autonomous detectors, thus, in total, 6 independent detectors will be mounted. Each tracking detector will consist of four double-layers of straw tubes, two with vertical wires and two with wires inclined by a few degrees. The planned configuration of double-layers of straws will allow to reconstruct tracks in each pair of tracking detectors separately, also in case of multi-track events.

### 2.3.2.2 Forward Cerenkov and TOF Detectors

A wall of slabs made of plastic scintillator and read out on both ends by fast photo-tubes will serve as time of flight stop counter placed at about 7 m from the target. Similar detectors will be placed inside the dipole magnet opening to detect low momentum particles which do not exit the dipole magnet. The time resolution is expected to be in the order of 50 ps thus allowing a good  $\pi/\text{K}$  and  $\text{K}/\text{p}$  separation up to momenta of 2.8 GeV/c and 4.7 GeV/c, respectively.

To enable the  $\pi/\text{K}$  and  $\text{K}/\text{p}$  separation also at the highest momenta, a RICH detector is proposed. The favored design is a dual radiator RICH detector similar to the one used at HERMES [25]. Using two radiators, silica aerogel and  $\text{C}_4\text{F}_{10}$  gas, provides  $\pi/\text{K}/\text{p}$  separation in a broad momentum range from 2 to 15 GeV/c.

### 2.3.2.3 Forward calorimeter

For the detection of photons and electrons a Shashlyk type calorimeter with high resolution and efficiency will be employed. The detection is based on lead-scintillator sandwiches read out with wave-length shifting fibers passing through the block and coupled to photo-multipliers. The lateral size of one module is 110 mm\*110 mm and a length of 680 mm ( $= 20X_0$ ). A higher spatial resolution will be achieved by sub-dividing each module into 4 channels of 55 mm\*55 mm size coupled to 4 PMTs. To cover the forward acceptance, 351 such modules, arranged in 13 rows and 27 columns at a distance of 7.5 m from the target, are required. With similar modules, based on the same technique as proposed for  $\bar{\text{P}}\text{ANDA}$ , an energy resolution of  $4\%/\sqrt{E}$  has been achieved.

### 2.3.2.4 Forward muon system

For the very forward part of the muon spectrum, a further range tracking system consisting of interleaved absorber layers and rectangular aluminum drift-tubes is being designed, similar to the muon system of the TS, but laid out for higher momenta. The system allows discrimination of pions from muons, detection of pion decays and, with moderate resolution, also the energy determination of neutrons and anti-neutrons. The forward muon system will be placed at about 9 m from the target.

## 2.3.3 Luminosity detector

Most of the physics topics planned for investigation using the  $\bar{\text{P}}\text{ANDA}$  detector require a determination of the luminosity with a very high accuracy to better than  $\approx 3\%$ . In order to achieve this,  $\bar{\text{P}}\text{ANDA}$  will rely on luminosity determination using the differential cross section of the elastic  $\bar{p}p$  scattering in the angular range from 3 to 8 mrad for the scattered anti-protons. The cross section at very small momentum transfer  $t$  (very small scattering angle), where the Coulomb part of the elastic cross section dominates, can be calculated very precisely. However at high energies, hadronic contribution at small  $t$  cannot be ignored. The parameters for the description of the differential elastic cross section will be measured in the dedicated Day-1 experiment with  $\bar{\text{P}}\text{ANDA}$ .

## 2.3.4 Data acquisition and trigger

In  $\bar{\text{P}}\text{ANDA}$  due to the rather high total cross-section of anti-proton-proton reactions of  $\sigma_{\bar{p}p} \approx 60\text{-}100$  mb, the expected average reaction rate computes to  $N = 20$  MHz with peak values of up to  $N_{max} \approx 40$  MHz. Combined with an average event size of 10-20 kB, this leads to a total raw

data rate of roughly 200 GB/s as shown in figure 2.11. Unlike other high energy experiments as ATLAS or CMS [26], where the charged multiplicity per reaction can be as large as a few tens in pp collisions and up to a few thousands in heavy ion collisions, the  $\bar{P}$ ANDA experiment produces only a few charged particles per reaction. However the reaction rate is so large ( $10^7/s$ ) that the data rate for  $\bar{P}$ ANDA will be even higher than the LHCb experiment at CERN.

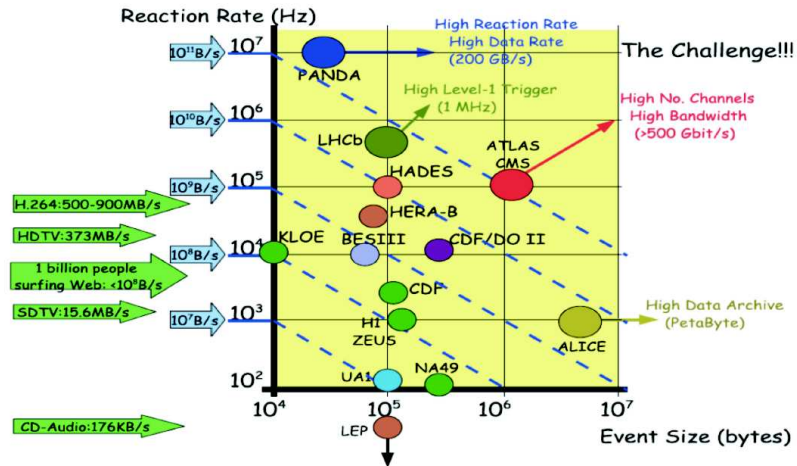


Figure 2.11: Event rates versus event sizes for various experiments. [27]

Assuming a duty cycle of 50 %, recording the unfiltered data stream would require a storage capacity of roughly 3000 PB per year, only a tiny fraction actually containing reactions of interest. Since providing this large amount of storage is neither efficient nor affordable, the data rate has to be reduced by approximately a factor of 1000 in order to keep the required storage capacity in the order of a few PB per year.

Therefore, the  $\bar{P}$ ANDA data acquisition (DAQ) system is based on a trigger-less read-out, i.e. the detectors front-end (FE) electronics and DAQ continuously sample and buffer data without any classical gated trigger signal. This approach principally allows to pre-analyze the data in an appropriate way before deciding to keep or reject a particular part of the data.

For example, in the electromagnetic channels, like  $e^+e^-$  or  $e^+e^-\pi^0$ , all the available energy is measured in the EMC. On the other hand, the charged pionic background deposits only a part of their energy. So, a threshold of energy deposit in EMC can reject most of the pionic data.



---

## Chapter 3

# Electromagnetic channels for nucleon structure studies with PANDA

As mentioned in the introduction, the study of the nucleon structure is one of the ways to learn about the strong interaction. The goal is to obtain a picture of the nucleon at different scales (so-called nowadays femto-tomography of the nucleon), allowing for studies of QCD properties from the perturbative regime to the region of strong coupling. The electromagnetic interaction, which is very well described by QED, provides a unique tool for these studies and is intensively used, especially at electron facilities, like JLab, but also at  $e^+e^-$  colliders, like BEPC or KEKB. Nucleon structure can be also studied using electromagnetic channels in  $\bar{p}p$  annihilation reactions. These channels have been less used up to now, due to the small number and the low luminosities of previous antiproton facilities.

The future availability of intense antiproton beam at FAIR puts this possibility forward. As described briefly in chapter 2, nucleon structure studies belong to the scientific program of PANDA. In this chapter, after mentioning shortly the different observables which parametrize the proton structure and can be accessed with the PANDA detector, we will describe in more detail two of them, namely the electromagnetic form factors and the Transition Distribution Amplitudes.

### 3.1 Different observables accessible with PANDA

Electron scattering experiments and electromagnetic channels in  $\bar{p}p$  annihilation reactions are very complementary tools to study the nucleon structure. Using crossing symmetry, observables parametrizing the nucleon structure are accessible in more than one reaction, as illustrated in figure 3.1. For this discussion, we introduce the Mandelstam variable  $s$ , i.e. the squared total center of mass energy and  $t$  and  $u$  the squared four-momentum transfers between the beam particle and outgoing particle, as well as  $q^2$ , which is the four-momentum squared of the virtual photon.

- Electromagnetic form factors are related to the charge and magnetization distributions in the proton. They are analytical functions of the four-momentum transfer  $q^2$ . Form factors can be accessed either in electron-proton elastic scattering ( $q^2 < 0$ ) or in  $\bar{p}p \rightarrow e^+e^-$  or  $e^+e^- \rightarrow \bar{p}p$  reactions ( $q^2 > 0$ ) (first column of figure 3.1). Depending on the four-momentum transfer squared, the electromagnetic structure at different scales can be probed.
  - Generalized Distribution Amplitudes (GDA) describe the transition  $\bar{p}p \rightarrow \bar{q}q$ . They might
-

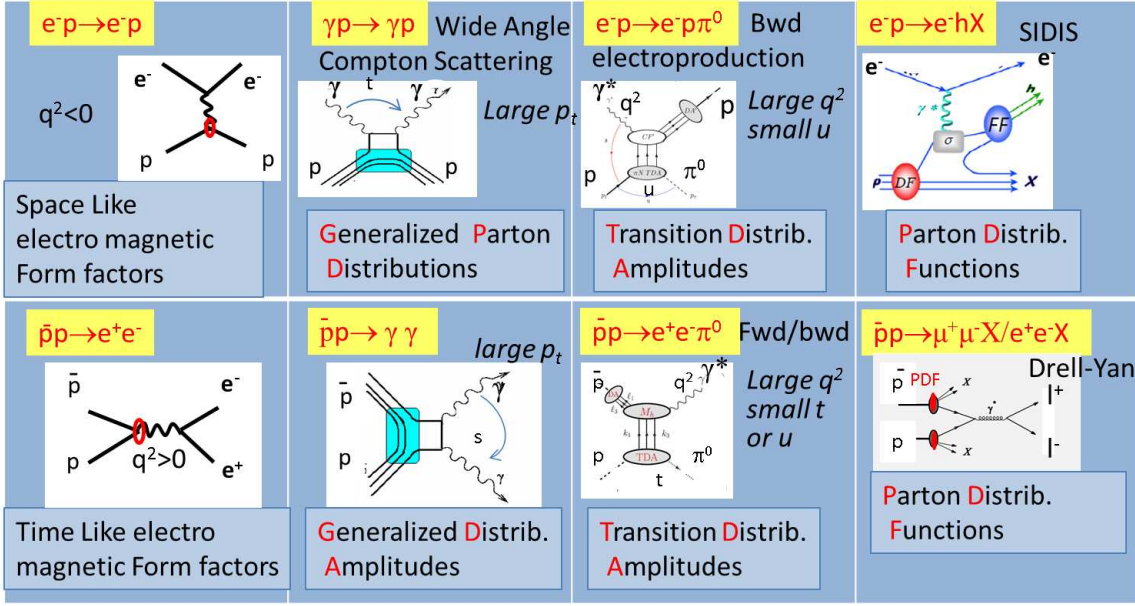


Figure 3.1: Different observables that can be accessed in electron scattering experiments and their counterpart in  $\bar{p}p$  annihilation reactions.

be accessed in  $\bar{p}p \rightarrow \gamma\gamma$  reaction at large transverse momentum of one of the emitted photon. They are the counterparts of Generalized Parton Distributions which parametrize the correlations of quarks inside the nucleon, which can be accessed for example in Wide Angle Compton Scattering (WACS), at large transverse momentum of the outgoing photon (second column of figure 3.1). Note that GDA are also called Time-Like GPDs. The GPD or GDA can be accessed only assuming the dominance of the handbag diagram which is calculated using a factorization between the hard calculable part and the soft part parametrized by the GPD or GDA. It has to be noted that the reliability of the factorization has not yet been proved in the case of the annihilation reactions, but there are arguments in this direction [28]. The  $\bar{p}p \rightarrow \gamma\pi^0$  could also be used to extract the GDA and has the advantage of a larger cross section.

- Transition Distribution Amplitudes (TDA) describe the partonic correlations in the transition between the nucleon and another particle. In this way, the different Fock components of the nucleon wave function can be probed, as will be described in more detail in sec. 3.3. For example, the same  $\pi N$  TDA can be measured either in backward pion electroproduction or in  $\bar{p}p \rightarrow e^+e^-\pi^0$  (or  $\bar{p}p \rightarrow J/\Psi\pi^0$ ) reactions (third column of figure 3.1).
- Transverse Momentum Dependent Parton Distribution Functions (TMD-PDF) describe the distributions of partons including their polarization, as a function of the fraction  $x$  of longitudinal momentum of the proton carried by the parton and the transverse momentum  $k_T$  of the parton. They can be accessed in Semi-Inclusive Deep Inelastic Scattering (SIDIS) reactions, but in this case, they are convoluted with Fragmentation Functions (FF) (fourth column of figure 3.1). The advantage of the annihilation reaction is to provide a direct access to the TMD-PDFs. This reaction has in addition a unique sensitivity to the Transverse Momentum Dependent distributions of transversely polarized partons.

The common challenge of the measurements of electromagnetic channels in  $\bar{p}p$  annihilation reaction is the huge hadronic background, which makes the observables much more difficult to measure than in electron scattering experiments. In the following, I will study in more details the possibility with PANDA to access electromagnetic form factors and TDA.

## 3.2 Electromagnetic form factors of proton

### 3.2.1 Kinematics

Electromagnetic form factors are analytical functions of  $q^2$ . They parametrize the internal structure of the proton in the electromagnetic vertex. The nucleon form factors can be measured

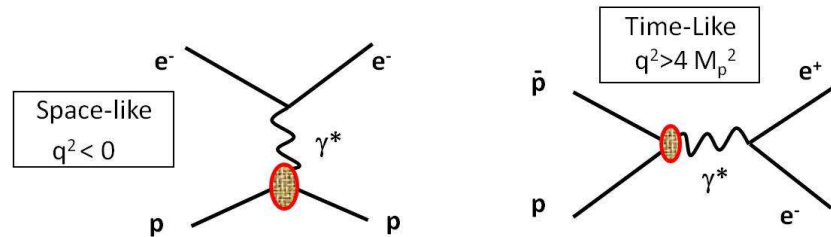


Figure 3.2: Feynman diagram for the single-photon exchange, or Born term, for elastic ep scattering (left) and  $\bar{p}p$  annihilation (right).

in the space like region ( $q^2 < 0$ ) and the time like region ( $q^2 > 0$ ), using either e-p elastic scattering or annihilation reactions ( $e^+e^- \rightarrow \bar{p}p$ ) assuming the dominance of the one photon exchange graph (figure 3.2).

In electron-proton scattering, see figure 3.2, the kinematics is such that  $q^2$  is negative. This is the Space-Like region (SL) and one generally uses:  $Q^2 = -q^2$ .

In annihilation experiments, like  $\bar{p}p \rightarrow e^+e^-$  or  $e^+e^- \rightarrow \bar{p}p$  (see right part of figure 3.2), the Time-Like region is probed,  $q^2$  is fixed at a given center of mass energy  $\sqrt{s}$  to the positive value:

$$q^2 = s, \quad (3.1)$$

In addition, in the case of the  $\bar{p}p$  reaction,  $q^2$  is deduced from the kinetic energy T of the incident antiproton by the simple relation

$$q^2 = 2M_p(T + 2M_p), \quad (3.2)$$

In the Time-Like region, the form factors present poles due to the particle production channels ( $\rho, \omega, \phi, \dots$ ).

The region where  $0 < q^2 < 4M_p^2$  cannot be accessed in any of these experiments and is called the unphysical region (see figure 3.3). The form factors in this region are involved in the description of electromagnetic channels like  $\bar{p}p \rightarrow e^+e^- \pi^0$ , as we will see in sec. 3.3.

### 3.2.2 General properties of the proton form factors

The electromagnetic form factors are scalar complex functions of  $q^2$  which parametrize the hadronic structure at the electromagnetic vertex. Being a spin 1/2 particle, the proton has two electromagnetic form factors. We will consider here the Sachs form factors:  $G_E(q^2)$ , the electric form factor and  $G_M(q^2)$ , the magnetic form factor. They fulfill the following properties

$$G_E^p(0) = 1, \quad G_M^p(0) = \mu^p/\mu_N, \quad G_E^n(0) = 0, \quad G_M^n(0) = \mu^n/\mu_N, \quad (3.3)$$

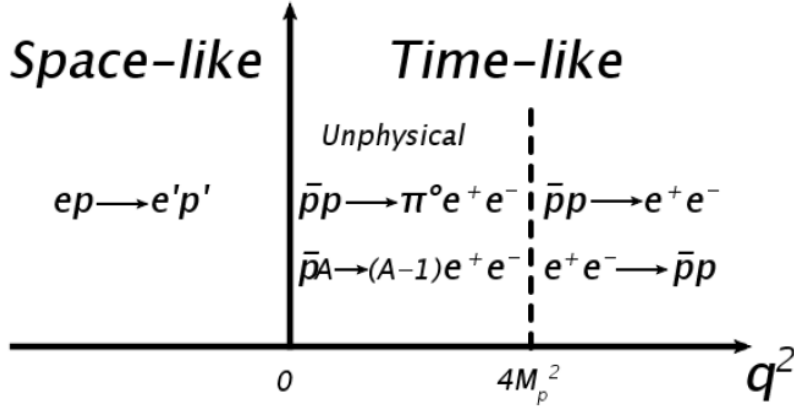


Figure 3.3: Space-like and Time-like regions and possible reactions to access the electromagnetic form factors in each region.

where  $\mu^p$  and  $\mu^n$  are respectively the proton and neutron magnetic moments and  $\mu_N = e\hbar/2M_p$  is the nuclear magneton. The definition of these form factors also implies that in the TL region  $G_E(4M_p^2) = G_M(4M_p^2)$ . This can be seen either from their definition starting from the Fermi and Pauli form factors [29] or from the fact that the angular distribution at threshold in the  $\bar{p}p \leftrightarrow e^+e^-$  should be isotropic at threshold (see Eq.3.18).

These complex functions are real for negative  $q^2$  and have a non-zero imaginary part for  $q^2 > 4M_\pi^2$ , where  $M_\pi$  is the pion mass, which reflects the existence of physics channels in the annihilation reaction.

In the non-relativistic approximation, the Space-Like form factors  $G_E(q^2)$  and  $G_M(q^2)$  can be identified to the Fourier transforms of the spatial charge and magnetization distributions in the nucleon [30]. However, taking into account relativistic effects, the relation between form factors and charge and magnetization spatial distributions depends on the reference frame. Using the Breit frame (in which the incident and final protons have the same energy), the Space-Like form factors  $G_E(q^2)$  and  $G_M(q^2)$  are equal to the Fourier transforms of the spatial charge and magnetization distributions in the nucleon [30]. However, the practical use of this relation is limited. Recently, a breakthrough has been made by establishing a relation between the form factors and the distributions of charge quark densities of nucleons in the infinite momentum frame [31, 32].

The physical interpretation of the Time-Like form factors is different. As mentioned by Zichichi, already in 1962 [33], they reflect the frequency spectrum of the electromagnetic response of the nucleon. The form factors are indeed sensitive in the Time-Like region to the physics channels that are open in the annihilation reactions.

In addition, dispersion relations relate form factors values in the space like region to the imaginary part of the form factors in the time like region:

$$f(q^2) = \frac{1}{\pi} \int_{4M_\pi^2}^{\infty} \frac{Imf(s)ds}{s - q^2} \quad (3.4)$$

### 3.2.3 Asymptotic behaviour

In the regime of very large  $Q^2$ , the form factor behavior should follow the perturbative QCD predictions. According to quark counting rules [34], the following relation should be fulfilled for both Space-Like and Time-Like regions:

$$G_E^{\text{SL}}(Q^2) \sim G_M^{\text{SL}}(Q^2) \sim \frac{\alpha_s^2(Q^2)}{Q^4} \sim \frac{1}{Q^4 \ln^2(Q^2/\Lambda^2)}, \quad (3.5)$$

$$G_E^{\text{TL}}(q^2) \sim G_M^{\text{TL}}(q^2) \sim \frac{\alpha_s^2(q^2)}{q^4} \sim \frac{1}{q^4 \ln^2(q^2/\Lambda^2)}, \quad (3.6)$$

where  $\alpha_s(Q^2)$  is the strong coupling constant.

Besides, the Phragmén-Lindelöf theorem [35] gives a prescription for the asymptotic behavior of analytical functions

$$\lim_{q^2 \rightarrow +\infty} F(q^2) = \lim_{q^2 \rightarrow -\infty} F(q^2) \quad (3.7)$$

, meaning that, asymptotically, in the Time-Like region, the imaginary part of the form factors vanishes, and the real part is equal to the Space-Like form-factor.

### 3.2.4 Proton electromagnetic form factors in the Space-Like region.

In the Space-Like region, the Rosenbluth and polarization methods can be used to extract the form factors. These two methods are based on the assumption of one-photon exchange in the electron proton scattering process.

#### 3.2.4.1 Rosenbluth method

The Rosenbluth method allows to separate  $G_E^2$  and  $G_M^2$  for proton and neutron. The method requires measuring the cross section for  $eN$  scattering at a number of electron scattering angles and incident energies for a given value of  $Q^2$ . This is obtained by varying both the beam energy and the electron scattering angle over as large a range as experimentally feasible (see sec. 3.2.1).

The differential cross section in the laboratory of ep scattering is written as follows:

$$\left( \frac{d\sigma}{d\cos\theta_{e'}} \right)^{\text{lab}} = \left( \frac{d\sigma}{d\cos\theta_{e'}} \right)_{\text{Mott}} \frac{\tau}{\epsilon(1+\tau)} \left( G_M^p{}^2 + \frac{\epsilon}{\tau} G_E^p{}^2 \right) \quad (3.8)$$

where:

$$\left( \frac{d\sigma}{d\cos\theta_{e'}} \right)_{\text{Mott}} = \left( \frac{\alpha}{2E_e} \right)^2 \frac{\cos^2\theta_{e'}/2 E'}{\sin^4\theta_{e'}/2 E'}, \quad (3.9)$$

$$\tau = Q^2/(4M_p^2), \quad (3.10)$$

$$\epsilon^{-1} = 1 + 2(1+\tau)\tan^2(\theta_{e'}/2) \quad (3.11)$$

where  $\epsilon$  is the virtual photon polarization and  $E_e$  is the incident electron energy,  $q_e$  is the electron charge and  $\theta_{e'}$  is the final electron angle.  $\left( \frac{d\sigma}{d\cos\theta_{e'}} \right)_{\text{Mott}}$  is the Mott cross-section corresponding to the elastic scattering of a relativistic electron by a point-like spin-less proton, whose recoil energy is neglected.

The reduced cross section is defined as:

$$\left( \frac{d\sigma}{d\cos\theta_{e'}} \right)_{\text{red}}^{\text{lab}} = \frac{\epsilon(1+\tau)}{\tau} \left( \frac{d\sigma}{d\cos\theta_{e'}} \right)^{\text{lab}} / \left( \frac{d\sigma}{d\cos\theta_{e'}} \right)_{\text{Mott}} \quad (3.12)$$

and one gets the linear relation:

$$\left( \frac{d\sigma}{d\cos\theta_{e'}} \right)_{red}^{lab} = G_M^p{}^2 + \frac{\epsilon}{\tau} G_E^p{}^2. \quad (3.13)$$

With these relations, the electric and magnetic form factors can be deduced from a linear fit of the reduced cross-sections measured at different  $\epsilon$  values.

Following this procedure,  $G_E$  and  $G_M$  have been measured separately up to  $Q^2 = 7 (GeV/c)^2$ , and the ratio  $\mu_p G_E/G_M$  was within 30% as expected from the pQCD prediction. For the large  $Q^2$  region,  $G_E$  is experimentally difficult to extract, due to the kinematical factor  $\epsilon/\tau$  in eq. 3.13. However,  $G_M$  was measured up to  $Q^2 = 31 (GeV/c)^2$  assuming  $\mu_p G_E = G_M$ .

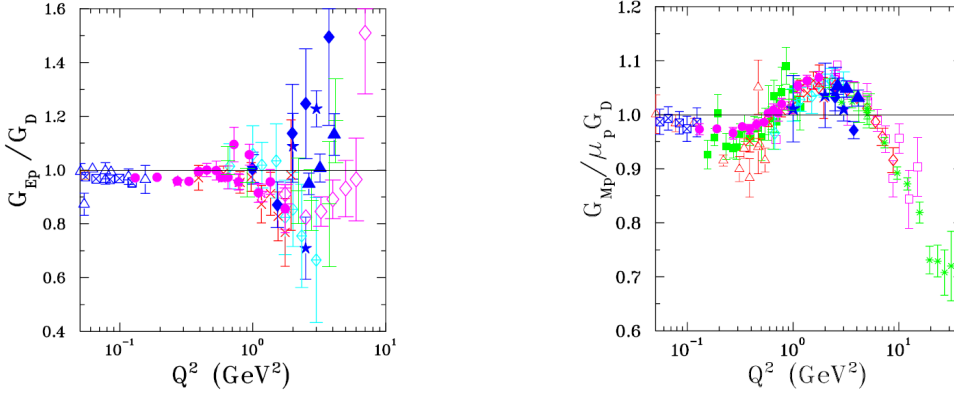


Figure 3.4: Data for  $G_E^p/G_d$  and  $G_M^p/(\mu_p G_d)$  in the Space-Like region, obtained with the Rosenbluth technique [36].

Figure 3.4 displays the values of  $G_E$  and  $G_M$  obtained in this way, divided by the dipole function

$$G_d(Q^2) = \left( \frac{1}{1 + \frac{Q^2}{M_d^2}} \right)^2, \quad (3.14)$$

$$\text{with } M_d^2 = 0.71 (GeV/c^2)^2. \quad (3.15)$$

### 3.2.4.2 Polarization transfer experiment

An alternative method exists to extract the nucleon electromagnetic form factors. This method, which requires polarized electron beams and either polarized proton target or measurement of the proton polarization, was first suggested by Akhiezer and Rekalov [38] in 1968. With the measurement of the longitudinal ( $P_l$ ) and transverse ( $P_t$ ) polarizations of the outgoing proton, the ratio  $G_E^p/G_M^p$  can be determined from:

$$R = \frac{G_E^p}{G_M^p} = -\frac{P_t}{P_l} \frac{E_e + E_{e'}}{2M_p} \tan \frac{\theta_{e'}}{2} \quad (3.16)$$

In this method, due to the larger sensitivity to  $G_E$ , more reliable results are expected at large  $q^2$  than in the case of the Rosenbluth method. In addition, the ratio  $R = G_E^p/G_M^p$  extracted from polarization measurement is much less sensitive to the radiative corrections and to the potential

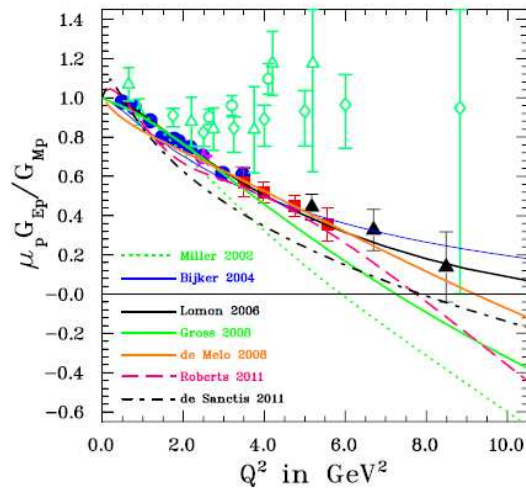


Figure 3.5: Recent measurements of  $\mu_P G_{Ep}/G_{Mp}$  ratio obtained from different JLab polarization data (full symbols) compared to the results of Rosenbluth analysis (green open points) and to different theoretical predictions. Figure taken from [37].

2  $\gamma$  exchange contributions. Because of this, it is believed that the polarization method gives a more reliable determination of  $G_{Ep}^p/G_M^p$  than the Rosenbluth method.

However, the results are found incompatible with the ones from the Rosenbluth method, as can be seen in figure 3.5. The ratio is decreasing very fast with  $Q^2$ , which is in clear contradiction with the perturbative QCD prediction of Brodsky and Farrar [34]. However, it can be explained by higher order perturbative QCD calculations [39], which take into account quark orbital angular momentum. These new form-factor measurements [36, 40, 41] can also be explained by a number of other models as shown in [37].

The study of electromagnetic form factors in the Space-Like region is a very active field. In a near future, new measurements at larger  $Q^2$  will be obtained at JLab at 12 GeV.

### 3.2.4.3 Two-photon contribution

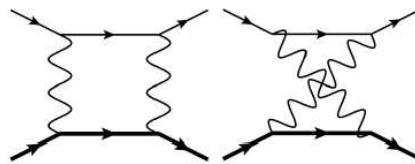


Figure 3.6: Graphs for the two-photon contribution in the ep elastic scattering reaction.

An important activity is also dedicated to measuring the effect of  $2\gamma$  contribution, which is expected to be the source of discrepancy between the results obtained in Rosenbluth and polarization methods. In the usual radiative corrections,  $2\gamma$  exchanges are taken into account using the approximation that the dominant fraction of four-momentum transfer squared is taken by one of them. The  $2\gamma$  contribution could manifest itself as a difference between differential cross sections in  $e^+p$  and  $e^-p$  elastic scattering at the same  $Q^2$  and  $\epsilon$ . However, no sizeable contribution has been measured up to now from the different experiments which have been

realized at Novosibirsk [42], JLab [40] and DESY(OLYMPUS experiment with analysis still on-going).

It has also to be noted that an alternative explanation to the discrepancy between the Rosenbluth and the polarization form factor results is given by higher order radiative corrections [43].

#### 3.2.4.4 Proton charge radius

At very low  $Q^2$  in the Space-Like region, the form factor measurements are used to extract the proton charge radius. Indeed the latter is defined as

$$\langle r_p^2 \rangle = -6 \left( \frac{\partial G_E(Q^2)}{\partial Q^2} \right)_{Q^2=0}. \quad (3.17)$$

The proton charge radius can also be obtained by measuring energy level shifts in electronic hydrogen as well as the Lamb shift in muonic hydrogen. The latter measurement is very precise but has a value that is 5 standard deviations lower than the values obtained from energy level shifts in electronic hydrogen and from electron-proton scattering experiments. The origin of this difference is at the moment not explained and triggers a lot of theoretical and experimental activity (see [44] for a review on the subject).

### 3.2.5 Proton electromagnetic form factors in the Time-Like region

#### 3.2.5.1 Experimental access to the Time-Like form factors

In the time like region, the nucleon electromagnetic form factors  $G_E$  and  $G_M$  can be extracted from measurements of the differential cross sections in the annihilation reactions,  $\bar{p}p \rightarrow e^+e^-$  or  $e^+e^- \rightarrow \bar{p}p$ . In these reactions, only a single measurement of the electron angular distributions at a given center of mass energy ( $q^2=s$ ) is needed to extract the module of the form factors  $G_E$  and  $G_M$ .

The differential cross section for  $\bar{p}p \rightarrow e^+e^-$  in the center of mass (CM) can be expressed as (neglecting the electron mass):

$$\left( \frac{d\sigma}{d\cos\theta_e^*} \right)^{CM} = \frac{\pi(\alpha_{em}\hbar c)^2}{8M_p^2\sqrt{\tau(\tau-1)}} \left[ |G_M^p|^2(1 + \cos^2\theta_e^*) + \frac{|G_E^p|^2}{\tau} \sin^2\theta_e^* \right] \quad (3.18)$$

where  $\tau = \frac{q^2}{4M_p^2}$  and  $\alpha_{em} \simeq \frac{1}{137}$  is the fine-structure constant. In a similar way to the Space-Like region, the sensitivity to  $G_E^p$  will become lower as one goes to higher  $q^2$  since the corresponding contribution scales with  $1/\tau$ .

After integration over  $\theta_e$ , one obtains:

$$\sigma = \frac{\pi(\alpha_{em}\hbar c)^2}{6M_p^2} \frac{(2\tau|G_M^p|^2 + |G_E^p|^2)}{\tau\sqrt{\tau(\tau-1)}}. \quad (3.19)$$

The total cross-section gives therefore access to an effective form factor, which is a linear combination of  $|G_E|^2$  and  $|G_M|^2$

$$\sigma_{tot} = \frac{\pi(\alpha\hbar c)^2}{6M_p^2} G_{eff}^2 \quad \text{with} \quad G_{eff}^2 = \frac{2\tau|G_M|^2 + |G_E|^2}{2\tau + 1}. \quad (3.20)$$

One also defines the ratio of the form factors:

$$R = |G_E^p|/|G_M^p|. \quad (3.21)$$

## 3.2.5.2 Existing data

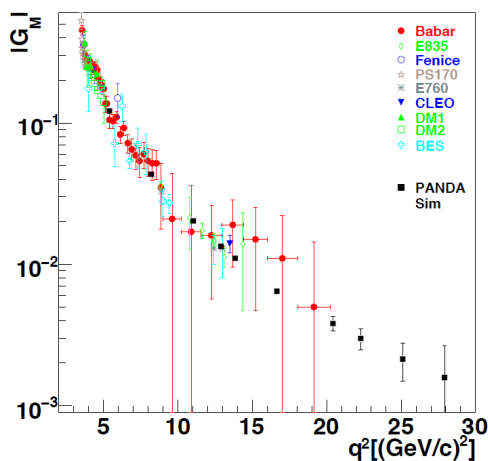


Figure 3.7: Existing data for the effective form factor  $|G_{eff}^p|/G_d$  in the Time-Like region. Projections for measurements in the  $\bar{p}p \rightarrow e^+e^-$  reaction with PANDA at an integrated luminosity of  $2 \text{ fb}^{-1}$  are shown as dark squares (adapted from [45]).

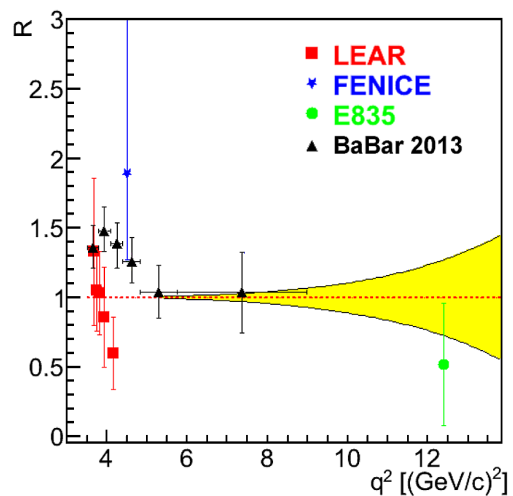


Figure 3.8: Expected statistical precision on the determination of the ratio  $R$  for PANDA measurements in the  $\bar{p}p \rightarrow e^+e^-$  reaction with PANDA at an integrated luminosity of  $2 \text{ fb}^{-1}$  from [45] (yellow band) for  $R = 1$ , as a function of  $q^2$ , compared with the existing data from [46] (triangles) and [47] (squares).

A recent review on the measurements of Time-Like form factors can be found in [29]. Most experiments in the time-like region were only able to provide total cross-sections and no angular distributions, therefore only an effective form factor was extracted (see Eq. 3.20). As can be seen from figure 3.7, many data points were recently provided by the BES-II collaboration at BEPC using an energy scan and by the BABAR collaboration at SLAC using the Initial State Radiation Technique [48]. In the latter method, the reaction  $e^+e^- \rightarrow \bar{p}p\gamma$  is used, allowing for a lower value of  $q^2 = M_{\bar{p}p}^2$  value at the  $\gamma^*\bar{p}p$  vertex. This technique is currently also exploited by the BES-III collaboration. The figure 3.7 does not include the updated BABAR data points corresponding to a higher statistics [46], which are consistent with the first ones, with reduced error bars by about 30%.

The region close to threshold attracts a lot of interest, due to the observed rise of the cross section close to the  $\bar{p}p$  threshold, which could be the hint of some contribution from resonances in the  $\bar{p}p$  system or from meson resonances below the  $\bar{p}p$  threshold [29]. But the observed effect could also be explained by Final State Interaction [49].

Concerning the high  $q^2$  region, the interest is to reach the perturbative QCD regime. The form factor values in the Time-Like region follow approximately the trend:

$$|G_{eff}| \sim \alpha_s^2(q^2)/q^2 \sim \frac{1}{q^2 \ln^2(q^2/\Lambda^2)}, \quad (3.22)$$

in agreement with pQCD prediction. However, the values in the Time-Like region are higher by a factor 2 than the values in the space-like region, which indicates that the asymptotic

regime is not yet reached. Very recently, new data points from the BABAR collaboration have been presented in a conference [50], up to  $q^2 = 36 \text{ GeV}/c^2$ , with values compatible with the SL ones. But these results are not very conclusive, since the error bars are very large and the measurements are averaged over bin width of about  $12 \text{ GeV}/c^2$ .

The ratio of electric to magnetic form factor has been extracted, by very few experiments, as can be seen from figure 3.8. The results of the PS170 experiment at LEAR and the BABAR experiment are not compatible. So, it is clear that the knowledge of electromagnetic form factors in the Time-Like region is still very poor.

The BESIII experiment is currently investigating the region close to threshold, using the ISR technique and could also perform direct measurements in an energy scan at different  $q^2$  between 4.0 and 20  $(\text{GeV}/c)^2$ . As will be discussed in the next section, PANDA can investigate the large  $q^2$  region in the  $\bar{p}p \rightarrow e^+e^-$  reaction.

### 3.2.6 Time-Like proton form factors with PANDA

A feasibility study of the proton form factor measurements at PANDA in the Time-Like region has been achieved in 2010 [45] using full-scale simulations with the same PANDA software as the one used for the physics benchmark simulations presented in [18]. An updated analysis using the PANDARoot framework is on-going [51]. A parametrization of the effective form factor measurements in the Time-Like region was used [52] as an input and the counting rates were evaluated using a luminosity of  $2 \text{ fb}^{-1}$ , corresponding to data taking during four months at the maximum luminosity of  $2 \cdot 10^{32} \text{ cm}^{-2}\text{s}^{-1}$ .

Special care was given to the realistic description of the background, which is mainly due to the  $\bar{p}p \rightarrow \pi^+\pi^-$  reaction and needs to be drastically reduced. The ratio of the cross sections for the  $\bar{p}p \rightarrow e^+e^-$  and  $\bar{p}p \rightarrow \pi^+\pi^-$  is indeed of the order of  $10^6$ . Using cuts on the particle identification and on the kinematics, it was shown that the contamination from the  $\bar{p}p \rightarrow \pi^+\pi^-$  reaction could be reduced to less than 1% in each angular bin.

This high rejection of the background is achieved, thanks to the complementarity of the detectors (STT, EMC, DIRC) for the particle identification and to the performance of the tracking which allows to apply efficient kinematical constraints. The statistical errors have also been evaluated and are shown in figure 3.8. The expected precision on R is better than 1% at  $5.1 \text{ (GeV}/c)^2$ , 15% at  $10 \text{ (GeV}/c)^2$  and 40% at  $14 \text{ (GeV}/c)^2$ . Besides, the effective form factor will be extracted with a precision degrading from 3% at  $q^2 = 5.1 \text{ (GeV}/c)^2$  to 60% at  $q^2 = 28 \text{ (GeV}/c)^2$  in the available kinematical range (figure 3.7). The BES experiment will have a better sensitivity close to threshold, but above  $8 \text{ (GeV}/c)^2$ , the sensitivity of PANDA is expected to be better. However, this experiment will need the maximum luminosity which will not be available at the early stages of data taking, since it requires the RESR (see sec. 2.1, which is not yet funded).

The two  $\gamma$  exchange contribution can be measured in the  $\bar{p}p \rightarrow e^+e^-$  reaction. Such contributions are indeed expected to produce an asymmetry in the angular distribution of  $e^+$  or  $e^-$  due to the presence of odd- $\cos(\theta)$  terms. It was shown in [45] that the PANDA experiment will be sensitive to a 5% contribution of these terms.

The electromagnetic form factors can be extracted in a very similar way using the  $\bar{p}p \rightarrow \mu^+\mu^-$  channel. This channel presents the interest of lower radiative corrections. However, the situation is very different from  $\bar{p}p \rightarrow e^+e^-$  from the experimental point of view. In this channel, due to the very close masses of muons and pions, the kinematics constraints do not help to reject the  $\pi^+\pi^-$  background and the extraction of the signal relies only on the performance of the muon detector. The segmentation of the yoke which acts as a pion absorber, with interleaved tracking

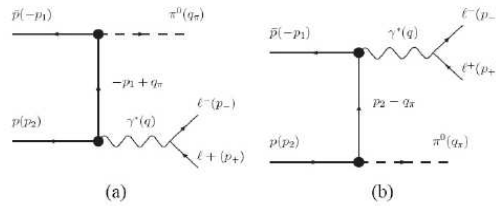


Figure 3.9: Graphs for the study of Time-Like form-factors below the  $\bar{p}p$  threshold in  $\bar{p}p \rightarrow e^+e^-\pi^0$  reactions.

detectors, is exploited to identify the muons. The analysis of this channel is on-going in Mainz, and will be part of I. Zimmermann’s PHD thesis.

To access the “unphysical” region corresponding to  $q^2$  lower than  $4M_p^2$ , the reaction  $\bar{p}p \rightarrow e^+e^-\pi^0$  can be used (figure 3.9), as was first proposed in [53]. The study of the feasibility of this measurement with PANDA was the subject of Jérôme Boucher’s PhD thesis [54], using a one nucleon exchange model developed by J. Van de Wiele and S. Ong. This model was based on the calculation by [55], but  $\pi NN$  form factors were added, to give realistic predictions for the cross section. The latter were adjusted to data measured in the  $\bar{p}p \rightarrow \pi^0\gamma$  channel.

Another way to access the unphysical region is to study the reaction  $\bar{p}A \rightarrow e^+e^-(A-1)$ . In this case, the annihilation takes place on a bound proton, moving according to the Fermi momentum distribution, allowing to access lower  $q^2$  than in the  $\bar{p}p \rightarrow e^+e^-$  reaction. The simplest case is the deuterium nucleus and rough estimates have been made at the lowest available  $\bar{p}$  momentum of 1.5 GeV/c [56].

### 3.3 Transition Distribution Amplitudes

#### 3.3.1 Definition

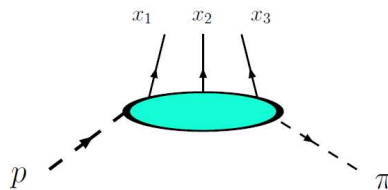


Figure 3.10: Scheme of the transition from a proton to a pion plus 3-quarks. The longitudinal momentum fractions  $x_i$  of the proton carried by each quark might be positive or negative.

The basis for the QCD description of hadron structure is the factorization of the amplitudes for hard exclusive reactions between a short distance part which can be calculated in a perturbative way and a long distance part which contains non-perturbative matrix elements related to the hadron structure. This approach is extensively used in forward hard exclusive processes, where the non-perturbative matrix element is the Generalized Parton Distributions (GPD). (see figure 3.1 and [57] for a review on the subject). The GPD are non-diagonal matrix elements of quark-antiquark or gluon-gluon non-local operators on the light cone, which describe correlations between partons inside the nucleon.

Transition Distribution Amplitudes (TDAs) were introduced as an extension of GPD. The

concept of TDAs was first mentioned in [58], where these functions were called Skewed Distribution Amplitudes (SDA), and were defined as a non-diagonal matrix element of a tri-local quark operator between a meson and a proton or a photon and a proton.

TDAs allow to parametrize the transition from a nucleon to three quarks + another hadron (see figure 3.10), for example  $p \rightarrow \pi$ ,  $p \rightarrow \gamma$  or  $p \rightarrow \rho$ . They are therefore sensitive to the different components of the nucleon wave function, as depicted in figure 3.11. They can also be seen as an extension of the Distribution Amplitudes (DA) which describe the transition from a baryon to three quarks and are sensitive to the minimal three-quark component of the proton wave function.

$$\underbrace{|qqq\rangle}_{\text{Described by DA}} + \underbrace{|qqq\pi\rangle + |qqq\rho\rangle + |qqq\eta\rangle}_{\text{TDA}} \dots$$

Figure 3.11: TDAs are defined as a way to probe the proton wave function.

Mathematically, the DA (Distribution Amplitude) is defined as

$$\langle 0 | \epsilon^{ijk} u_\alpha^i(z_1 n) u_\beta^j(z_2 n) u_\gamma^k(z_3 n) | N(p, s_p) \rangle \quad (3.23)$$

and a  $\pi - N$  TDA is defined as

$$\langle \pi(p_\pi) | \epsilon^{ijk} u_\alpha^i(z_1 n) u_\beta^j(z_2 n) u_\gamma^k(z_3 n) | N(p, s_p) \rangle \quad (3.24)$$

where  $\epsilon^{ijk} u_\alpha^i(z_1 n) u_\beta^j(z_2 n) u_\gamma^k(z_3 n)$  is the hadronic matrix element of 3 quark operators on the light cone.  $\alpha, \beta, \gamma$  are the quark flavor indices,  $N(p, s)$  and  $\pi(p_\pi)$  are respectively the nucleon and  $\pi$  wave functions.  $p$  and  $s_p$  are respectively the proton momentum and spin and  $p_\pi$  the pion momentum.

TDAs contribute to the imaging, or femto-photography, of the nucleon via their Fourier transform to the impact parameter space. For example, the  $\pi - N$  TDA gives information on the structure of the pion cloud in the transverse plane in the infinite momentum space (see figure 3.12).

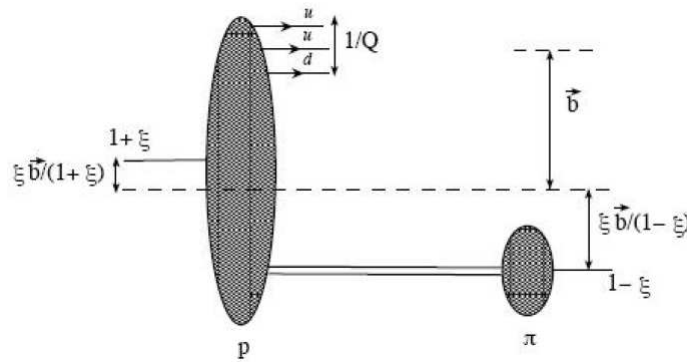


Figure 3.12: Impact parameter representation of the TDA.

Like GPDs, DAs and TDAs can be calculated using models. Recent lattice QCD calculations are also able to provide estimates for these quantities [59]. While nucleon DA models can

be constrained by the electromagnetic form factors measurements at large  $q^2$  and GPDs have been already explored in different reactions at Jlab, there is at the moment no experimental information on the TDAs.

### 3.3.2 Factorization approach and experimental access to TDAs

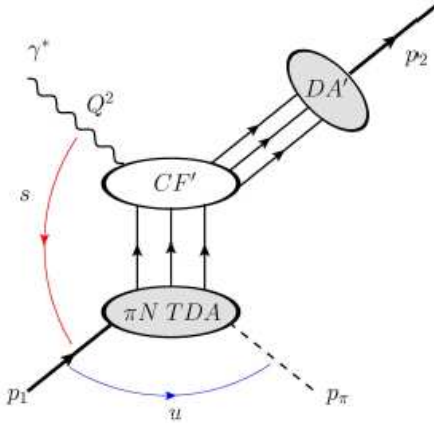


Figure 3.13: The factorization of backward electro-production reaction  $\gamma^* p \rightarrow p' \pi^0$ .

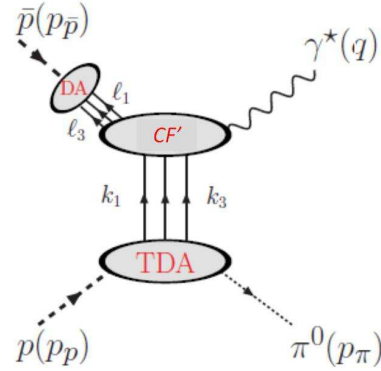


Figure 3.14: The factorization of the annihilation process  $\bar{p}p \rightarrow \gamma^* \pi^0$ .

As shown by Pire and co-workers [60, 61, 62, 63], two main classes of reactions can be identified to give access to meson-nucleon or photon-nucleon TDAs: backward meson or photon electroproduction processes on the one hand and  $\bar{p}p$  annihilation into an  $e^+e^-$  pair and a meson or a photon on the other hand. The pion production is the most probable and therefore it seems easier to have access to  $\pi - N$  TDA.

In the case of electroproduction, the validity of the factorization approach is expected for the backward production (small  $u$ ). For the  $\bar{p}p$  annihilation factorization, there are two available kinematical regions: in the small  $u$  region (backward pion production), the proton-pion TDA can be investigated, while the small  $t$  (forward pion production) give access to antiproton-pion TDAs.

The factorization schemes in backward pion electroproduction and  $\bar{p}p \rightarrow e^+e^- \pi^0$  reactions are illustrated in figure 3.13 and 3.14. In the figures, DA stand for the proton distribution amplitude,  $CF'$  for the hard subprocess amplitude which is calculable and TDA for the  $\pi - N$  TDA.

While the study of backward electro-production of a pion in the  $\gamma^* p \rightarrow p' \pi^0$  reaction is on-going at JLab [64] and might be continued at JLab12GeV, the PANDA experiment will open the possibility to access the fully unexplored hard exclusive processes in  $\bar{p}p$  annihilation.

As discussed before, the extraction of matrix elements like GPD, TDA or DA in hard exclusive processes needs the validity of the amplitude factorization approach, which requires a large scale in the reaction. The latter is given by the four-momentum squared (or virtuality  $Q^2$  in the space-like case and  $q^2$  in the Time-Like case) of the virtual photon in the electromagnetic interaction.

The rigorous proof of such a factorization scheme has been provided up to now only for the GPDs in the forward Deeply Virtual Compton Scattering (DVCS) or exclusive meson production.

However, as discussed in [58], a factorization approach might also be valid in the case of backward Compton scattering or backward meson electroproduction, where TDA are the relevant hadronic matrix elements.

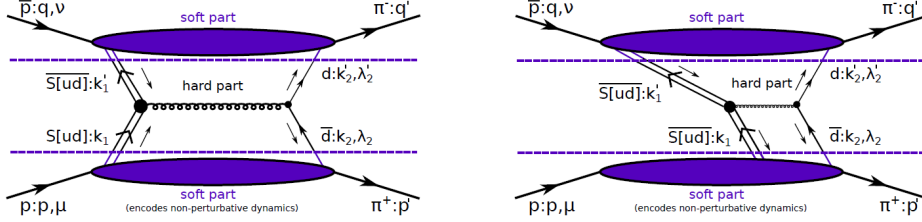


Figure 3.15: The factorization of the annihilation process  $\bar{p}p \rightarrow \pi^+\pi^-$ .

It was also suggested that  $\pi$ -nucleon TDAs could be accessed by the  $\bar{p}p \rightarrow \pi^+\pi^-$  reaction [65], the two contributing graphs corresponding to this factorization scheme in this case are given in figure 3.15. The validity of the factorization scheme for this process requires a large  $s$  and large center-of-mass angles of the emitted pions.

### 3.3.3 Mathematical description of TDA

Let us introduce the needed quantities for a more formal discussion on the TDAs. In the light cone system,  $P = (p_p + p_\pi)/2$  is the average 4-momentum of the proton-pion system,  $\Delta = p_\pi - p_p$  is the 4-momentum transfer between the proton and the pion. Two vectors  $p$  and  $n$  are defined, such that  $2p \cdot n = 1$ . The transverse component of  $\Delta$  is  $\Delta_T$  and the skewness  $\xi$  is defined as

$$\xi = -\frac{\Delta \cdot n}{2P \cdot n} \quad (3.25)$$

which corresponds to the fraction of longitudinal momentum transfer.

At the leading twist (twist-3), the parametrization of the Fourier transform of  $\pi N$  matrix elements of the three-local light cone quark operator involves eight invariant TDAs. The latter are functions of the light-cone momentum fractions  $x_i$ , the skewness variable  $\xi$ , the four-momentum transfer squared  $\Delta^2$  and the factorization scale  $\mu_F$

$$\begin{aligned} 4(P \cdot n)^3 \int \left[ \prod_{j=1}^3 \frac{d\lambda_j}{2\pi} \right] e^{i \sum_{k=1}^3 x_k \lambda_k (P \cdot n)} \langle \pi_\alpha(p_\pi) | \hat{O}_{\rho\tau\chi}^{\alpha\beta\gamma}(\lambda_1 n, \lambda_2 n, \lambda_3 n) | N_\iota(p_1) \rangle \\ = \delta(x_1 + x_2 + x_3 - 2\xi) \sum_{s.f.} (f_a)^\alpha{}_{\beta\gamma} s_{\rho\tau\chi} H_{s.f.}^{(\pi N)}(x_1, x_2, x_3, \xi, \Delta^2, \mu^2) \end{aligned} \quad (3.26)$$

where  $H_{s.f.}^{(\pi N)}(x_1, x_2, x_3, \xi, \Delta^2, \mu^2)$  are the eight TDAs.

TDAs are universal objects which depend only on  $\xi$  and  $\Delta_T$ , and not on squared  $e^+e^-$  invariant mass ( $Q^2$ ) and squared center of mass energies ( $W^2$ ). The same TDA should therefore be measured in different kinematics or different reactions. This property can be used to check the consistency of the TDA approach in the different reactions. However, the factorization hypothesis needs first to be checked.

In the limit  $\xi \rightarrow 0$ , where the pion takes all the longitudinal momentum of the nucleon, the TDA is expected to be equal to the DA.  $\xi \rightarrow 1$  is the soft pion limit, where the pion takes

only a little fraction of the nucleon longitudinal momentum. In this limit, constraints from the chiral dynamics can be used, while when  $\xi \neq 1$ , phenomenological inputs are needed. In the limit  $\Delta_T = 0$ , the pion is emitted close to  $0^\circ$  or  $180^\circ$ , only three invariant amplitudes contribute ( $V_1^{\pi N}$ ,  $A_1^{\pi N}$ ,  $T_1^{\pi N}$ ).

One interesting characteristics of the hard part of the amplitude is that only transversely polarized virtual photons are produced and therefore a lepton angular distribution in  $1+\cos^2\theta$  is expected in the reference frame of the virtual photon. Another interesting feature is the  $1/Q^8$  dependence of the cross section. Both results can be used to check the consistency of the description of the reaction in terms of TDAs.

### 3.3.4 Predictions from TDA models for different reactions

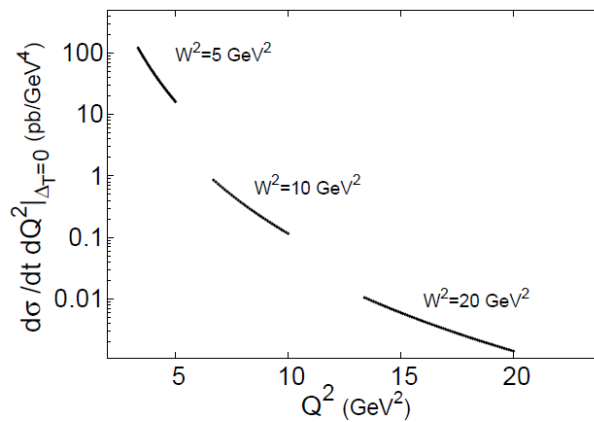


Figure 3.16: Differential cross section as a function of  $Q^2$  for the annihilation process  $\bar{p}p \rightarrow \gamma^*\pi^0$  for different squared center of mass energies  $W^2$ . Figure from [61].

A model for  $\pi$ -nucleon TDAs based on the soft pion theorem was proposed [60] and used to estimate the cross-section for the  $\bar{p}p \rightarrow e^+e^-\pi^0$  reaction [61]. In this model, the TDAs have no explicit  $\Delta_T$  dependence and therefore the model can be applied only for the emission of the pion close to  $0^\circ$  or  $180^\circ$ .

The predictions of this model for the differential cross-section as a function of  $Q^2$  are displayed in figure 3.16. It can be seen that the cross section decreases very rapidly with  $Q^2$ .

As we will see below, this model was used to make a first feasibility study for TDA investigations in the  $\bar{p}p \rightarrow e^+e^-\pi^0$  reaction.

However, according to the authors themselves, this model was oversimplified. The fact that there is no  $\Delta_T$  dependence hindered practical use of the model. In addition, it is valid only in the soft pion limit ( $\xi=1$ ), where the pion takes a very small fraction of the nucleon longitudinal momentum and the pion is emitted almost at rest. Therefore, it can not provide a realistic description of the transition amplitude outside this strict domain.

A few years later, a more general model was proposed [62]. In addition to the spectral part, which is fixed by the soft pion theorem and valid close to  $\xi=1$ , a contribution due to nucleon pole exchange was added (see figure 3.17). The graph enclosed in the red circle corresponds to the Leading Order (LO) graph for the nucleon electromagnetic form factor calculation in perturbative QCD, where the two blobs stand for the nucleon (or antinucleon) DAs.

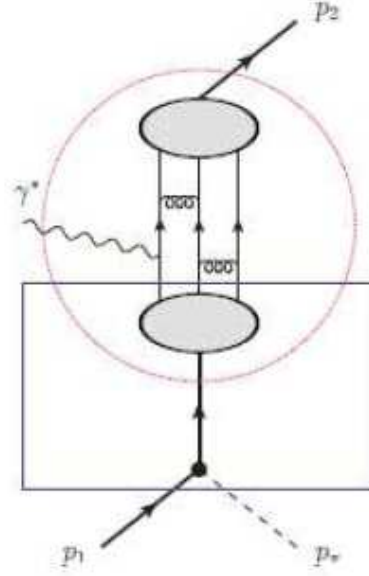


Figure 3.17: Nucleon pole contribution to the  $\pi N$  TDA. The two grey blobs stand for the nucleon DAs.

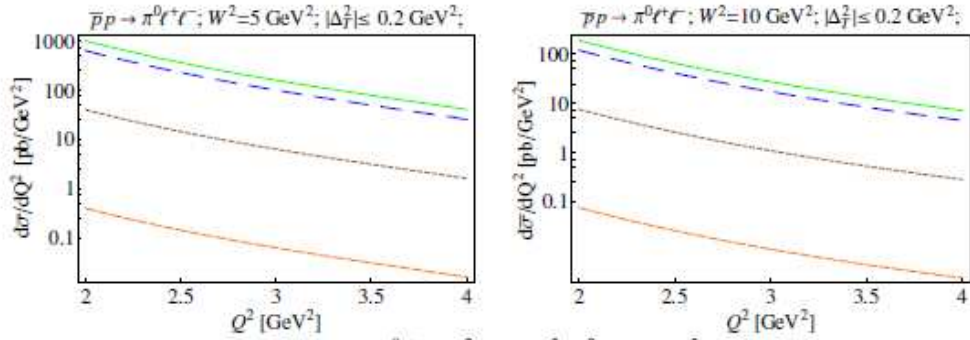


Figure 3.18: Integrated cross sections for  $\bar{p}p \rightarrow e^+e^-\pi^0$  over the range  $\Delta_T^2 \leq 0.2$  ( $\text{GeV}/c$ )<sup>2</sup> as a function of  $q^2$  for  $W^2=5$   $\text{GeV}^2$  (left) and  $W^2=10$   $\text{GeV}^2$  (right) for various phenomenological nucleon DA solutions. COZ (blue long dashes) ; KS (green solid line) ; BLW NLO (orange medium dashes) and NNLO modification of BLW (brown short dashes) (see references in [63] from which the picture is extracted.)

It was shown that the contribution of the nucleon pole exchange diagram is dominant for  $\xi \neq 1$ .

Numerical estimates for the  $\bar{p}p \rightarrow e^+e^-\pi^0$  reaction were therefore provided with the nucleon pole exchange diagram. A set of DA models fitting the nucleon electromagnetic form factors were used to calculate the  $\bar{p}p \rightarrow e^+e^-\pi^0$  amplitudes [63]. The differential cross-sections  $d\sigma/dQ^2$  calculated with this improved model for the t-channel (forward emission) are shown in figure 3.18, where they are integrated for  $\Delta_T^2 < 0.2 \text{GeV}^2$ . They are displayed for different phenomenological DA models. A very strong dependence on model input is observed, although each of the models

reproduces the electromagnetic form factor. Here, also a decrease of the cross section for a given  $q^2$  and different center-of-mass energy squared can be observed. Depending on  $W^2$ , different skewness  $\xi$  will be probed.  $\xi$  decreases when  $W^2$  increases for a given  $q^2$ . Therefore, it is interesting to measure the reaction at different energies. Similar results can be obtained for the backward (y-channel) pion emission.

Estimates were also given for the  $\bar{p}n \rightarrow e^+e^-\pi^-$  and  $\bar{p}p \rightarrow e^+e^-\eta$  reactions where the cross sections are respectively 40% larger and about a factor 5 smaller. The TDA formalism can also be extended to other mesons ( $\rho$ ,  $\phi$ , ...) in order to probe other components of the proton wave function.

In [10], calculations for the reaction  $\bar{p}p \rightarrow J/\Psi\pi^0$  were provided. The latter will be shown in sec. 6.2, together with the results of the feasibility study which are part of my PhD work.

The analysis of JLab backward pion electroproduction is still on-going, but results have been presented in a conference and are displayed in figure 3.19. The experimental differential cross section obtained for different  $Q^2$  are compared to the predictions of a model similar to [62]. The order of magnitude of the cross section is fine, but the dependence as a function of  $t$  is not correctly described.

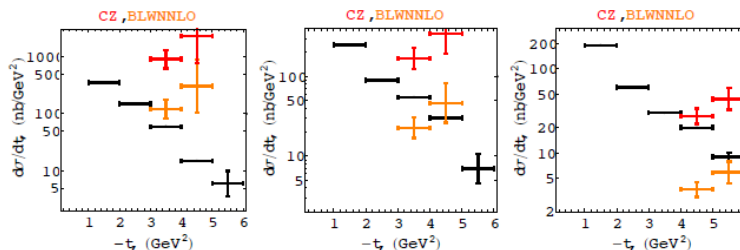


Figure 3.19: The  $d\sigma/dt$  differential cross section measured by the CLAS collaboration (black) for different  $Q^2$  and  $x_B$  bins compared with theoretical calculations with a TDA model with two different nucleon DAs (orange and red). From left to right: ( $Q^2 = 2$  GeV<sup>2</sup>,  $x_B = \pm 0.375$ ), ( $Q^2 = 3$  GeV<sup>2</sup>,  $x_B = \pm 0.525$ ), ( $Q^2 = 4$  GeV<sup>2</sup>,  $x_B = \pm 0.525$ ). Picture from [64].

### 3.3.5 Feasibility study of the TDA measurement in the $\bar{p}p \rightarrow e^+e^-\pi^0$ for PANDA

The feasibility of measuring TDAs in the  $\bar{p}p \rightarrow \gamma^*\pi^0 \rightarrow e^+e^-\pi^0$  reaction has been studied by Maria Carmen Mora Espi in her PhD thesis [66] using full scale simulation of the signal and backgrounds reactions.

The model of [61], briefly described in sec. 3.3.4 was used to produce signal events from the reaction  $\bar{p}p \rightarrow e^+e^-\pi^0$ . Since the  $\Delta_T$  dependence of the TDA is not given by the model, the cross section was assumed to be constant over the range  $|\cos(\theta_0)| > 0.5$ . The study was made at  $W^2 = 5$  GeV<sup>2</sup> and  $W^2 = 10$  GeV<sup>2</sup> with  $q^2$  respectively in the range [3.0, 4.3] and [5.0, 9.0].

As was the case for the electromagnetic form factor studies, the main problem is the rejection of the hadronic background. Among all the copiously produced hadronic channels, the reaction  $\bar{p}p \rightarrow \pi^+\pi^-\pi^0$  is the most difficult to suppress, since the kinematics is very close to  $\bar{p}p \rightarrow e^+e^-\pi^0$ . Strict cuts on the electron PID probabilities were applied in order to reduce the number of misidentified pions (see section 4.2.5). It was shown that rejection powers ranging from  $10^8$  to  $6 \cdot 10^6$  can be achieved depending on  $Q^2$  and  $W^2$ , while keeping an electron efficiency larger than 40%. In these conditions, a total number of about 1500 signal events at  $W^2 = 5$  GeV<sup>2</sup> and

about 200 signal events at  $W^2=10 \text{ GeV}^2$  will be recorded for each of the t- or the u-channel configurations for an integrated luminosity of  $2 \text{ fb}^{-1}$ , corresponding to 100 days at the maximum luminosity of  $2 \cdot 10^{32} \text{ cm}^{-2} \text{ s}^{-1}$ .

This shows that the cross section can be measured in the given  $q^2$  range. Since the cross section decreases fast with  $q^2$ , statistical errors are however large for the largest  $q^2$  bins.

To estimate the residual hadronic contamination after the analysis cuts, the hypothesis was made that the ratio of cross sections  $\sigma(\pi^+\pi^-\pi^0)/\sigma(e^+e^-\pi^0)$  is equal to  $10^6$ , independently on the energy and  $q^2$ . If this is the case, with the rejection powers of the hadronic background obtained in this analysis, a contamination lower than 20% is expected. We will see in sec. 6.2.5 that our investigations of the  $\sigma(\bar{p}p \rightarrow \pi^+\pi^-\pi^0)$  reaction suggest much larger ratios of pionic to leptonic cross sections as well as a strong dependence of this ratio as a function of  $q^2$ .

---

## Chapter 4

# Simulation and Reconstruction

A specific simulation and analysis tool is needed in the PANDA experiment. In this chapter, I will first introduce the structure and basic concept of this framework, then I will explain how a simulation chain can be processed. At the end, I will show some results to illustrate the performance of the particle reconstruction and identification. I will also study the tracking system acceptance and track finder efficiency for different particles.

### 4.1 Simulation tools

In the PANDA experiment, analysis is performed using PandaRoot, a software framework which is still under active development. PandaRoot is used for detector studies as well as analysis of benchmark channels. It is implemented within the FairRoot framework, which is being developed by GSI and used by all the major FAIR experiments (See figure 4.1).

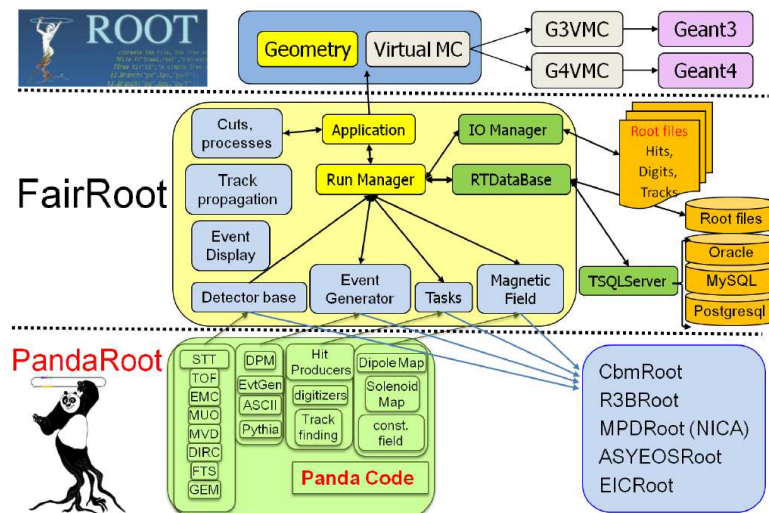


Figure 4.1: Code design of the FairRoot and PandaRoot frameworks. From [67].

FairRoot relies on Root and Virtual Monte Carlo (VMC) among other external packages and implements basic features including the provision of an interface for simulation and geom-

---

etry handling as well as a parameter database and I/O for data storage and retrieval. As an application of FairRoot, PandaRoot indirectly depends on the same external packages. However the main part of the PandaRoot code is specific to PANDA experiment. In the following, the external packages and the internal PandaRoot code will be briefly described.

#### 4.1.1 External packages

The external pack is the collection of a number of software packages that the internal PandaRoot code depends on. The packages included in the external package are, among others, Root, VMC, GEANT, PYTHIA and PLUTO.

ROOT is a framework for data processing and analysis, developed by a team of physicists at CERN. It provides a very diverse set of tools and functionality tailored for the needs of particle physicists.

VMC [68] is the abstract interface for various available transport models that handle simulation of the passage of particles inside detector material. It allows for access to different Monte-Carlo software packages and their geometry descriptions through a unified interface. The geometry has to be defined only once and the user selects which particular transport simulation package is used through a simple flag.

GEANT3 [69] and GEANT4 (GEometry ANd Tracking) [70] [71] are platforms for the simulation of the passage of particles through matter using Monte Carlo methods. Application areas include high energy physics and nuclear experiments, medical, accelerator and space physics studies.

PYTHIA [72] is a high energy collision event generator and decay model. It models collisions of particles, such as electrons, protons, etc. with each other. Physics reaction processes included are, among others, hard and soft interactions of quarks and gluons, parton distributions and parton showers, fragmentation into hadrons as well as decays.

PLUTO [73] [74] is a simulation package for hadronic reactions developed by the HADES collaboration. It is a C++ library for event generation, experimental filters (acceptance, etc.) and particle decays, and can be invoked interactively from ROOT where the output can be analyzed directly or in *batch mode* where the output it generates is passed to GEANT for further simulation.

#### 4.1.2 PandaRoot main code

PandaRoot is the internal PANDA specific part of the simulation program. It implements the geometrical description of the PANDA detectors within the magnetic fields, detector specific hit production and digitization algorithms, as well as track and cluster reconstruction algorithms. Other essential components are the particle identification and analysis packages. It also provides additional event generators not available as external packages. Together with the external packages, it enables complete simulation and reconstruction of  $\bar{p}p$  and  $\bar{p}$  nucleus annihilation reactions.

## 4.2 Simulation steps

For a full simulation of physics process with PandaRoot, the first step is event generation. Depending on physics objective, the events can be produced by any of several available event generators: Evtgen, DPM, PYTHIA, UrQMD, etc. Particles are then propagated through the full detector set-up using the transport simulator GEANT, via the VMC interface.

Detector responses are simulated by digitizers, that translate the hit information into the physical information as provided by the detector in the actual experiment.

Pattern recognition algorithms are then used to look for charged tracks by combining hits from different tracking detectors, after which, the reconstructed tracks are extrapolated to PID detectors.

The combination of the tracks with the reconstructed hit information from the PID detectors forms a list of charged candidates for the particle identification. The sign of the curvature gives the sign of the charge. Clusters of hits detected in the electromagnetic calorimeter and not correlated to charged tracks are supposed to be candidates for neutral particles such as photons or  $\pi^0$ , and will form the list of neutral candidates.

Different independent algorithms assign to each candidate and for each detector a PID probability value for being one of five particle species: electron, muon, pion, kaon or proton. This information is then used by the analysis packages for particle selection based on a probability threshold requirement specified by the user. Finally kinematic and vertex fitters can be run to improve the quality of the analysis results.

### 4.2.1 Event generation

An event generator is a software which produces particles in final states and their momentum vectors for Monte Carlo simulations. Several event generators are available in PandaRoot:

- Box Generator

In this generator, there is no decay chain. One or more particles are emitted with flat angular and momentum distributions. The vertex can be set to a point value or a flat distributions. This generator is used for detector code testing and the determination of particle resolutions and efficiencies in the detectors.

- EvtGen

EvtGen contains entire decay chains. Each decay can be given an underlying decay model, the simplest of which is the phase space distribution. Many decay models for well known particles are present as presets, modifying the distributions of momenta and angles accordingly. It is possible to add user-defined models for specific decays.

This generator has two modes. One is the fast mode, where the four-momentum and position information for each particles are already defined in the input file, PandaRoot only reads this information without real simulation. Another is the normal one, where PandaRoot reads the differential distribution, and simulates the momentum and position distribution itself.

- Dual Parton Model (DPM)

As the name indicates, DPM is an event generator based on the dual parton string model. It can be used to simulate the inelastic and elastic  $\bar{p}p$  collisions according to already known cross sections. It is used to simulate background events, which are necessary to evaluate signal-to-background ratios for specific physics signals.

### 4.2.2 Physics lists from GEANT

GEANT is a general purpose particle transport code, which caters to applications in domains as diverse as medical imaging, radio-protection, and high energy physics detector simulation.

As such it attempts to cover as wide an energy range as possible for projectile particles. For this purpose, GEANT comes with a large selection of physics models and cross sections with finite, yet precisely specified validity domains. This feature is indispensable, because the physics processes that are relevant at different projectile energies are not the same.

The situation for electromagnetic physics models is quite clear [75] with a standard physics list that handles all physics processes relevant at energies of the order of a GeV and above, including multiple scattering, pair creation and Bremsstrahlung and photoelectric effect. The main variations are optimizations to reduce CPU usage on the one hand and to achieve higher accuracy modeling of physics (multiple scattering, ionization) at very low energy scale (few tens of MeV and below) on the other hand.

The situation for hadronic physics models is much more involved with a large selection of physics models and cross sections available to pick from. Here the relevant physics is the scattering of the projectile hadron off a nucleus (elastic or inelastic) and the subsequent cascade decay of the remnant excited nucleus until stability is achieved through various physics mechanisms such as evaporation (emission of neutrons, photons alpha particles etc.), fission when a channel is open and disintegration through explosion models or fermi break up for light nuclei. Unstable nuclear fragments created in the inelastic interaction are followed and decayed in flight. In addition the capture of slow or at rest negative hadrons by nuclei is also handled separately. Depending on the required precision and computing constraints, one can choose from a selection of reference physics lists [76] that combine a carefully selected collection of models and cross sections for each particle species that is appropriate for different applications.

For GEANT3, fully parametric models of hadronic interactions called GEISHA is the most widely used option. GEANT4 deals with theory based and more extensively validated hadronic interaction physics models. The most appropriate models for high energy inelastic scattering of hadrons off nuclei are the QGS (Quark Gluon String) and FTF (Fritiof) string fragmentation models. The validity domain of these models is typically above a few GeV (FTF) and above about 10 GeV (QGSP). In this range, the excited nucleus has to be passed on to a separate module for de-excitation. For lower energies, cascade models that can handle both the inelastic scattering and de-excitation of the wounded nucleus are used, the most widely used ones being the Bertini cascade model and the binary cascade model. In addition, for backward compatibility with GEANT3, the GEISHA packages was reintroduced in GEANT4 under the name LHEP (stands for Low/High Energy Parametrization), but will be removed in subsequent releases of GEANT4, due to the better validation of the more theory based GEANT4 only models.

### 4.2.3 Digitization

Before executing the reconstruction algorithm on the data simulated by the transport package GEANT, a detailed description of the detectors' behavior is needed. The output of the simulation from GEANT is a collection of hits, which contain mainly the intersection points and energy losses of all particles in the individual detector parts. Based on this information, the digitization step models the signals and their processing in the front-end-electronics of the individual detectors, and produces a digitized detector response as similar as possible to the real experimental data.

#### 4.2.3.1 MVD readout

The Micro Vertex Detector (MVD) makes use of two different silicon detector types, silicon strip and pixel detectors. The digitization process steps through two stages, geometric and electronic.

Geometrically, the particle path is projected through the sensor to its surface. As the path crosses the readout structure, the discretisation into pixels or strips is done. The charge collected in each of the channels is parametrized by a Gaussian cloud distribution around the path.

#### 4.2.3.2 STT readout

There are three types of STT digitization options available in PandaRoot, the fast digitization, the realistic digitization and the ideal digitization.

The fast digitization of the Straw Tube Tracker (STT) is performed in a similar way as in the case of the MVD. The STT consist of wires inside an  $Ar/CO_2$  gas (90%/10%) mixture volume. When a charged particle traverses this gas volume, the local helix trajectory is derived from the corresponding GEANT4 intersection points. The drift time of the ionization electrons is estimated from the smallest distance of this helix trajectory to the wire. The uncertainty of the drift time is taken into account by smearing the drift length with a Gaussian distribution with a standard deviation depending on the radial distance as shown in figure 4.2 where radial distance is calculated as the distance between the simulated track and the wire. The average number of primary ionization electrons is the total deposited energy in the gas volume divided by the ionization energy of 27 eV for  $ArCO_2$ . The energy signal of a straw tube is finally calculated using Poisson statistics.

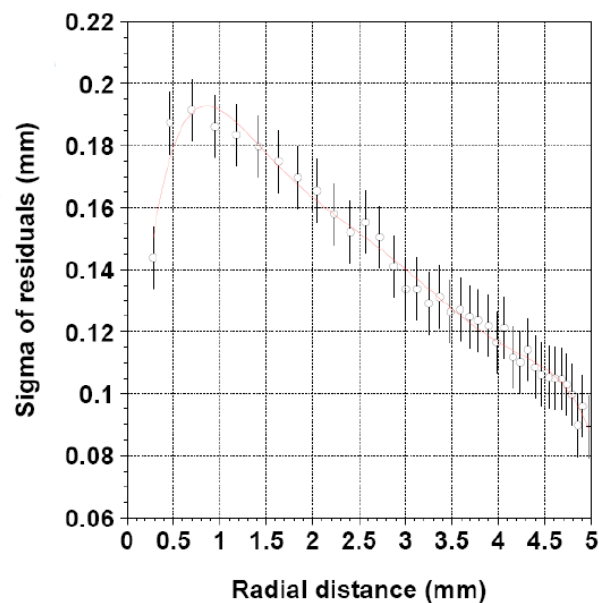


Figure 4.2: Width (sigma) of the residual distributions for different intervals of the radial distances to the wire. The distribution of the arrival time on the anode of the electrons created along the path of particle is narrower when the radial distance is large, so the resolution is better for the large radial distance. From [12].

The real digitization implements a full simulation of the detector response. The full physics of the formation of the electron/ion couples due to ionization and the drift of the produced electrons towards the anode wire and the avalanche formation are simulated. The signal on the wire is simulated, the drift time is computed and the isochrone is reconstructed.

The ideal digitization procedure simply uses the position of the hit from simulation directly without smearing.

#### 4.2.3.3 GEM readout

Each GEM station consists of two detector planes. The distance between the detector planes is 1 cm. It has been assumed that each detector plane has two strip detector layers with perpendicular orientation to each other. In the current implementation, the gas amplification process and the response of the strip detector has not been simulated in detail. Instead, the entry point of a charged track into the detector plane has been taken directly from GEANT4 and smeared with a Gaussian distribution of 70  $\mu\text{m}$  width in the direction of the orientation of each strip.

#### 4.2.3.4 DIRC detectors readout

In the DIRC (which stands for Detector for Internally Reflected Cherenkov light) the light propagation in the Cherenkov radiators, the signal processing in the front-end electronics and the reconstruction of the Cherenkov angle are all modeled in a single step. The resolution of the reconstructed Cherenkov angle  $\sigma_C$  is driven by the uncertainty on the single photon angle  $\sigma_{C,\gamma}$  and the statistics of the relatively small numbers of detected Cherenkov photons  $N_{ph}$ :

$$\sigma_C = \frac{\sigma_{C,\gamma}}{\sqrt{N_{ph}}} \quad (4.1)$$

The single-photon resolution  $\sigma_{C,\gamma}$  and the number of detected photons are pre-calculated in a full simulation and stored in a look up table as a function of  $\theta$  and  $\phi$ . The average value of  $\sigma_{C,\gamma}$  is about 19 mrad. The average number of detected photons for 1 GeV/c pions at a polar angle of 90° is 20 and increases by a factor of 2 for very forward and backward directions.

#### 4.2.3.5 EMC readout

For the EMC in the target spectrometer (barrel EMC) the properties of  $\text{PbWO}_4$  crystals at the operational temperature of  $-25^\circ\text{C}$  have been modeled in the following way. A Gaussian distribution with a  $\sigma$  of 1 MeV has been used for the electronics noise. The statistical fluctuations in the LAAPD were estimated assuming 80 photo-electrons per MeV deposited in a crystal. An excess noise factor of 1.38 has been used, corresponding to the measurements with the first LAAPD prototype at an internal gain of  $M = 50$ . This results in a photo statistics noise term of  $0.41\%/\sqrt{E/\text{GeV}}$ . The digitization was tested with a prototype of the calorimeter that was built from 60 crystals with a complete readout stack, called the PROTO60.

In order to reproduce the energy resolution of the PROTO60, the non-uniformity of the light yield as a function of the longitudinal position of the energy deposit has to be taken into account in the simulation. This effect is important, (1.5 %/cm) and degrades substantially the resolution (from 1.6 to 2.6 % for a photon at 1 GeV). To take this effect into account, a weight depending on the distance of the energy deposit to the entrance surface of the crystal is calculated. The weighted sum of all the energies deposited in the crystal is subsequently used by the calibration task to provide the corrected energy. The raw energy is just the sum of the deposited energies in each crystal, without taking into account the non-uniformity (or any other digitization effects).

### 4.2.4 Reconstruction

After digitization, the three-momentum and position information of each particle in the decay chain needs to be reconstructed for the further analysis. The charged particles and neutral particles are reconstructed in different detectors with different algorithms, using the digitized information in the previous step.

#### 4.2.4.1 Charged particle tracking

The charged particles are reconstructed by merging the information from all the tracking detectors present in the spectrometer. The aim of the reconstruction is to provide the four-momentum of the particle at the interaction point as well as the position where and time when the particles cross the various detector subsystems.

To achieve this aim, the hits produced by the energy deposit in the different detectors are taken as input for the pattern recognition and track reconstruction. The information of the hits include the detector's identification, the hit identification and the radial distance of the hit. Hits are grouped together to identify the original tracks by the following steps:

- Pattern recognition and prefit

This step identifies the hits that belong to the same track and gathers them together. In the region where the solenoidal field is homogeneous, for example in the target spectrometer, it is enough to fit the hits with a helix, since the material budget is small and the field inhomogeneities are negligible. In the dipole region and the transient field region, i.e. the region between the solenoid and the dipole, this is not possible anymore. Some other track representations are needed for instance splines. The purpose of pattern recognition is to give a guess of the track momentum and position.

In PandaRoot there are different pattern recognition procedures. The local one gathers information for each tracking detector. The global one combines information from different detectors. The ideal one takes the information from simulation.

In MVD local pattern recognition, the XY coordinates of the hits are transformed to a Riemann surface, as shown in figure 4.3.

In particular here the XY coordinates are mapped to a circular paraboloid, via the transformation  $w = x^2 + y^2$ . The equation of a circle in the xy plane  $(x - x_0)^2 + (y - y_0)^2 = R_0^2$  becomes  $w - 2x_0x - 2y_0y + x_0^2 + y_0^2 - R_0^2 = 0$ . A plane is fitted to the mapped points and the parameters of the plane are then transformed back to the circle parameters in the xy plane. In a second stage a linear fit with a straight line is made between the arclength of the points on the fitted circle and the Z coordinate of the hits.

The STT pattern recognition proceeds in two steps, using at first the axial straws, then the skewed straws.

In the first step, only the hits of axial wires are used. The X and Y position of the wires and the drift radius define a small circumference in the XY plane (drift circles in figure 4.4) to which the particle trajectory is tangent. They are transformed through a conformal map into a conformal space where tracks which are circles in XY plane become straight lines (see figure 4.5) by using  $u = x/(x^2 + y^2)$  and  $v = y/(x^2 + y^2)$ .

The hits are clustered and each cluster is fitted in the conformal plane. The parameters of the fitted line are transformed back to the circle parameters in the XY plane.

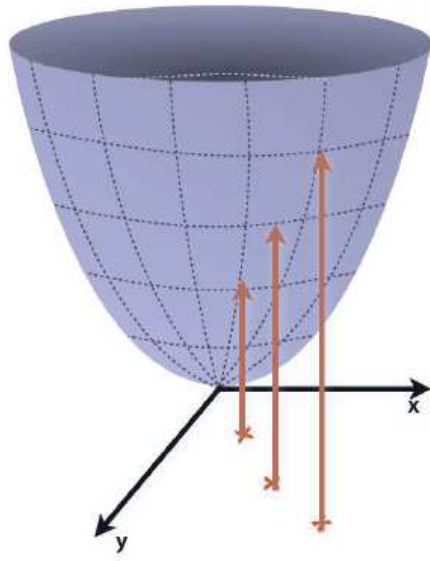


Figure 4.3: Transformation from XY coordinates to a Riemann surface.

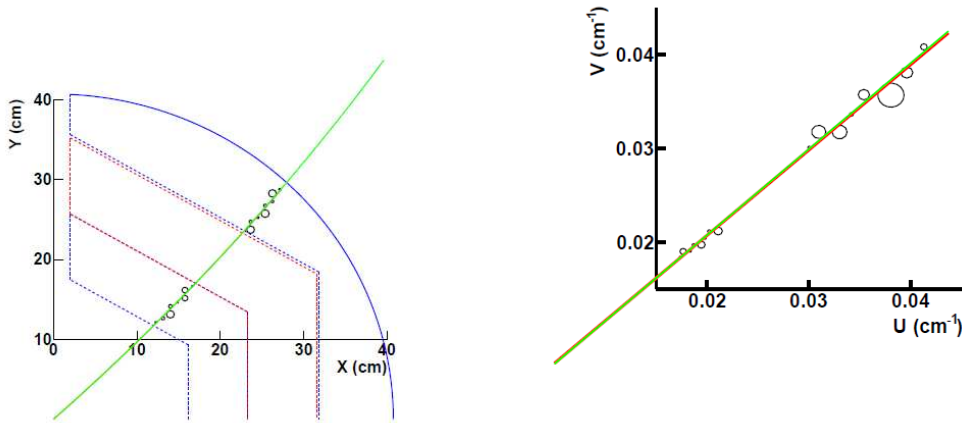


Figure 4.4: Track generated with Monte Carlo at the interaction vertex ( $x = 0$ ,  $y = 0$ ); the small circles are the isochrone circles of the STT axial straws in the XY projection; the track is the circle tangent to all drift circles.

Figure 4.5: The same track as in figure 4.4 plotted after the conformal transformation. The track circle transforms into a straight line, while the drift circumferences transform into circumferences. The track straight line is still tangent to all drift circles. The green line is the Monte Carlo truth, the red line is found by the pattern recognition.

After this stage three of the five parameters of the track helix are known (the radius  $R$ , the positions of the helix center in the XY plane).

In the second step, the remaining two parameters of the helix are determined by using the hits of the skewed STT straws. Due to the geometry and small inclination ( $3^\circ$ ) of the skewed straws the tangency of the straight line essentially occurs at the edges of the

ellipses. The extremities are fitted with a straight line, as shown in figure 4.6.

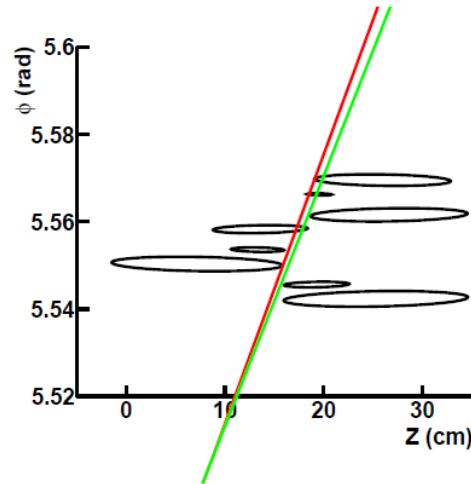


Figure 4.6: The same track as in figure 4.4 plotted in the  $\phi$ -Z plane.

The global pattern recognition contains the information from STT, MVD and GEM. It starts from the MVD and STT standalone track finders. First, it extrapolates the STT hits alone with the helix fit over the MVD hits, then does the same thing for the MVD alone. The new track candidates, of both STT and MVD hits, are refitted with a helix to improve the parameters thanks to the high resolution of the MVD. Once the MVD+STT track are ready, it is extrapolated to the GEM station to collect also the GEM hits. At this stage no refit is done since the GEM stations are in a zone where the field is non homogeneous and so the helix is not suitable for fitting.

- Kalman fit and extrapolation

After the helix prefit step, a Kalman Filter [77] based on GENFIT and GEANE [78, 79] for error estimation and track propagation is used to refine the parameters provided by the prefit.

The Kalman Filter is applied in three steps: first the track parameters and the associated errors at the next detection plane are predicted, using the knowledge at the previous plane. Then a weighted mean between the predicted and the measured values is calculated taking into account the corresponding errors (GENFIT). Eventually, the final parameters of the track at the vertex are deduced from the backward propagation of the particle. For the propagation of the particle in the first and the third step, the GEANE track follower is used. GEANE takes into account energy loss by ionization and the angular deviation due to multiple scattering between two measurement planes. GEANE is processed before the PID information is available, so an arbitrary mass hypothesis is used for the propagation. In our studies, we use the muon mass, so-called  $\mu$  hypothesis.

The comparison of the muon momentum reconstruction result between the Kalman fit and the prefit is given in figure 4.7. In all cases the Kalman fit results are better than the prefit ones, both in terms of mean value and sigma of the distributions. At low momentum, due to the energy loss by ionization, the helix fit introduces a systematic offset in the momentum determination giving an underestimated value. The Kalman Filter suppresses this shift and in addition reduces the width of the distribution. At high momentum region, the

improvement is small but still significant. This is due to the more appropriate weights of the different measurements which take into account the multiple scattering and energy loss. At high momenta, the improvement is smaller, since the dominant error is due to the position measurement, but the effect is still significant.

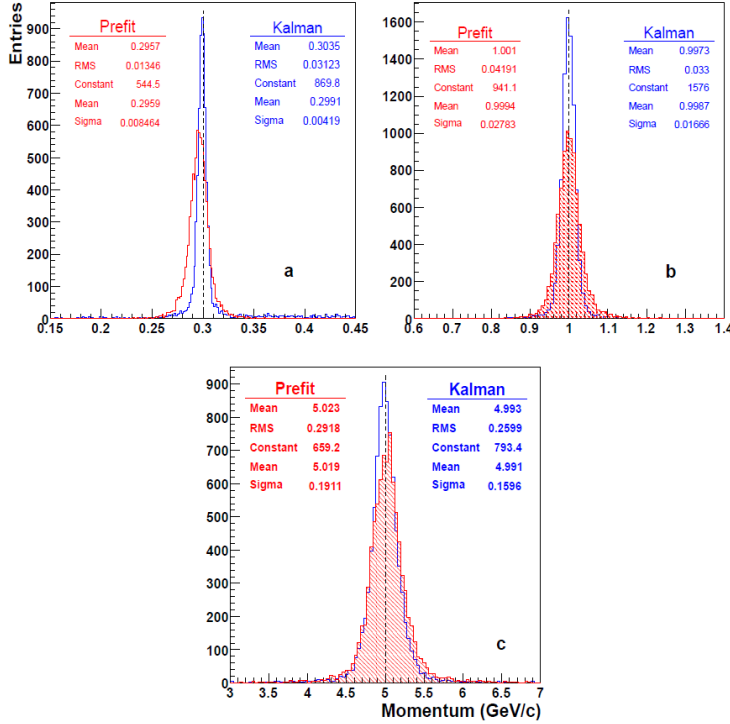


Figure 4.7: Momentum distributions for (a) 0.3, (b) 1 and (c) 5 GeV/c  $\mu^-$ , reconstructed with helix (red dashed) and Kalman (blue) fits. The statistic boxes report the mean values and RMS of the non fitted histograms, as well as mean and sigma values of the Gaussian fits, before and after the Kalman fit.

At a given polar angle  $\theta$ , the momentum resolution in drift chambers

$$\frac{\sigma_p}{p} \sim \frac{\sigma_{p_T}}{p_T} = \frac{K_0}{p_T} \oplus K_1 p_T \quad (4.2)$$

is dominated at high  $p_T$  by the spatial resolution dependent linear term ( $K_1$ ), and at low  $p_T$  by multiple scattering ( $K_0$ ). Both  $K_0$  and  $K_1$  depend on the polar angle,  $K_0$  via the numbers of radiation length traversed by the track and  $K_1$  via the number of hits. The high  $p_T$  linear dependence is a consequence of the relationship between the radius of curvature of a track and the magnetic field strength given by  $0.3B\rho = p_T$ , where B is in Tesla and  $p_T$  is in GeV/c and  $\rho$  in meters. The resolution on the measurement of the radius of curvature becomes worse linearly as the track's momentum increases, because the hits generated by the track become more aligned and measuring the radius of curvature from the hit position measurement becomes more difficult. It can be shown that to first order approximation,  $K_1$  is roughly proportional to the spatial resolution of the hits. Figure 4.8 shows the momentum resolution of the full Kalman filter procedure using STT hits as a function of  $p_T$ . The results are averaged over polar and azimuthal angles covering the full Barrel region. The global trend can be qualitatively understood based

on the above discussion. The increase as a function of  $p_T$  for  $p_T > 400\text{MeV}/c$  is indeed clearly due to the increasing effect of the error on the measurements, while the resolution is worse for the lowest momenta due to the effect of multiple scattering. However, the detailed interpretation is difficult due to the average over different geometrical regions where both the numbers of hits and the track length are different.

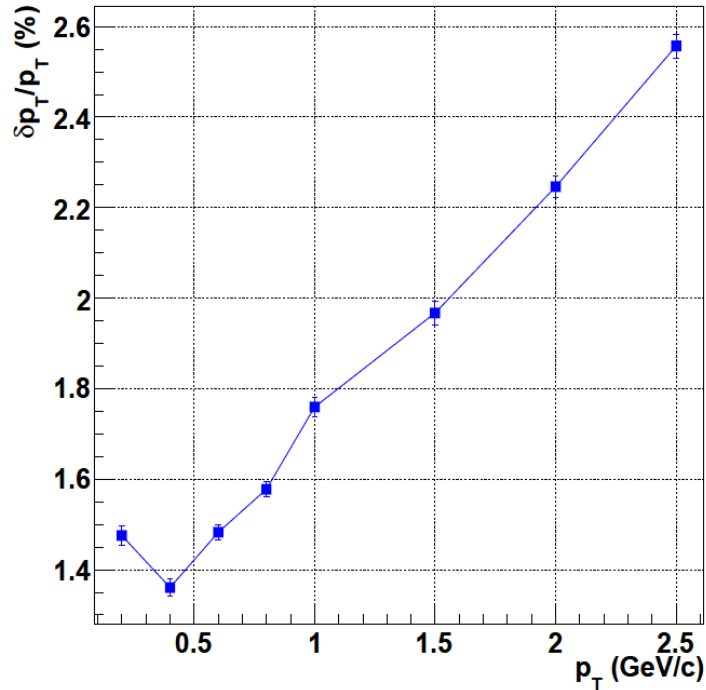


Figure 4.8: Momentum resolution vs  $p_T$  for  $\mu^-$  single track events, in the angular ranges  $\phi \in [0^\circ, 360^\circ]$  and  $\theta \in [7^\circ, 160^\circ]$ .

The momentum resolution of the whole reconstruction procedure as a function of polar angle is shown in figure 4.9. The resolution improves for  $\theta$  values up to  $21^\circ$ , then starts to worsen again. The results can be interpreted on the basis of geometrical considerations. We start the discussion with the result obtained at 5 GeV/c, where the momentum resolution is driven by the position measurement ( $\frac{\sigma_p}{p} = K_1 p_T = K_1 p \sin\theta$ ). The resolution follows basically the number of hits.

For  $\theta < 11.6^\circ$ , there is no reconstruction of the  $z$  coordinate of the straw tube hits, which results in a bad spatial resolution of the STT hits. Therefore, the tracking in this forward angular region is performed mainly with the hits produced in the MVD and in the GEM chambers.

For  $11.6^\circ < \theta < 21^\circ$ , as the  $\theta$  value increases, tracks cross more and more straw tube layers, allowing a better track reconstruction in the tracker. Combined with the good resolution of the MVD and GEM hits, it results in a better global momentum resolution.

For  $21^\circ < \theta < 133^\circ$ , tracks traverse the MVD and all the straw layers; so the resolution obtained by the STT alone is improved with respect to that at lower  $\theta$  values, but it suffers from the fact that there are no more hits in the GEM chambers. So the resolution is globally a bit worse. The trend in  $\sin\theta$  is due to the fact that the coefficient  $K_1$  is constant in this region since the number of hits is constant.

Finally, for  $\theta > 133^\circ$  tracks are going in the backward direction and traverse a lower number of straw layers as the angle increases: Consequently, and since the decreased number of hits is not compensated by any other outer tracking detectors (like the GEMs in the forward direction), the resolution becomes worse.

At low momenta, the contribution of the position uncertainty decreases while the contribution of the multiple scattering increases. The evolution of multiple scattering contribution as a function of position is  $1/\cos\theta$  in Forward and Backward region and  $1/\sin\theta$  in the Barrel region. This results in an overall decrease of the momentum resolution as a function of  $p$ , except for the region below  $22^\circ$ , where the effect of the multiple scattering is higher. This results in a momentum resolution which is almost independent on the momentum for  $p \leq 2$  GeV/c in this region. In the Barrel region, the multiple scattering effect goes as  $1/\sin\theta$ , which leads to a flattening of the curve when the momentum decreases.

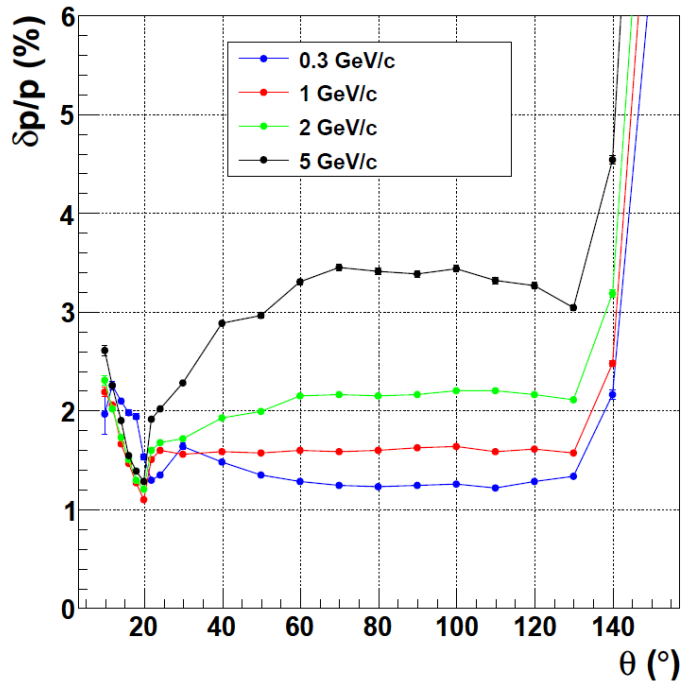


Figure 4.9: Momentum resolution as a function of polar angle ( $\theta$ ) for 0.3, 1, 2, 5 GeV/c  $\mu^-$  single track events, in the full angular range  $\theta \in [9^\circ, 160^\circ]$

#### 4.2.4.2 Cluster reconstruction EMC

A photon or electron entering one scintillator module of the EMC develops an electromagnetic shower which, in general, extends over several modules. A contiguous area of such modules is called a cluster. The energy deposits and the positions of all scintillator modules in a cluster allow a determination of the four vector of the initial photon. Most of the EMC reconstruction code used in the offline software is based on the cluster finding and bump splitting algorithms which were developed and successfully applied by the BaBar experiment.

The first step of the cluster reconstruction is the finding of a contiguous area of scintillator modules with an energy deposit. The algorithm starts at the module exhibiting the largest

energy deposit. Its neighbors are then added to the list of modules if the energy deposit is above a certain threshold  $E_{xtl}$ . The same procedure is continued on the neighbors of newly added modules until no module fulfills the threshold criterion. Finally a cluster gets accepted if the total energy deposit in the contiguous area is above a second threshold  $E_{cl}$ .

The next step is the search for bumps within each reconstructed cluster. A cluster can be formed by more than one particle if the angular separation of the particles is small. In this case the cluster has to be subdivided into regions which can be associated with the individual particles. This procedure is called the bump splitting. A bump is defined by a local maximum inside the cluster: The energy deposit of one scintillator module  $E_{local}$  must be above  $E_{max}$ , while all neighbor modules have smaller energies. In addition the highest energy  $E_{Nmax}$  of any of the  $N$  neighboring modules must fulfill the following requirement:

$$0.5(n - 2.5) < E_{Nmax}/E_{local} \quad (4.3)$$

The total cluster energy is then shared between the bumps, taking into account the shower shape of the cluster. For this step an iterative algorithm is used, which assigns a weight  $w_i$  to each scintillator module, so that the bump energy defined as  $E_b = \sum_i w_i E_i$ . Where  $E_i$  represents the energy deposit in the  $i^{th}$  module and the sum runs over all modules within the cluster. The module weight for each bump is calculated by

$$w_i = \frac{E_i \exp(-2.5r_i/r_m)}{\sum_j E_j \exp(-2.5r_j/r_m)} \quad (4.4)$$

Where  $r_m$  is the Moliere radius of the scintillator material,  $r_i$  and  $r_j$  are the distances of the  $i^{th}$  and  $j^{th}$  module to the center of the bump, and index  $j$  runs over all modules. This procedure is iterated until convergence. The center position is always determined from the weights of the previous iteration and convergence is reached when the bump center stays stable within a tolerance of 1 mm.

The spatial position of a bump is calculated via a center-of-gravity method. The radial energy distribution, originating from a photon, decreases mainly exponentially. Therefore, a logarithmic weighting with  $W_i = \max(0, A(E_b) + \ln(E_i/E_b))$  was chosen, where only modules with positive weights are used. The energy dependent factor  $A(E_b)$  varies between 2.1 for the lowest and 3.6 for the highest photon energies.

The optimal choice for the three photon reconstruction thresholds depends strongly on the light yield of the scintillator material and the electronics noise. To detect low energetic photons and to achieve a good energy resolution, the thresholds should be set as low as possible. On the other hand, the thresholds must be sufficiently high for a suppression of misleadingly reconstructed photons originating from the noise of the readout and from statistical fluctuations of the electromagnetic showers. The single crystal threshold was set to 3 MeV of deposited energy, corresponding to the energy equivalent of  $3\sigma$  of the electronics noise. All reconstruction thresholds for the target spectrometer (TS) EMC as well as for the forward (FW) EMC are listed in Table 4.1 .

	TS EMC	FW EMC
$E_{xtl}$	3 MeV	8 MeV
$E_{cl}$	10 MeV	15 MeV
$E_{max}$	20 MeV	10 MeV

Table 4.1: Reconstruction thresholds for the PbWO<sub>4</sub> and Shashlyk calorimeters.

### 4.2.5 Particle identification

Good particle identification (PID) for charged hadrons and leptons plays an essential role for  $\overline{\text{P}}\text{ANDA}$  and must be guaranteed over a large momentum range from 200 MeV/c up to approximately 10 GeV/c. The information from EMC, DIRC and the dE/dx measurement in STT and MVD are complementary. While energy loss measurements within the trackers yield good criteria for the distinction between the different particle types below 1 GeV/c, the DIRC detector is the most suitable device for the identification of particles with momenta between 1 and 3 GeV/c. In combination with the tracking detectors, the EMC is the most powerful detector for an efficient and clean electron identification, and the Muon detector is designed for the separation of muons from the other particle species. The best PID performance however can only be obtained by taking into consideration all available information of all sub detectors.

The PID software is divided in two different parts. In the first stage the PID probabilities are determined for each detector individually, so that for each charged candidate, probabilities for all five particle hypothesis (e,  $\pi$ ,  $\mu$ , K and p) are provided. The probabilities are normalized to one and the same flux is assumed for each particle species. In the second stage the global PID probabilities are calculated by combining this information and applying a standard likelihood method. The global PID probabilities allows an optimization of efficiency and purity, depending on the requirements of the particular physics channel under study.

#### 4.2.5.1 dE/dx measurement in STT and MVD

The energy loss of particles in thin layers of material directly provides an access to the dE/dx. As can be seen directly from the Bethe-Bloch formula, for a given momentum, particles of different types have different specific energy losses, dE/dx. This property can be used for particle identification, as illustrated in figure 4.10.

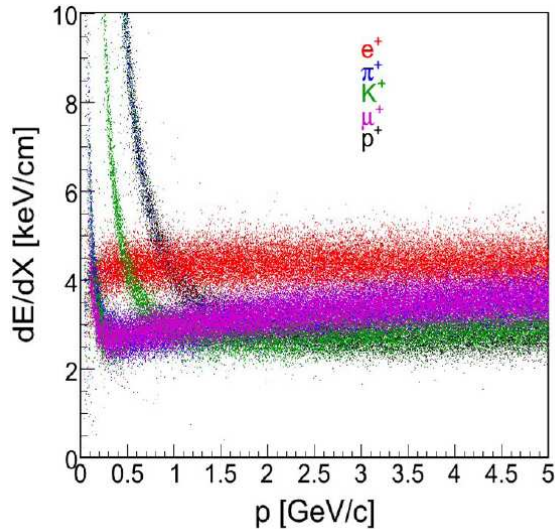


Figure 4.10: Typical truncated dE/dx plot as a function of momentum for the 5 particle types.

The method however has two limitations. First of all, there is no possibility to disentangle between two particles at the crossing points of their respective dE/dx curves. Secondly, the distribution of the specific energy loss displays a long tail following a Landau probability

distribution which constitutes a limitation to the separation, especially for particles with large domain in yields.

In PANDA, two detectors will give access to a  $dE/dx$  measurement, the MVD detector setup, and the central spectrometer tracking system (STT). The STT provides more than 20 measurements of  $dE/dx$  for each track whereas the MVD provides only 4 to 6. As stated above, using large measured  $dE/dx$  values can lead to a bias on the average, resulting in a loss of separation power between particle species, since all particles have a long  $dE/dx$  tail. On the other hand throwing away measurements lowers the statistical accuracy on the average. As a compromise, the top 30% of the  $dE/dx$  measurements in the STT are discarded track by track before the average STT  $dE/dx$  is calculated. In contrast, since the maximum possible number of  $dE/dx$  measurements from the MVD is already small, all available values are used to calculate the average MVD  $dE/dx$ .

#### 4.2.5.2 PID in DIRC

Cerenkov detectors work on the principle that particles that moved faster than the local light speed emit light. Those photons are emitted at angles that depend on the speed of the particles as shown in figure 4.11. Combined with the momentum information from tracking, the reconstructed Cerenkov angle in the DIRC is used for particle identification.

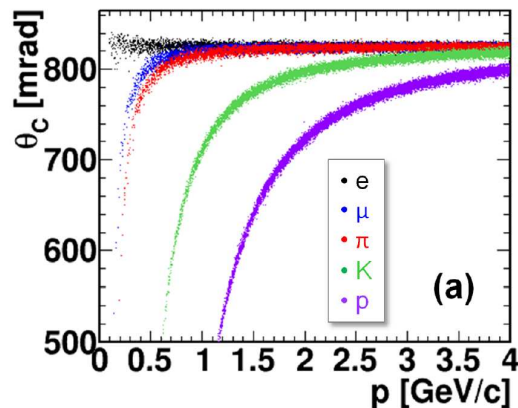


Figure 4.11: Reconstructed track's Cerenkov angle for  $e$ ,  $\mu$ ,  $\pi$ ,  $K$  and  $p$ .

#### 4.2.5.3 PID in EMC

The difference in the amount of energy deposited in the EMC by electrons, muons and hadrons of the same momentum provides the possibility of particle identification. While muons and hadrons in general lose only a certain fraction of their kinetic energy by ionization processes, electrons deposit their complete energy in an electromagnetic shower. The ratio of the measured energy deposit in the calorimeter to the reconstructed track momentum ( $E/p$ ) will be approximately unity to within detector resolution. Due to the fact that hadronic interactions can take place, hadrons can also have a higher  $E/p$  ratio than expected from ionization only. Figure 4.12 shows the reconstructed  $E/p$  fraction for electrons and pions as a function of the momentum.

The shower shape of a cluster is also helpful to distinguish between electrons, muons and hadrons. Since the chosen size of the scintillator modules corresponds to the Moliere radius of

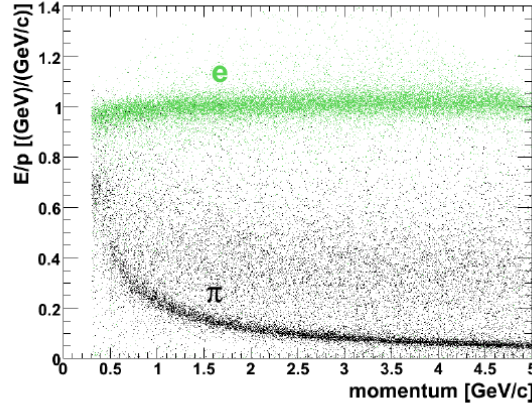


Figure 4.12:  $E/p$  versus track momentum for electrons (green) and pions (black) in the momentum range between 0.3 GeV/c and 5 GeV/c.

the material, the largest fraction of an electromagnetic shower originating from an electron is contained in just a few modules. In contrast, a hadronic shower with a similar energy deposit is less concentrated. These differences are reflected in the shower shape of the cluster, which can be characterized by different properties like  $E1/E9$  (the ratio of the energy deposited in the central scintillator module and in the  $3 \times 3$  module array containing the central module and the first innermost ring), Lateral moment and Zernike moments.

Lateral moment is defined by:

$$P_{lat} = \frac{\sum_{i=3}^n E_i r_i^2}{\left( \sum_{i=3}^n E_i r_i^2 + E_1 r_0^2 + E_2 r_0^2 \right)} \quad (4.5)$$

where  $n$  is the number of crystals associated to the shower,  $E_i$  is the deposited energy in the  $i^{th}$  crystal, and  $r_i$  is the lateral distance between the central and  $i^{th}$  crystal and  $r_0$  is the average distance between two crystals.

A set of Zernike moments describe the energy distribution within a cluster by radial and angular dependent polynomials.

Unlike in other PID detectors where the PID parameter can be fitted by an analytic function, in EMC the distribution of the PID parameters is not easy to fit with analytic functions. Another method named Bayesian classifier is used. This method has been developed in Orsay by Ronald Kunne [80]. The main idea of this method is to perform full simulation of the response of the EMC for the five different particle species, and to map each cell in the discretized space of possible measurements of  $(p, E/p, L, Z, \dots)$  where  $L$  is the Lateral moment and  $Z$  is the Zernick moments) with a probability for each species of particle that depends on the relative yield of the species of particle compared to the others in that particular cell.

In practice, due to the excessive amount of simulation that would be required to fill the space of measurements completely, the probabilities are determined only in pairs of parameters ( $E/p$  vs.  $p$ ), ( $L$  vs.  $p$ ) etc... and combined by taking the product of probabilities for each parameter pairing. As an example, figure 4.13 shows the yield distribution of  $E/p$  vs.  $p$  for a simulation of identical statistics of the five positive particle species considered. The distributions of the negative particles are almost equivalent, except for anti-protons due to the annihilation process.

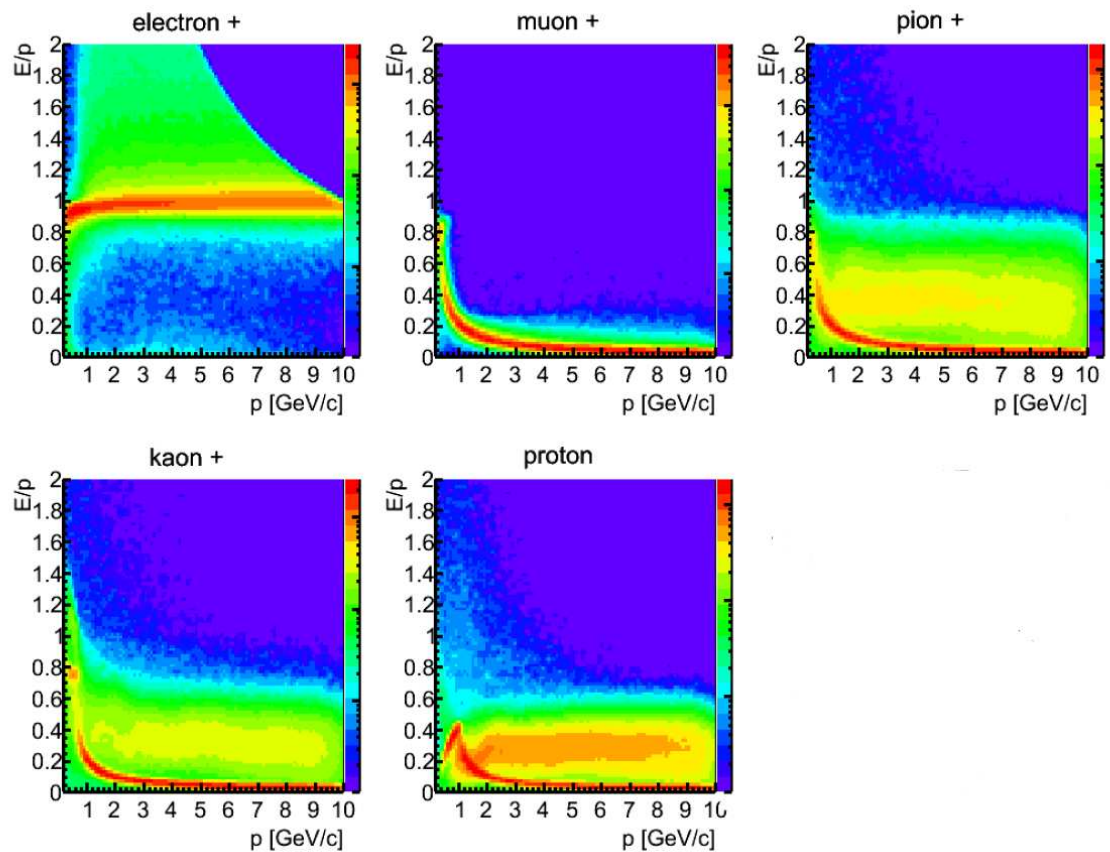


Figure 4.13: The yield of particles as a function of  $p$  and  $E/p$  based on a simulation of equal statistics samples of each of the five particle species. The electron distribution stands out very distinctively from the other particles, suggesting that the  $E/p$  information from the EMC is mostly going to be useful to identify electron from all other particle species.

For instance, the probability for a track to be an electron given measured values of  $E/p$  and  $p$  is calculated as:

$$P(e|E/p, p) = \frac{Y(e|E/p, p)}{\sum_{\xi=e,\mu,\pi,K,p} Y(\xi|E/p, p)} \quad (4.6)$$

where  $Y(\xi|E/p, p)$  is the yield of particle species  $\xi$  in the cell corresponding to  $E/p$  and  $p$ . The probability distribution thus extracted is shown in figure 4.14. Finally the equation to calculate the combined probability from all the variables is:

$$\frac{P(e|E/p, p, L, Z)}{1 - P(e|E/p, p, L, Z)} = \frac{P(e|E/p, p)}{1 - P(e|E/p, p)} \cdot \frac{P(e|L, p)}{1 - P(e|L, p)} \cdot \frac{P(e|Z, p)}{1 - P(e|Z, p)} \quad (4.7)$$

One can distinguish in the  $(E/p, p)$  plane the region where the probability for an electron is close to 1 and others where this probability is close to 0. This shows that  $E/p$  is a good variable in association with  $p$  for particle identification.

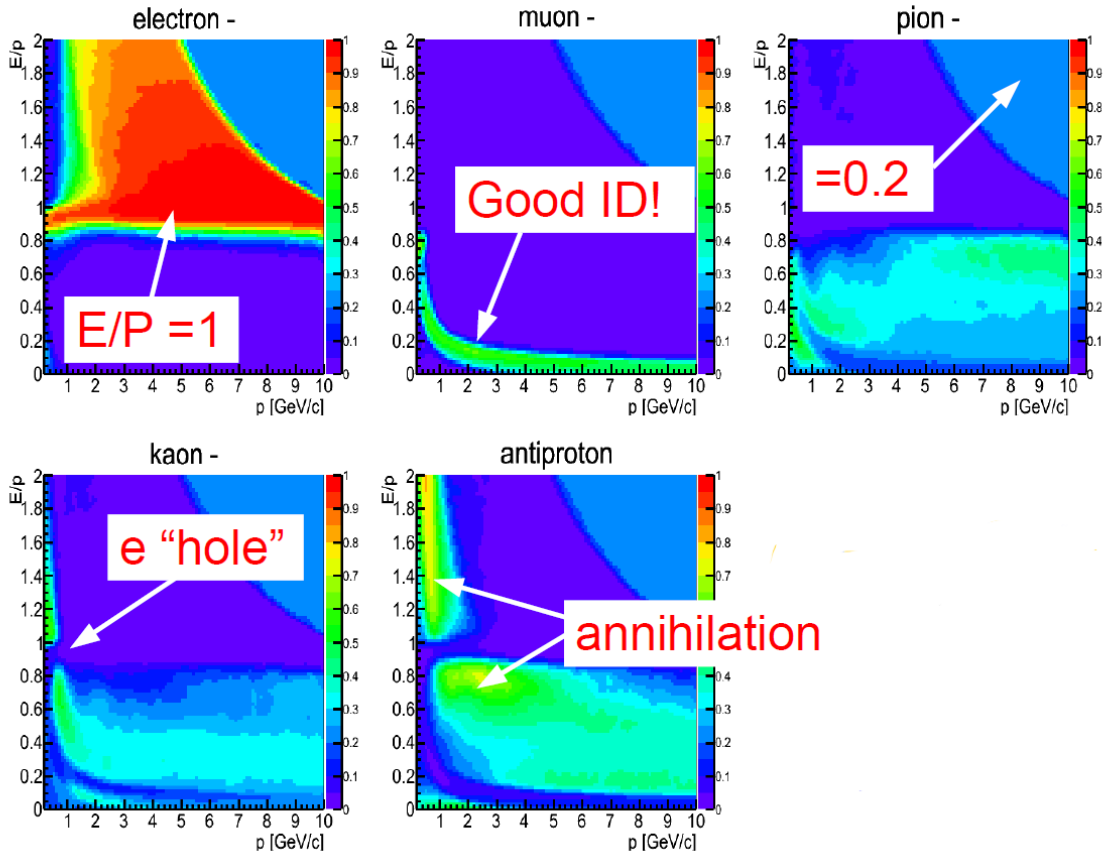


Figure 4.14: Probability of identification for the five particle species as function of momentum and  $E/p$  using the Bayesian classifier method as extracted from the distributions in figure 4.13 using Eq. 4.7.

#### 4.2.5.4 Global PID

The global PID, which combines the relevant information of all sub detectors associated with one track, has been realized with a standard likelihood method. Based on the likelihoods obtained by each individual sub detector the probability for a track originating from a specific particle type  $p(k)$  is evaluated from the likelihoods as follows:

$$p(k) = \frac{\prod_i p_i(k)}{\sum_j \prod_i p_i(j)} \quad (4.8)$$

where the product with index  $i$  runs over all considered sub detectors and the sum with index  $j$  over the five particle types  $e$ ,  $\mu$ ,  $\pi$ ,  $K$  and  $p$ .

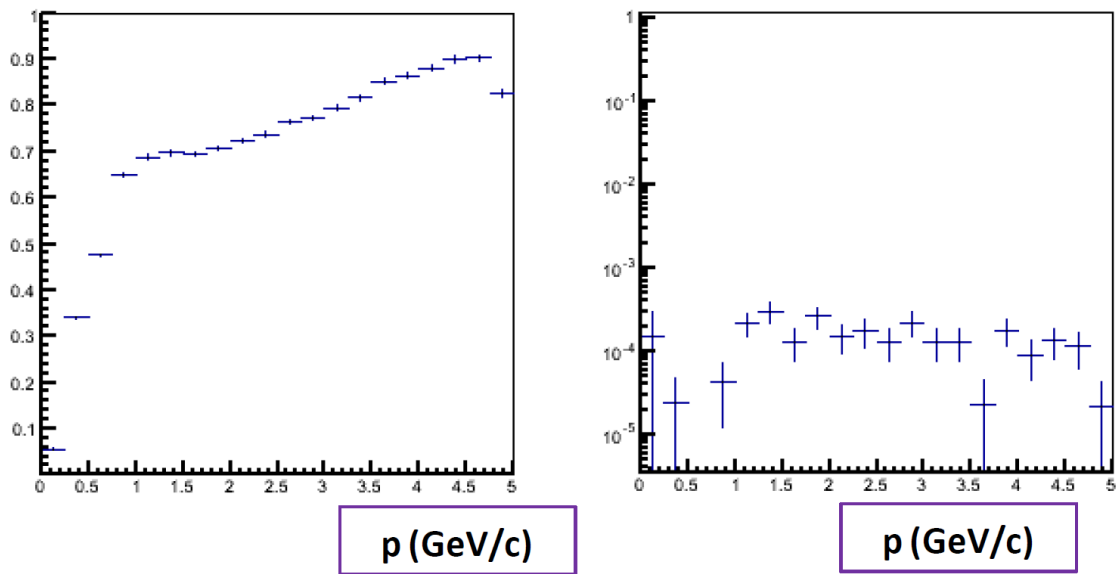


Figure 4.15: The remaining proportion of electron (left) and pion (right) after the PID probability cut using the Bayesian method.

There is a good performance for the pion/electron identification. As shown in figure 4.15, the efficiency for the electron identification is globally over 60%. Applying a cut on the electron probability, the rejection power for pions is better than  $3 \cdot 10^{-4}$ . This is important for the electromagnetic channels' feasibility studies.

### 4.3 Tracking acceptance and efficiency studies

To better understand the tracking operation and efficiency for the studies performed in this thesis, the performance of PandaRoot framework over the acceptance of central tracker (STT), in particular the effect of secondary particle production in the central tracker on track finding efficiency are checked. Simulations of  $e^-$ ,  $\mu^-$  and  $\pi^-$  with 15000 events of each with box generators are used. For the mass of the particles, the  $\mu$  hypothesis is used. The range of parameters used in the box generator are  $p \in [0.15, 5]$  GeV,  $\theta \in [5^\circ, 140^\circ]$  and  $\phi \in [0^\circ, 360^\circ]$ .

### 4.3.1 STT acceptance

The STT acceptance was studied by the distribution of the number of hits per event with the  $\mu^-$  simulation. This was done mainly to check the STT geometrical information. The results are shown in figure 4.16 and 4.17. The distribution in  $\theta$  shows a flat behavior with a constant mean numbers of STT tubes fired in the range of  $20.9^\circ < \theta < 133.6^\circ$ . The results in the  $\phi$  distribution are in agreement with the ones as a function of  $\theta$ . The hole at  $\phi = 90^\circ$  and the low number of hits around this  $\phi$  value are due to the gap in the tracker to create a passageway for the target pipe. The losses at  $\phi = 30^\circ$  and  $\phi = 150^\circ$  are caused by the fact that the short tubes placed in the hexagon corners do not completely fill the volume, leaving empty spaces.

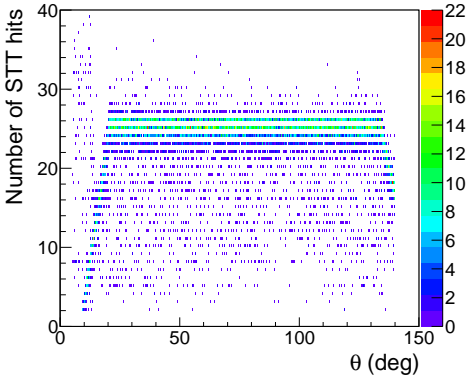


Figure 4.16: Distribution of STT hits as a function of  $\theta$ .

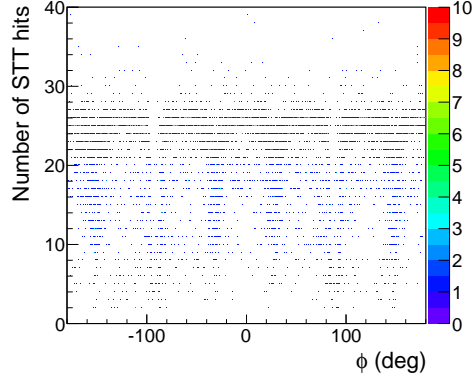


Figure 4.17: Distribution of STT hits as a function of  $\phi$ .

The STT hit multiplicity as a function of transverse momentum is shown in figure 4.18. The large number of hits in the low transverse momentum region is due to tracks with large curvature going back into the tracker without reaching the EMC due to the strong magnetic field. Tracks with momentum lower than approximately 150 MeV/c do not reach the EMC. As a consequence, the EMC can not be used for PID for such tracks.

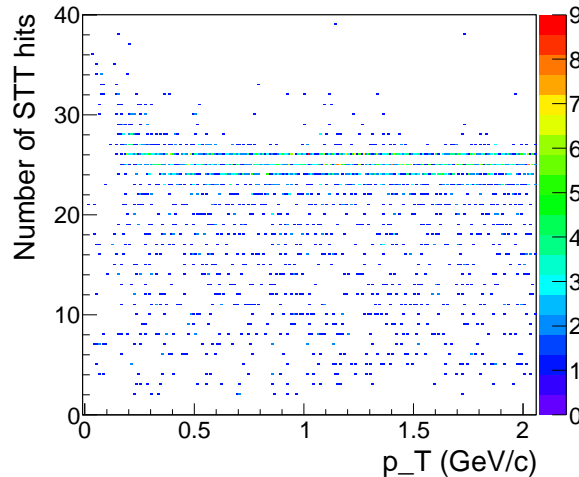


Figure 4.18: Distribution of STT hits as a function of transverse momentum.

### 4.3.2 Track finder purity study

For one single particle, sometimes there are more than one track reconstructed. Some of these multiple tracks correspond to the secondary particles. We investigate here this effect. To get this information, the PDG code of each track which do not correspond to the primary particle is plotted. In each case 15000 particles were generated.

For  $\mu^-$  at our simulated energy, the dominant processes are ionization and multiple scattering in the detector material. Therefore the only expected secondary particles are delta electrons which might be produced in the ionization process.

For  $\pi^-$ , the result is given in figure 4.19 and 4.20. The main secondary particles are pions, muons, electrons and protons. GEANT gives also the physics process information for each secondary particles. Table 4.2 gives the different physics processes that can create the different secondary particles in the  $\pi^-$  simulation. For charged pions, secondary pions and protons are produced by hadronic interactions. Muons are produced in the decay of pions and electron positron pairs come from photon interaction when a photon is created by a hadronic interaction. Additional electrons are due to delta electrons or Compton scattering.

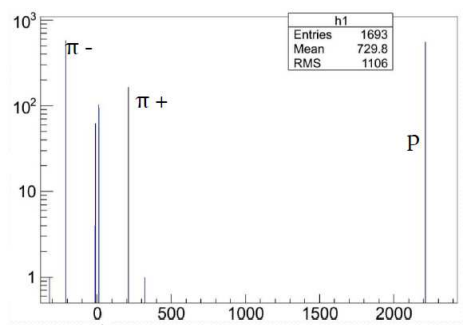


Figure 4.19: PDG code distribution of secondary particles for a primary  $\pi^-$ .

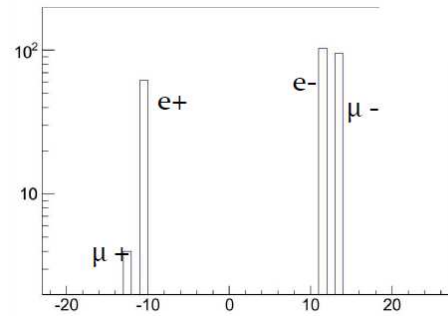


Figure 4.20: A zoom of figure 4.19 in the region where the PDG code is between -20 and 20.

Physics process	secondaries for a primary $\pi^-$
Particle decay	$\mu^+, \mu^-$
Pair production	$e^+, e^-$
Compton scattering	$e^-$
Delta ray production	$e^-$
Hadronic interaction	$\pi^+, \pi^-, p$

Table 4.2: The origin of secondaries for a primary  $\pi^-$ .

The secondary particles from electrons are shown in figure 4.21. Unlike  $\pi^-$ , electrons have only electromagnetic interaction with the material of detector. So the secondary particles are electrons, positrons and photons. The origin processes at the different secondaries are shown in table 4.3.

Electrons are also producing a lot of photons as will be shown in next chapter.

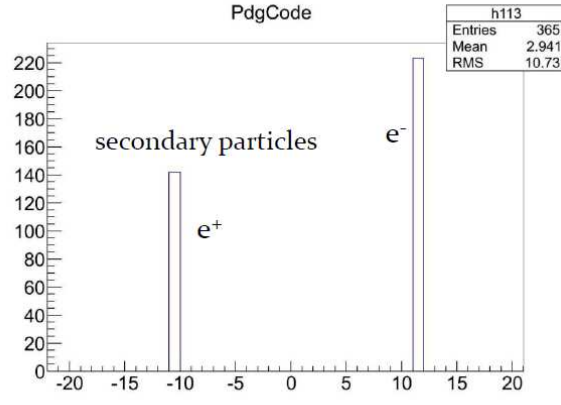


Figure 4.21: The same plot as figure 4.19 for a primary  $e^-$ .

Physics process	secondaries for a primary $e^-$
Pair production	$e^+, e^-$
Compton scattering	$e^-$
Delta ray production	$e^-$

Table 4.3: The origin processes at the secondaries for a primary  $e^-$ .

### 4.3.3 Tracking efficiency

For most events, the reconstruction with  $\mu$  hypothesis gives one reconstructed track per simulated track. However a small fraction of events is reconstructed with more than one track and another small fraction of events is reconstructed with no tracks. For the first case (more than one reconstructed track per simulated track), we consider only tracks with most of the points belonging to the primary MC track and using a track check process to choose the track with a momentum closest to the simulated track. The loss of efficiency of the track finder is due to the second case. The aim of this study is to look at the reason for this inefficiency for different particles.

Figures 4.22, 4.23 and 4.24 give the distribution of track finder efficiency for  $\mu$ ,  $e$  and  $\pi$ . The gaps at  $\phi = -90^\circ$  and  $90^\circ$  and the efficiency loss at small polar angle is due to the acceptance of STT detector. Inside the acceptance of the STT, the efficiency is homogeneous for these three particles. Muons have the best efficiency and pions have the worst one. This effect is due to the interactions of different particles with material of detector (see section 3.2). The efficiencies inside the STT acceptance are given in table 4.4.

Particle	Track finder efficiency
$\mu$	99.2%
$e$	98.6%
$\pi$	95.6%

Table 4.4: Track finder efficiency inside the STT acceptance for  $\mu$ ,  $e$  and  $\pi^-$ .

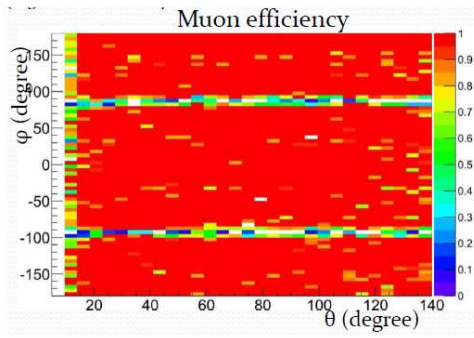


Figure 4.22:  $\theta$  and  $\phi$  distribution of track finder efficiency for  $\mu^-$ .

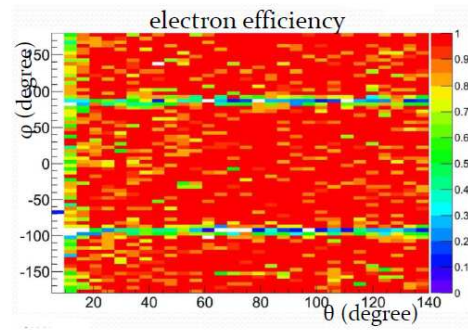


Figure 4.23: The same plot as figure 4.22 for  $e^-$ .

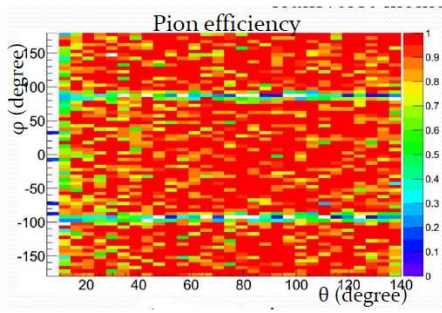


Figure 4.24: The same plot as figure 4.22 for  $\pi^-$ .

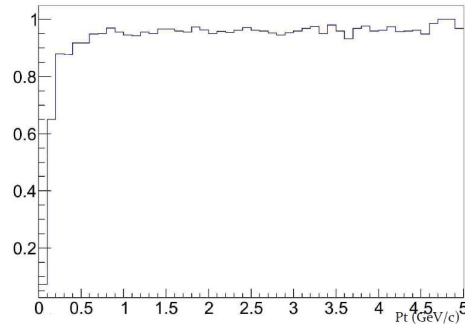


Figure 4.25: Transverse momentum distribution of track finder efficiency for  $\pi^-$ .

Figure 4.25 gives the distribution of track finder efficiency as a function of transverse momentum for pions inside the STT acceptance. The inefficiency at the region of  $p_T < 150 \text{ MeV}/c$  is due to the fact that the low energy particle curl in the STT due to the effect of the magnetic field. The efficiency loss from 150 MeV to 500 MeV is due to the multiple scattering.

If we remove the particles with interaction with detectors, the efficiencies for the three particles are compatible as shown in table 4.5, since we estimate a statistic error of 0.2% on these numbers.

Particle	Track finder efficiency
$\mu$	99.2%
e	98.9%
$\pi$	98.9%

Table 4.5: Track finder efficiency inside the STT acceptance for  $\mu$ , e and  $\pi^-$  for particles without interaction with detectors.

## 4.4 Conclusion

In this chapter, we have described the simulation and analysis tool and some important result are shown. We understand the tracking system acceptance and the efficiency effect. There is no specific problem for the track finding. We have also discussed the properties of momentum resolution for the case of muons. In the next chapter, we will investigate the problems related to the electron momentum reconstruction.

---

## Chapter 5

# Electron bremsstrahlung correction method

As seen previously, electromagnetic channels in  $\bar{p}p$  annihilation and in particular channels with an  $e^+e^-$  pair in the exit channel, like  $\bar{p}p \rightarrow e^+e^-$  or  $\bar{p}p \rightarrow e^+e^-\pi^0$  can be used to study the proton structure. The detection of an  $e^+e^-$  pair is also needed for the study of charmed meson decays of the type  $Y \rightarrow J/\Psi X \rightarrow e^+e^-X$ . In both cases, a high quality electron reconstruction is crucial to improve the signal detection efficiency. For the selection of such exclusive reactions, the main background is due to the production of a  $\pi^+\pi^-$  pair which is typically  $10^6$  times larger than the production of an  $e^+e^-$  pair. This puts very high demand both on Particle Identification (PID) capabilities and four momentum reconstruction resolution which is crucial to use the kinematical constraints for signal selection.

However, the quality of the electron momentum reconstruction is limited due to the bremsstrahlung effect in the detectors. The goal of this chapter is to describe a new method based on the bremsstrahlung photon detection to correct the electron momentum event by event. All the simulation and analysis results shown here are based on PANDARoot version 23756 (10 February 2014). These studies concern the central tracking system which has the highest acceptance.

In section 5.1, we present a status of the electron momentum reconstruction in the PANDA experiment and discuss the problem introduced by bremsstrahlung. The correction method is described in section 5.2 and resulting improvements on the momentum resolution are shown in section 5.3. Examples of application of the method to selected electromagnetic channels are given in section 5.4.

### 5.1 Electron momentum reconstruction in the PANDA central tracking system

As discussed in chapter 2, the central tracking system of PANDA includes three types of detectors: the Straw Tube Tracker (STT), the Micro Vertex Detector (MVD) and the Gas Electron Multiplier-based detectors (GEM) [12]. The central tracking system can be divided into two parts, the Barrel region ( $22^\circ < \theta < 140^\circ$ ) and the Forward Endcap region ( $5^\circ < \theta < 22^\circ$ ).

The general method of momentum reconstruction, based on Kalman Filter with GEANE as track follower, has been presented in section 4.2.4.1. The general features of the momentum resolution have also been discussed. Here, we will study in more details the case of electron momentum reconstruction.

---

### 5.1.1 Bremsstrahlung effect in the PANDA central tracking system

Unlike other charged particles for which the dominant causes of worsening momentum and angular resolution are multiple scattering and position measurement uncertainty, the electron tracking resolution is strongly affected by bremsstrahlung effect.

When an electron travels through materials, it has a high probability to emit one or several photons which take away a non negligible part of its energy. Bremsstrahlung is an inelastic process which is due to the electromagnetic interaction between the electron and the nuclei in the material.

#### 5.1.1.1 Bremsstrahlung description in Geant

The results presented in the following have been obtained with GEANT3.

In GEANT3, the differential cross-sections depending on the photon energy are taken from the Seltzer-Berger tabulations [81] up to 10 GeV and at higher energies from the screened Bethe-Heitler analytical function together with Migdal corrections [69]. The photon angular distribution is taken from an approximation of the Tsai differential cross-section [82].

The main differences in the standard GEANT4 electromagnetic model is first that there is a smooth transition between the Seltzer-Berger model and the screened Bethe-Heitler model in the 1 GeV~10 GeV region and, second, the Landau-Pomeranchuk effect, which is due to the multiple scattering and reduces the cross-section, is introduced above 1 GeV.

#### 5.1.1.2 Material budget in the central tracker

The bremsstrahlung effect depends both on the momentum of the electron and on the thickness of the material in units of radiation length.

The central tracking system is made of detectors with different materials. The distribution of radiation length as a function of polar angle is shown in figure 5.1.

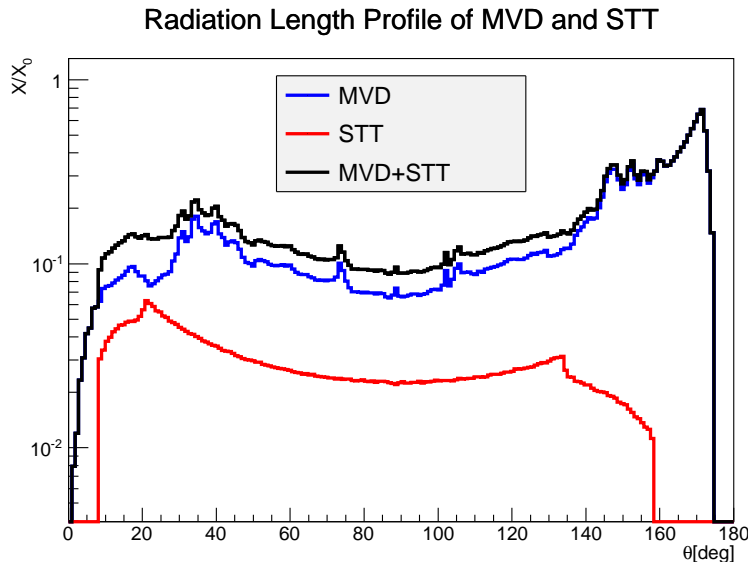


Figure 5.1: The number of radiation length seen by an electron traversing the MVD+STT (black), STT (red) and MVD (blue) detectors in units of radiation length.

It can be seen that the MVD contribution dominates at all polar angles. For STT, one can distinguish three different trends: an increase in  $1/\cos\theta$  in the Forward Endcap region ( $\theta < 22^\circ$ ), a  $1/\sin\theta$  trend in the Barrel region ( $22^\circ < \theta < 137^\circ$ ) and again a  $1/\cos\theta$  dependence in the Backward Endcap region ( $\theta > 137^\circ$ ). For the MVD, the dip in the region of  $\theta$  close to  $20^\circ$  is due to the gap between the MVD disks in the forward and the Barrel MVD. The full coverage for the barrel starts only from about  $40^\circ$ . The radiation length in the backward region is very large for the MVD due to the services which are placed in this region.

In the following, we investigate the bremsstrahlung effect in the angular range of  $30^\circ < \theta < 120^\circ$  and  $10^\circ < \theta < 20^\circ$ .

### 5.1.1.3 Electron energy loss

The distribution of electron energy loss by bremsstrahlung is highly non-Gaussian. The bremsstrahlung effect depends on the energy  $E$  and mass  $m$  of the particle as  $(E/m)^4$ . In the PANDA energy range, only electrons are significantly affected by this process.

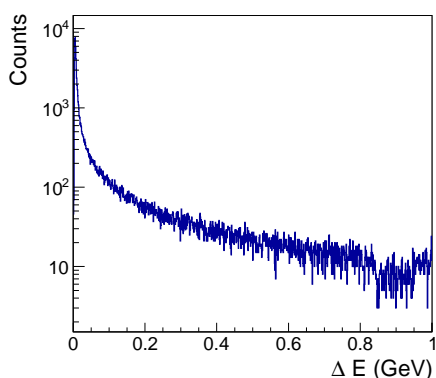


Figure 5.2: Energy loss distribution in bins of 1 MeV for  $10^4$  electrons ( $p_T=1$  GeV/c) in the Barrel detection region ( $30^\circ < \theta < 120^\circ$ ).

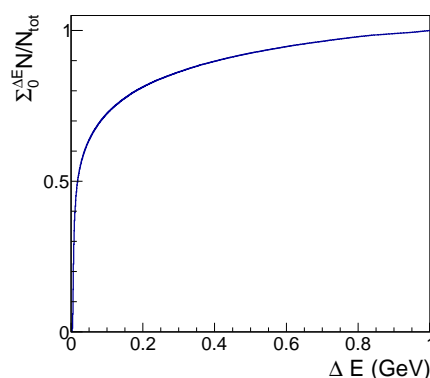


Figure 5.3: Proportion of electrons with energy loss lower than  $\Delta E$ , for an electron with  $p_T=1$  GeV/c in the Barrel detection region ( $30^\circ < \theta < 120^\circ$ ).

Figure 5.2 gives an example of the energy loss distribution for electrons with a transverse momentum of 1 GeV/c in the Barrel detection region. The slope of the distribution is very steep at low energies. However, it extends up to the kinematical limit with a slowly decaying tail. This typical trend is known as "bremsstrahlung tail", and affects the electron momentum resolution. The mean value of energy loss in the figure is about 112 MeV, as expected due to the thickness of the material in the Barrel region which is of the order of  $0.1X_0$ . In the bremsstrahlung process the mean energy loss is indeed roughly given by  $\Delta E \sim E \cdot (X/X_0)$ .

Figure 5.3 shows that about 73% of events lose less energy than the mean value. So, it is clear that a Gaussian fit can not well describe the energy loss distribution and taking the mean value would overestimate the energy loss for most of the events. This is the reason why bremsstrahlung can not be handled by track followers like GEANE which are based on mean values and Gaussian errors.

#### 5.1.1.4 Bremsstrahlung photon angular distributions

As shown in figure 5.4, the bremsstrahlung photons are emitted in a very narrow cone around the electron direction. 90% of the photons are emitted with an angle with respect to the electron, which is smaller than 2 mrad.

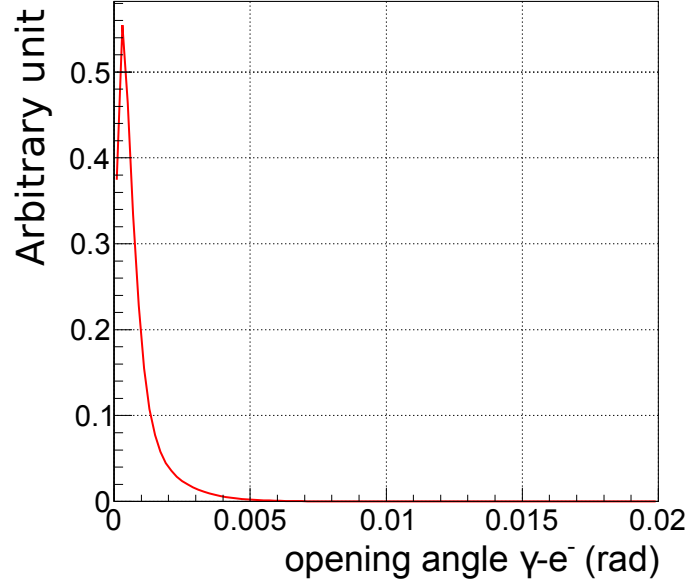


Figure 5.4: The distribution of the opening angle between the bremsstrahlung photon and its mother electron in GEANT for electrons at 1 GeV/c.

#### 5.1.1.5 Photon multiplicities

The multiplicity of photons emitted in the Barrel and Forward Endcap regions in central tracking system for electrons with different electron momenta has also been studied (on table 5.1). Depending on momentum, 50~70% of the electrons pass the detectors with emission of at least one photon with an energy higher than 1 MeV at 90°, whereas this fraction reaches 80% at 15°. This is due to the different numbers of radiation length at the given angles (see figure 5.1).

For higher momentum electrons, the probability of photon emission increases, since the cross section of photon emission depends on the energy of incident electron (most of the electrons emit one photon, but multiphoton emission is also important).

N. of $\gamma$	$\theta=90^\circ$		$\theta=15^\circ$	
	$p_T = 1 \text{ GeV}/c$	$p_T = 2 \text{ GeV}/c$	$p_T = 1 \text{ GeV}/c$	$p_T = 2 \text{ GeV}/c$
0	48.8%	38.7%	19.0%	18.9%
1	30.4%	37.3%	31.9%	33.9%
2	14.2%	16.0%	26.8%	26.9%
3 and more	6.6%	8.0%	22.3%	20.3%

Table 5.1: Proportion of the different photon multiplicities for different electron transverse momenta. The threshold on the photon energy is 1 MeV.

### 5.1.1.6 Photon emission point

The positions of photon emission in the radial direction for the Barrel region ( $30^\circ < \theta < 120^\circ$ ) and along the beam direction for the Forward Endcap region ( $10^\circ < \theta < 20^\circ$ ) are shown in figure 5.5 for electrons with  $p_T = 300$  MeV/c. The different subdetectors appear very clearly in the figure. For example, in the Barrel region, the structures in the region with distance from the beam axis lower than 15 cm are due to the MVD layers, while a small and continuous yield can be seen in the STT region ( $14 < R < 41$  cm). The two peaks in front ( $R = 14$  cm) of and at the end ( $R = 41$  cm) of STT are due to the support. There are four times more photons emitted in MVD than in STT. This is due to the ratio of number of radiation length which is about 4 in the Barrel region. In the Forward Endcap region, an additional sub-structure of three peaks which correspond to the GEM detectors is visible at the region of  $z$  larger than 110 cm. The increase of the number of emitted photons is mainly due to the fact that much more photons are emitted from the STT. The ratio of number of radiation length in STT and MVD is of the order of 2 in this region.

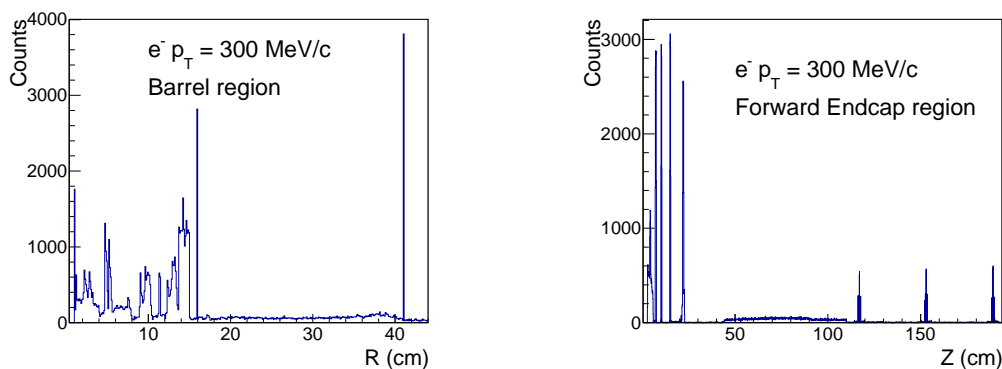


Figure 5.5: The spatial distribution of the bremsstrahlung photon emission point for electrons with  $p_T = 300$  MeV/c in the Barrel region (left) and in the Forward Endcap region (right).

## 5.1.2 Electron tracking resolution

Here, the effects of bremsstrahlung on momentum and angular resolution will be shown.

### 5.1.2.1 General results

As the muons have very little interaction with the material of detectors, they are taken as a reference for the resolution for electron momentum reconstruction. The general trends of muon momentum resolutions have been studied in section 4.2.4.1 (see figure 4.8 and figure 4.9). Here, we will compare electron and muon resolution.

Figures 5.6, 5.7 and 5.8 show examples of momentum and angular resolutions for electrons and muons with a transverse momentum of 1 GeV/c and 2 GeV/c in the Barrel detection region. The momentum resolution is defined as  $\Delta p/p = (p_{MC} - p_{KF})/p_{MC}$ , where  $p_{MC}$  is the Monte-Carlo value and  $p_{KF}$  is the reconstructed value as calculated using Kalman filter. The angular resolution is defined by the difference between the Monte-Carlo and the reconstructed values.

We see that the momentum resolution distribution of the electrons has a large tail and the center of the peak is also shifted to positive values (0.4%) compared to the distribution for muons. This can be qualitatively understood by the fact that photon emission decreases the

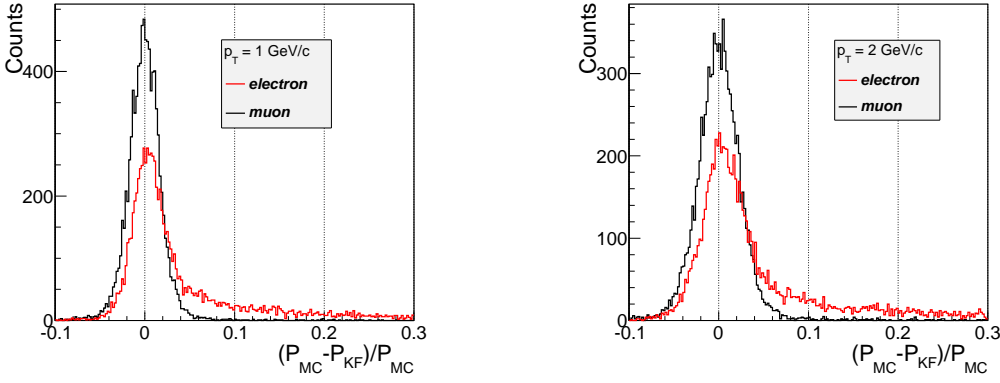


Figure 5.6: Comparison of electron (red) and muon (black) momentum resolution for  $p_T=1$  GeV/c (left) and  $p_T=2$  GeV/c (right) in Barrel region ( $30^\circ < \theta < 120^\circ$ ).  $P_{MC}$  is the Monte-Carlo momentum,  $P_{KF}$  is the momentum reconstruction with Kalman Filter.

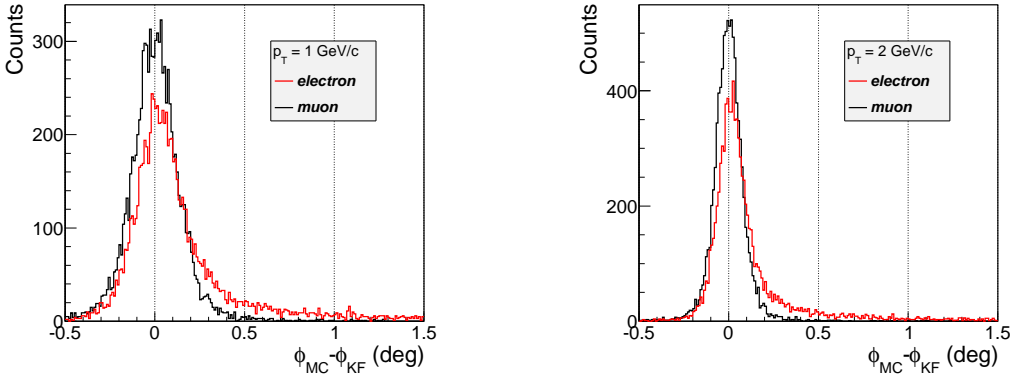


Figure 5.7: Comparison of electron (red) and muon (black)  $\phi$  angular resolution for  $p_T=1$  GeV/c (left) and  $p_T=2$  GeV/c (right) in Barrel region ( $30^\circ < \theta < 120^\circ$ ).  $\phi_{MC}$  is the Monte-Carlo angle,  $\phi_{KF}$  is the reconstructed angle.

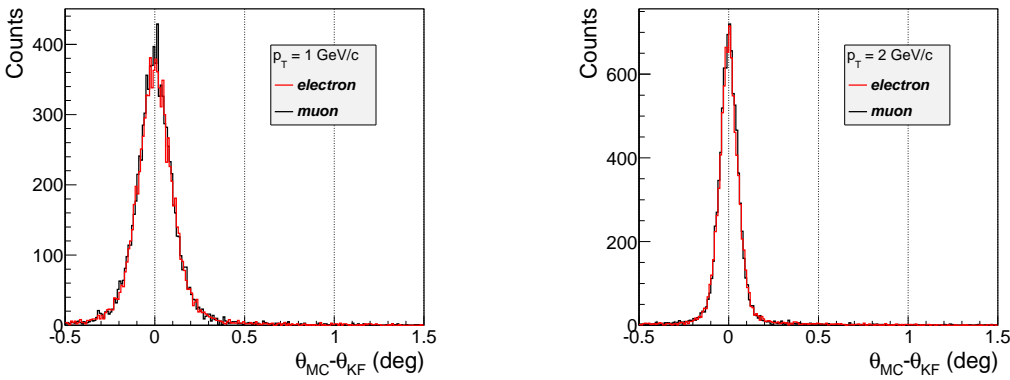


Figure 5.8: Comparison of electron (red) and muon (black)  $\theta$  angular resolution for  $p_T=1$  GeV/c (left) and  $p_T=2$  GeV/c (right) in Barrel region ( $30^\circ < \theta < 120^\circ$ ).  $\theta_{MC}$  is the Monte-Carlo angle,  $\theta_{KF}$  is the reconstructed angle.

momentum of the electron. The shape of the distribution with a large tail is reminiscent of the tail in the energy loss distribution in figure 5.2. The proportion of events inside two standard deviations of the Gaussian fit of the resolution spectra is only about 60% in the Barrel EMC detection region and 45% in the Forward Endcap EMC detection region (see more information in Table 5.2). As shown in figure 5.1, the larger effect in the forward region can be explained by the larger number of radiation lengths traversed. For muons, the proportion of events inside two standard deviations of the Gaussian fit is about 85% for all momenta in both Barrel and Forward Endcap regions (to be compared to 95% in the case of a perfect Gaussian). The distribution of electron azimuthal angular resolution also presents a tail, but this is less crucial for pionic background rejection than the momentum resolution. Indeed, channels with pions and kaons instead of electrons can not be distinguished by the  $\phi$  angle correlations at all. The polar angle distribution (Figure 5.8) shows a perfect agreement with the distribution for muons.

Barrel region			FW Endcap region		
$e^- p_T$ (GeV/c)	$\sigma$	$N_{2\sigma}/N$	$e^- p_T$ (GeV/c)	$\sigma$	$N_{2\sigma}/N$
0.5	1.5	55.6%	0.5	1.9	46.6%
1	1.8	58.9%	1	2.1	46.3%
2	2.4	61.0%	2	2.4	46.6%

Table 5.2: Proportion of events with momentum resolution inside  $2\sigma$  of a Gaussian fit for electron in the Barrel region (Left) and in the Forward Endcap region (Right).

This difference between electron and muon reconstruction can be explained by the bremsstrahlung photon emission in the tracking system. This is shown in figure 5.9, where electrons with momentum of 1 GeV/c are taken as an example and the MC information is used to get information about photon emission.

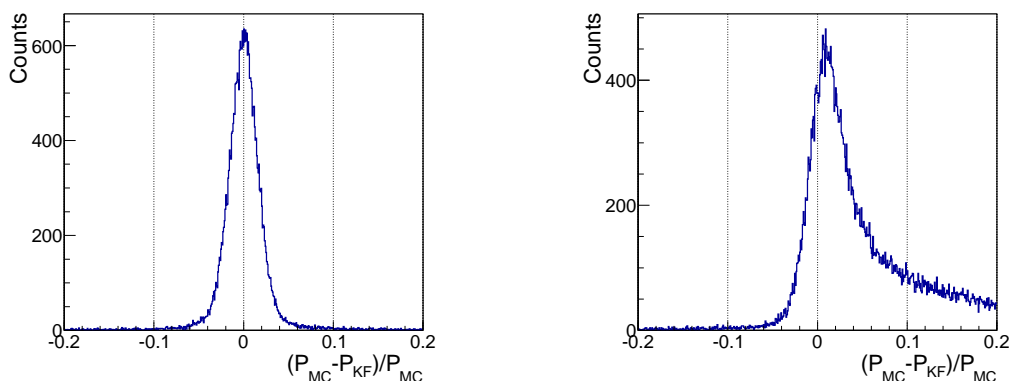


Figure 5.9: Momentum resolution of electrons with  $p=1$  GeV/c and  $\theta = 90^\circ$ . Left: No photon emitted with energy larger than 1 MeV. Right: at least one photon with energy larger than 1 MeV.

If there is no photon emitted with an energy larger than 1 MeV (figure 5.9, Left), the electron momentum resolution is as good as for the muon, for which the effect of bremsstrahlung is negligible. The shape is symmetric, the center is at zero and there is no tail. But when one or several photons are emitted (figure 5.9, Right), the distribution becomes highly asymmetric and the center of the peak shifts also towards positive values. This clearly illustrates that the problem of bad momentum resolution for electrons is due to the bremsstrahlung photon emission in the detectors.

### 5.1.2.2 The influence of bremsstrahlung emission point

The impact of the photon emission on the electron momentum reconstruction depends strongly whether the emission occurs at the beginning or at the end of the track. The more the points are measured after the photon emission the larger the effect will be.

Figure 5.10 gives an example of the different electron resolutions for the bremsstrahlung photons emitted at different position along the track.

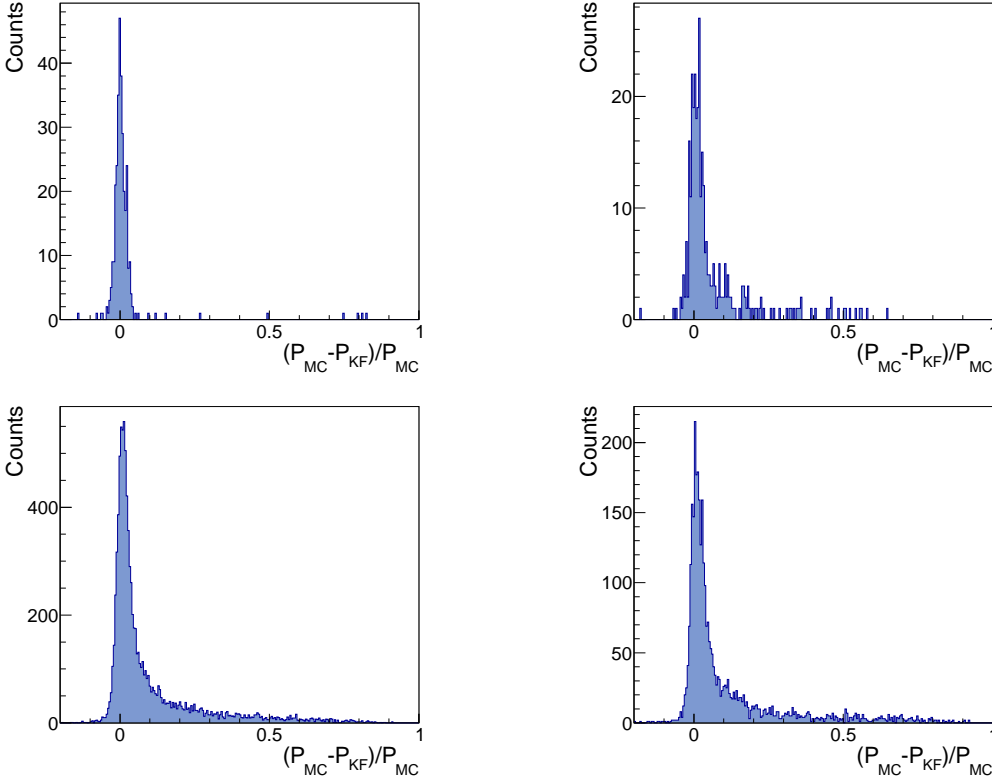


Figure 5.10: Momentum resolution of electrons with  $p=1$  GeV/c in the Barrel region with a bremsstrahlung photon emitted at different distances  $R$  from the beam axis. Top left: at  $R = 38$  cm (end of the STT). Top right: at  $R = 20$  cm (first several point of the STT). Bottom left: at  $R = 14$  cm (end of the MVD). Bottom right: at  $R = 3$  cm (first point of the MVD).

### 5.1.2.3 Comparison of reconstructed momentum and momentum after photon emission

As seen in figure 5.5, most of the bremsstrahlung photons are emitted in the MVD which has the largest material budget. As discussed in section 5.1.1.4, for an electron emitted at  $90^\circ$ , the average thickness of MVD is about  $0.07 X_0$ , about a factor of 4 more than for the STT. As a result, there are on average four to five times more photons emitted in the MVD than in the STT. In addition, the MVD provides only four to six points to the track, depending on the  $\theta$  and  $\phi$  angles, which is much less than the 25 points provided by the STT. These points are very close to the target (at a radial distance lower than 15 cm), while the STT points are distributed up to a radial distance of 42 cm. The momentum of the track is therefore mostly defined by the STT points, most of which are measured after the  $\gamma$  emission. Therefore, in most cases, the

Kalman Filter will give a reconstructed electron momentum ( $p_{KF}$ ) close to the momentum after the  $\gamma$  emission.

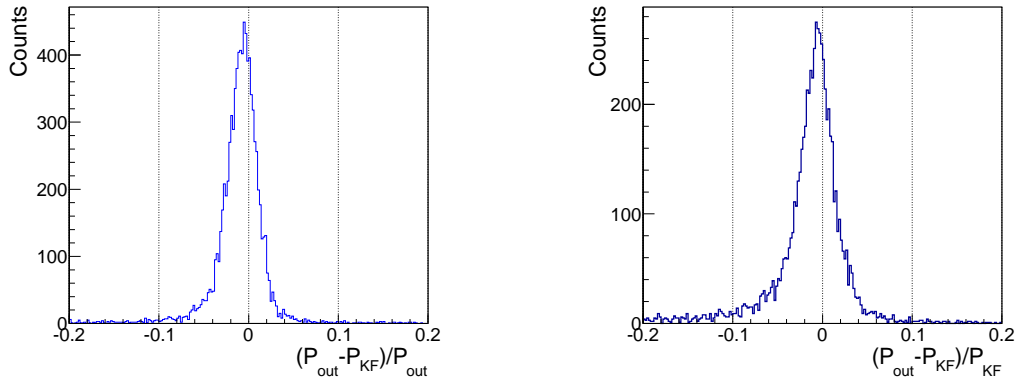


Figure 5.11: Comparison of  $p_{KF}$  and  $p_{out}$  (see text) for electron transverse momentum at 1 GeV/c in the Barrel detection region (left) and the forward endcap detection region (right).

In figure 5.11, the comparison of the reconstructed momentum with the momentum at the end of the tracking system from the Monte Carlo ( $p_{out}$ ) shows that the reconstructed electron momentum gives indeed a good approximation for the momentum after the  $\gamma$  emission. The observed shift is due to the energy loss by ionization which affects  $p_{out}$ , but is corrected in the Kalman Filter procedure. One can notice that the rms is only slightly larger than the value for the muon momentum resolution distribution (see section 4.2.4.1). The asymmetry on the left side is due to bremsstrahlung emission at the end of the track. In this case, the Kalman Filter provides a momentum  $p_{KF}$  close to  $p_{MC}$  (see figure 5.10) and only  $p_{out}$  is affected by the bremsstrahlung. This tail on the left side of the distribution is larger when the electron travels in the forward endcap region, as can be seen on figure 5.11 right. This can be explained by the fact that more photons are emitted in the STT, i.e. more points of the track are measured before photon emission. But, for most events  $p_{KF} \sim p_{out}$ .

### 5.1.3 The problem of bremsstrahlung treatment in the Kalman filter

The distribution of electron energy loss by bremsstrahlung is highly non-Gaussian. So the Kalman Filter approach with GENFIT, which uses the mean value of the energy loss distribution to calculate the next point and its root mean square (RMS) to estimate the error of the energy loss distribution, is not well suited. This is why bremsstrahlung cannot be successfully introduced in the Kalman Filter. A new method based on the photon detection in electromagnetic calorimeter is proposed.

## 5.2 Electron bremsstrahlung correction method

The problem of "bremsstrahlung tail" of electrons reduces the efficiency of signal selection of the  $e^+e^-$  channels. Methods like the Gaussian Sum Filter [83] or Dynamic Noise Adjustment (DNA) [84] are sometimes used to improve the electron momentum determination. These two methods can partially improve the momentum resolution, but have less effect to the bremsstrahlung tail. As explained further in more details, we follow a different procedure based on an event by event treatment and exploiting the detection of the bremsstrahlung photon.

### 5.2.1 General idea

A new attempt to handle the problem of bremsstrahlung by using the energy of photons measured in the EMC is proposed. In this method, for each event, a photon will be searched for in an angular window around the electron track. Its energy  $E_\gamma$  will be used to correct the momentum  $P_{KF}$ .

$$p_{rec} = p_{KF} + E_\gamma \quad (5.1)$$

This can be easily justified by the discussion in section 5.1.1.4 and 5.1.2.3.

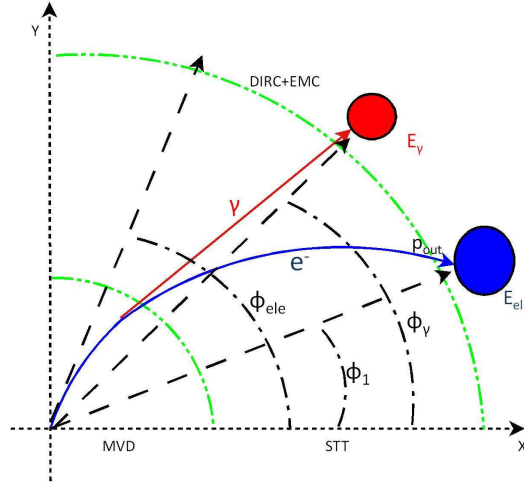


Figure 5.12: An example of electron track with a photon emission in the tracking system.

The bremsstrahlung photons are indeed emitted in a very narrow cone around the electron direction and the Kalman Filter gives a reconstructed electron momentum ( $p_{KF}$ ) close to the momentum after the  $\gamma$  emission ( $p_{out}$ ) (see section 5.1.2.3). One can deduce that

$$p_{KF} \sim p_{out} \sim p_{MC} - E_\gamma \quad (5.2)$$

Following these evidences, an improvement of the reconstructed momentum of electron is expected by adding the bremsstrahlung photon energy to the reconstructed momentum provided by the Kalman Filter.

### 5.2.2 Description of the method

The existing reconstruction algorithm identifies "bumps" in the distribution of energy deposits in the EMC crystals which correspond to a set of neighboring hit crystals. Neutral bumps are identified as those bumps which do not match with a track.

Two cases can be considered when searching for the bremsstrahlung photon (see figure 5.13). The first one corresponds to low energy electrons (transverse momentum  $p_T$  below 1 GeV/c) with large curvature. If the photon is emitted at the beginning of the track, the "bumps" of electron and photon in EMC are separated. In the second case, the curvature of the electron track is not large enough, the photon bump is merged in the electron bump and the existing software can not distinguish between the two signals. For these two cases, different methods to calculate the photon energy are used, as will be discussed later.

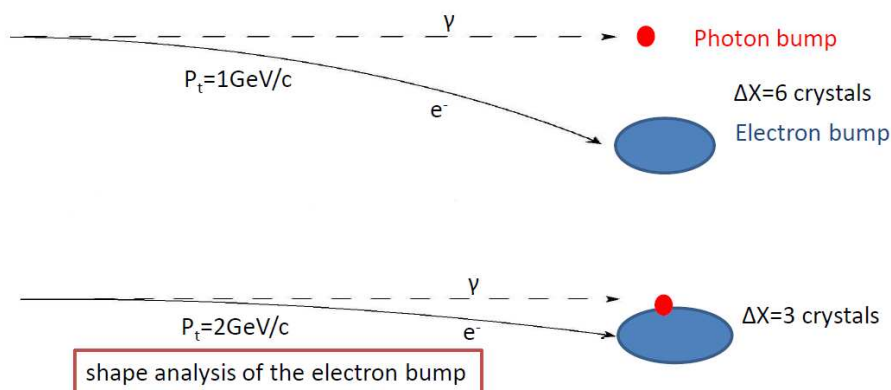


Figure 5.13: The two different cases for the bremsstrahlung photon detection.

The threshold of photon energy is set to 1% of the momenta of mother electron. The emission of photons with a lower energy does not indeed affect the electron momentum resolution. It means that only photons with energy larger than the threshold will be accepted as bremsstrahlung photons and will be used to correct the electron momenta.

In the following, each step of the method will be described in detail.

### 5.2.2.1 First step: separated photon and electron Bumps

In a first step, bremsstrahlung photons detected as separated photons bumps are searched for.

As the bremsstrahlung photons are emitted in a very narrow cone around the electron direction, the photon angular information is very useful to identify the primary bremsstrahlung photons. Since the magnetic field is parallel to the beam axis, only the azimuthal angle of the momentum vector of the electron is changing along the track. The photon bump has therefore to be found with a polar angle  $\theta_\gamma$  close to the reconstructed electron one  $\theta_{ele}$ . The azimuthal angle  $\phi_\gamma$  of the photon bump, is expected to be between the reconstructed electron value  $\phi_{ele}$  and the value at the exit of the tracking system  $\phi_1$  (see figure 5.12).

The window in the polar angle to search for the photon is fixed to  $\pm 1^\circ$ . The limits in the azimuthal angle are calculated in two different ways for the Barrel region (equation 5.3, where  $R_{STT+MVD} = 42$  cm) and the Forward Endcap region (equation 5.4, where  $Z_{STT+MVD+GEM} = 192$  cm) due to their different geometries.

$$\phi_\gamma - \phi_{ele} < \phi_1 - \phi_{ele} = 2 \arcsin\left(\frac{0.3 \cdot B \cdot R_{STT+MVD}}{2 \cdot p_T}\right) \quad (5.3)$$

$$\phi_\gamma - \phi_{ele} < \phi_1 - \phi_{ele} = \frac{0.3 \cdot B \cdot Z_{STT+MVD+GEM} \cdot \tan(\theta_{ele})}{p_T} \quad (5.4)$$

Figure 5.14 shows an example for  $10^5$  electrons with  $p_T=1$  GeV/c in the Barrel region ( $30^\circ < \theta < 120^\circ$ ), the chosen limits for these angles are indicated as a rectangle.

This rectangular cut in the  $(\phi_\gamma - \phi_{ele}, \theta_\gamma - \theta_{ele})$  plane is used to eliminate the photons from the DIRC and EMC detectors and select most of the photons emitted in the tracking system. As shown in the figure 5.14 left, most of the events with a  $\gamma$  emitted in the tracking system are indeed inside the  $\phi_1 - \phi_{ele}$  limit. When the  $\gamma$  is emitted in the DIRC (figure 5.14 right), the distribution is much broader. The dip seen around  $\Delta\phi = 10^\circ$  in the right figure is due to the photons produced in the DIRC which are merged into the electron bumps. The

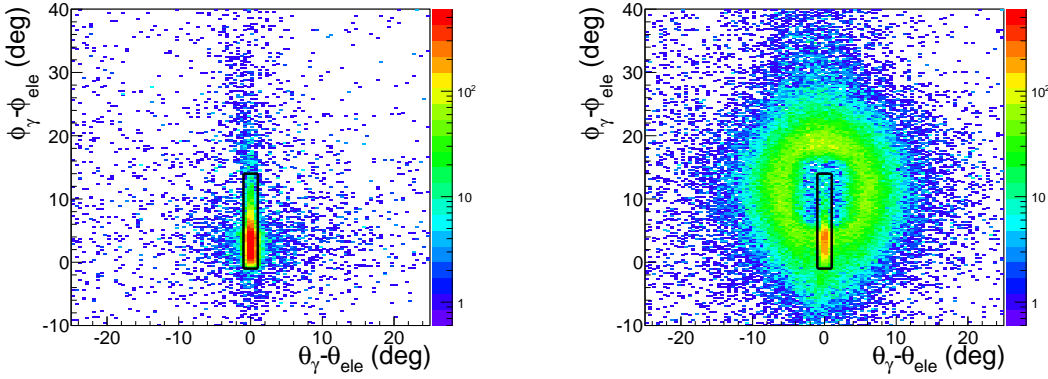


Figure 5.14: Correlation between the difference in azimuthal and polar angles of the  $\gamma$  and electron bumps. The figure on the left shows photons from the central tracking system (before the DIRC), and the one on the right is for photons produced outside this region. The electron has  $p_T = 1$  GeV/ $c$  and is in the Barrel Region ( $30^\circ < \theta < 120^\circ$ ). The rectangle shows the limits for the selection of bremsstrahlung photon.

photons seen around the dip correspond to the secondary photons produced in DIRC or EMC by the interaction of the primary electron in the DIRC or EMC. They are not taken into account in the correction method, which is relevant since those interactions do not affect the momentum resolution. The red spot around  $\Delta\phi = \phi_\gamma - \phi_{ele} = 0^\circ$  corresponds to the secondary photons induced by the bremsstrahlung photons emitted in the central tracking system. As they carry a fraction of the primary photon energies, these secondary photons are also useful for the correction. Most of the secondary photons produced by the interaction in DIRC remaining in the rectangular cut will anyway be eliminated by the energy threshold, since most of them have very low energies.

After selection by the angular cut and the energy threshold, the energy of photons are added to the reconstructed electron momentum.

### 5.2.2.2 Second step: merged photon and electron Bumps

To take into account the case of  $\gamma$  merged into the electron bump, a second algorithm based on the azimuthal distribution of the energy deposited in the EMC crystals in the electron bumps was developed. The idea is that, due to the deviation of the electron in the magnetic field, the photon is expected to contribute only on a given side of the electron bump in the transverse plane, depending on the sign of the curvature.

For each cluster corresponding to an electron, the energy deposits in each crystal as a function of the azimuthal angle  $\phi$  are considered. An histogram is built from the energy deposits in crystals in a given azimuthal bin. The bin width is taken as  $2.25^\circ$ , which corresponds to the angular aperture of the entrance face of the crystals in Barrel (see figure 5.15), so that for the barrel region, one bin corresponds to one row of crystals. An example of such histogram for a negative electron is shown in figure 5.16. Two local maxima can be recognized in the energy distribution. The smaller one on the left part is due to a bremsstrahlung photon and its energy can be extracted and added to the electron reconstructed momentum. To estimate the energy of the photon, the following algorithm is used.

First, it is determined which hits correspond to the electron and which to the photon. Each bin with a signal is taken to make a list  $k_1, k_2, \dots, k_n$  of the amplitude of energy deposits. The

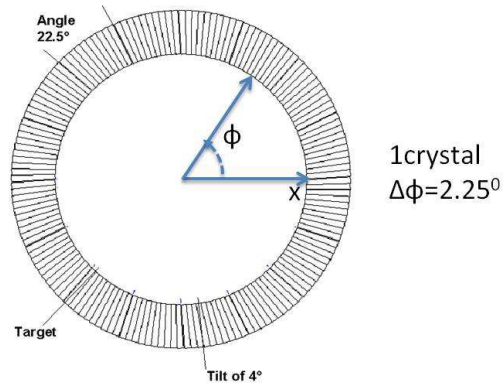


Figure 5.15: The geometry of the Barrel EMC in the transverse plane and the definition of " $\phi$ " angle.

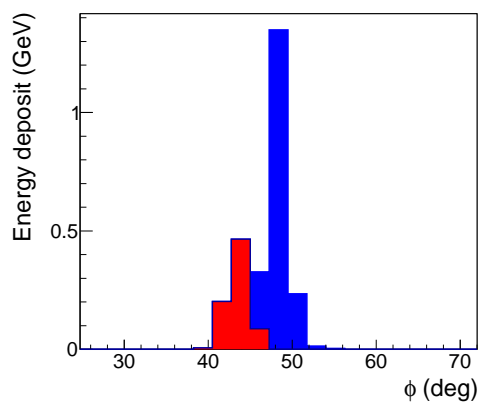


Figure 5.16: An example of the distribution of energy deposits in the EMC as a function of  $\phi$  in the case of a bump resulting from merged electron (blue) and bremsstrahlung photon (red) showers.

values in the list are grouped by three ( $k_{i-1}, k_i, k_{i+1}$ ), and each group is given a code according to its configuration as shown in Table 5.3.

slope code	configuration
1	raise
-1	fall
0	peak
2	valley

Table 5.3: The different configurations for three neighboring bins of the histogram.

For example, for the 8 groups in figure 5.16, the codes are (1, 1, 0, 2, 0, -1, -1, -1) which means that there are two peaks and one valley in this electron bump. This procedure allows to detect substructures in the bumps, which we call " $\phi$ -bumps". The energy of each " $\phi$ -bump" is calculated as the sum of the energy deposits on either side of the valley. The intermediate bin in the two  $\phi$  bumps is distributed with a weight proportional to their respective peak values. After that, a list of the " $\phi$ -bumps" ( $E_1, E_2, \dots, E_n$ ) is made. Due to the magnetic field which deviates the negative electron, the peak on the right hand side is considered to be the electron peak, and the others are assumed to be photons. For a positron, it is the opposite, the peak on the left is taken as the positron peak. As a consequence, the energy of photons is calculated as  $\Sigma_1^{n-1} E_i$ .

### 5.2.3 Implementation of the method in PANDARoot

The bremsstrahlung correction method described above was implemented within the PANDARoot framework through the addition of three new classes, and modification of an existing class. The locations of these classes are given below with a brief description of their functions and instruction of how to invoke them in a simulation/reconstruction macro.

- **PndEmcPhiBumpSplitter (new class emc/EmcReco )** This class implements the analysis of the  $\phi$  projection of clusters to determine if the cluster comes from two or more showers generated by different particles (for example, of interest to this method: an electron and its associated bremsstrahlung photons). If this is found to be the case, the energy of the cluster is split into multiple components called " $\phi$ -bump". Since the EmcBump container can store all the information about phi-bumps that is required for later analysis (their energy), the phi-bumps derived from each cluster are stored inside a TClonesArray of EmcBumps with the name "EmcPhiBumps". An integer is stored that indicates which cluster id each phi-bump was derived from.
- **PndEmcMakeBump (existing class in emc/EmcReco)** was modified to instantiate a PndEmcPhiBumpSplitter object and execute the main process after the regular bump splitting (PndEmc2DLocMaxFinder and PndEmcPhiBumpSplitter) algorithms.
- **PndPidBremCorrector (new class in pid/PidCorr).** In this class the phi-bumps created in the PndEmcPhiBumpSplitter class, in addition to all neutral candidate cluster energies, are analyzed track by track of charged candidates. The cumulative energy of

– All phi-bumps derived from the charged candidate's EMC cluster

- Those neutral candidates within spatial proximity of the track candidate projection (as determined by momentum and charge dependent  $\Delta\phi$  vs  $\Delta\theta$  cut described in previous sections)

is added to momentum of charged candidate track. The momenta are calculated from energy using electron mass hypothesis.

- **PndPidBremCorrected4Mom (new class in pnddata/PidData).** In order to avoid conflict with analysis that are not necessarily interested in bremsstrahlung correction, a separate container class is created to store the corrected momentum associated with each candidate charged track. This class stores the new calculated momentum, as well as the index of the charged candidate track for which it gives the corrected momentum.

To execute this correction algorithm, the only thing that is required is to add the PndPidBremCorrector task in the PID stage of the simulation, after PndPidCorrelator (the code is given below). For analysis, it will be necessary, for each track, to loop over the list of all PndPidBremCorrected4Mom of the event until the correct one is found. The CPU time overhead due to this method was estimated to be 10% for phi-bump splitting and 5% for calculating the bremsstrahlung corrected momentum.

## 5.3 Result of the correction method

In the following, the efficiency of bremsstrahlung photons reconstruction and the improvement of the electron momentum reconstruction will be shown. As the geometry of EMC is not the same for the Barrel and the Forward Endcap, this method is tested separately for these two regions. To do this,  $10^5$  electron samples were generated with five different momentum (0.5, 1, 1.5, 2, 2.5 GeV/c) with uniform polar angle distribution in two regions:  $[10^\circ, 20^\circ]$  and  $[30^\circ, 120^\circ]$  respectively.

### 5.3.1 Electron momentum resolution after using the correction method

The kinematical ranges of interest to test the method will be firstly determined. The momentum of anti-proton beam ranges from 1.5 to 15 GeV/c. The highest momenta of electrons are reached for the binary reaction  $\bar{p}p \rightarrow e^+e^-$ . Figure 5.17 shows the variation of  $p_T$  as a function of  $\theta$  for this reaction at different incident anti-proton momenta. One can conclude that the maximum transverse momentum in both the Forward Endcap ( $\theta < 22^\circ$ ) and the Barrel region is close to 2.7 GeV/c.

Since both the momentum resolution and the bremsstrahlung effect depend on the polar angle, different regions were considered taking into account the kinematics (see table 5.4).

Figures 5.18 to 5.21 show the new electron momentum resolution after correction for transverse momenta  $p_T$  from 0.5 GeV/c to 2.5 GeV/c. The result obtained when only the separated  $\gamma$  and electron bumps are used is also displayed as a green line in the figures. As expected, for  $p_T = 0.5$  GeV/c, the algorithm finds mostly separated  $\gamma$  and electron bumps. After applying the correction method, no significant change of the  $\sigma$  of a Gaussian fit is observed. However, the bremsstrahlung correction reduces significantly the tail of the resolution distribution. The improvement is especially remarkable for the most forward bin ( $[30^\circ, 45^\circ]$ ) where the material budget encountered by the electron is large. For  $p_T = 1$  GeV/c, the same trend is observed. In addition, the algorithm finds sometimes merged bumps depending on the photon emission point.

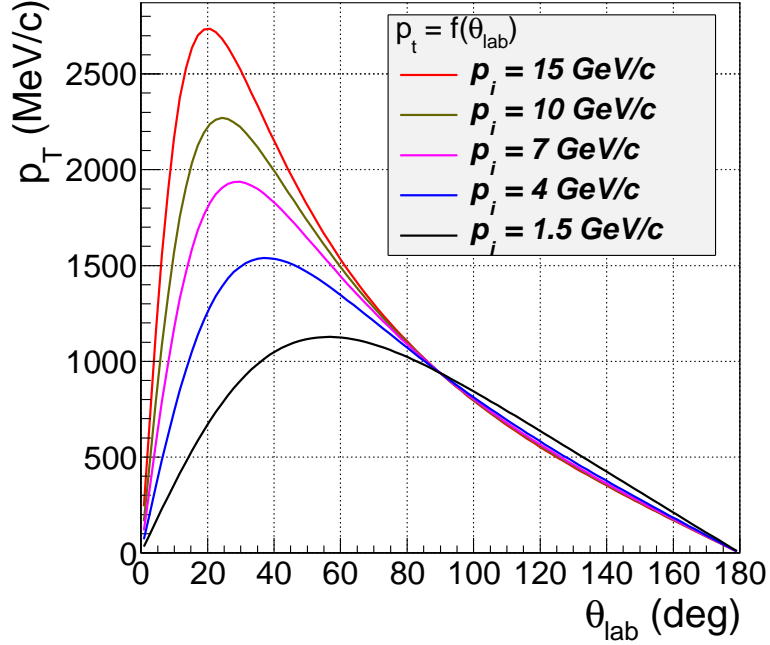


Figure 5.17: Kinematical curves showing the transverse momentum  $p_T$  against the laboratory polar angle  $\theta_{lab}$  for  $\bar{p}p \rightarrow e^+e^-$  reaction at five different anti-proton incident momenta.

Region	$e^- p_T$ (GeV)	$\theta$ angular region
Barrel	0.5	$[30^\circ, 45^\circ]$ , $[45^\circ, 60^\circ]$ , $[60^\circ, 75^\circ]$ , $[75^\circ, 90^\circ]$ , $[90^\circ, 105^\circ]$ , $[105^\circ, 120^\circ]$
	1	$[30^\circ, 45^\circ]$ , $[45^\circ, 60^\circ]$ , $[60^\circ, 75^\circ]$ , $[75^\circ, 90^\circ]$
	1.5	$[30^\circ, 45^\circ]$ , $[45^\circ, 60^\circ]$
	2	$[30^\circ, 45^\circ]$
Forward Endcap	0.5	$[10^\circ, 20^\circ]$
	1	$[10^\circ, 20^\circ]$
	1.5	$[10^\circ, 20^\circ]$
	2	$[10^\circ, 20^\circ]$
	2.5	$[10^\circ, 20^\circ]$

Table 5.4: Different kinematical regions used to test the method.

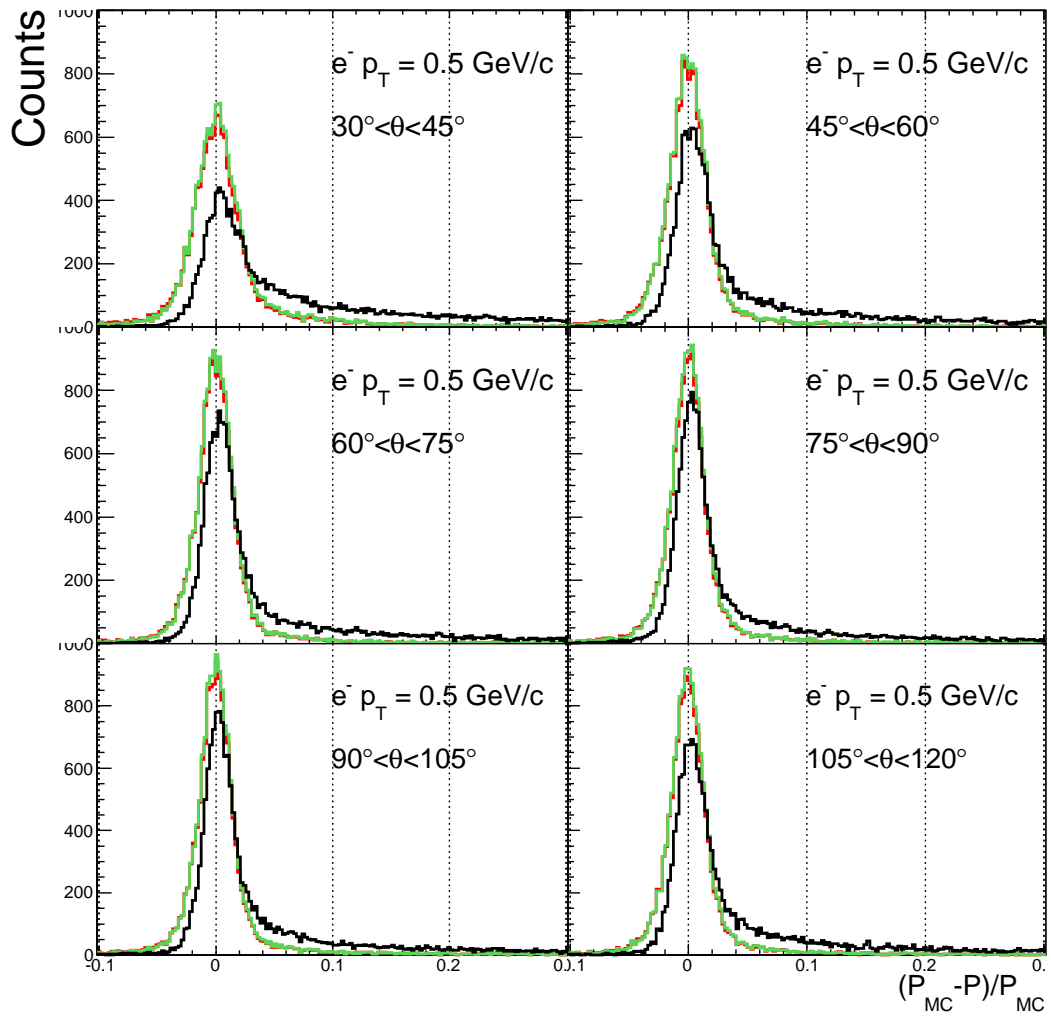


Figure 5.18: Comparison of the electron momentum resolution before (black) and after (red) using the bremsstrahlung correction method for electron with  $p_T = 0.5$  GeV/c in the Barrel region. The green line shows the result when only the separated  $\gamma$  bumps are used.

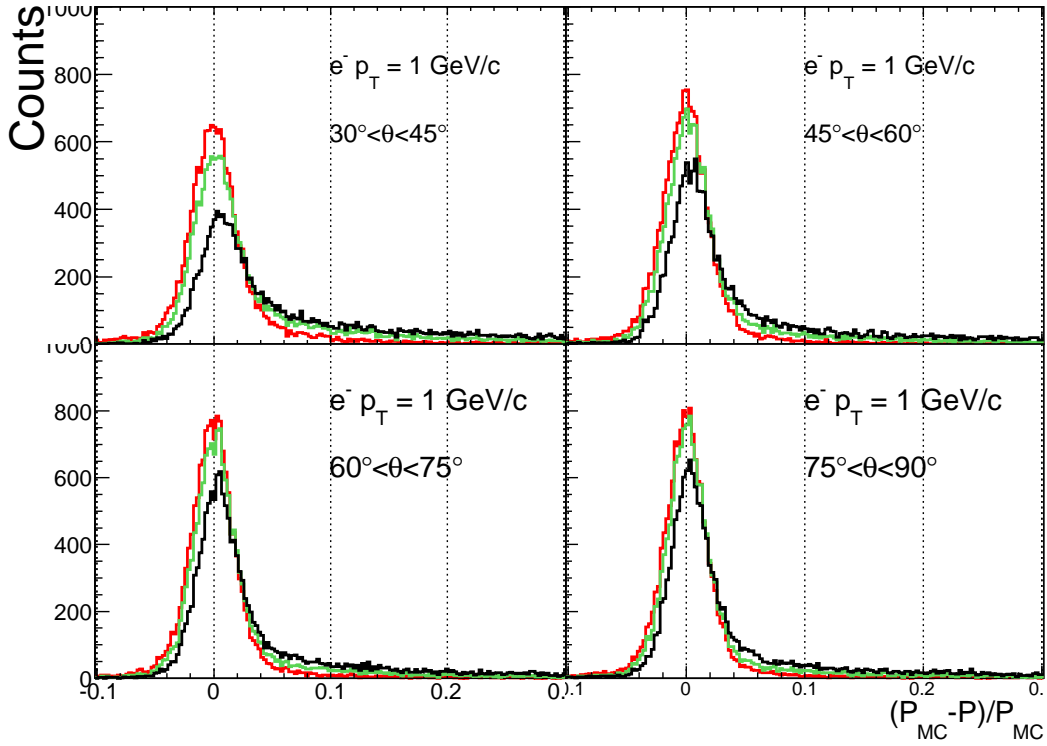


Figure 5.19: Same as figure 5.18 for  $p_T = 1 \text{ GeV}/c$ .

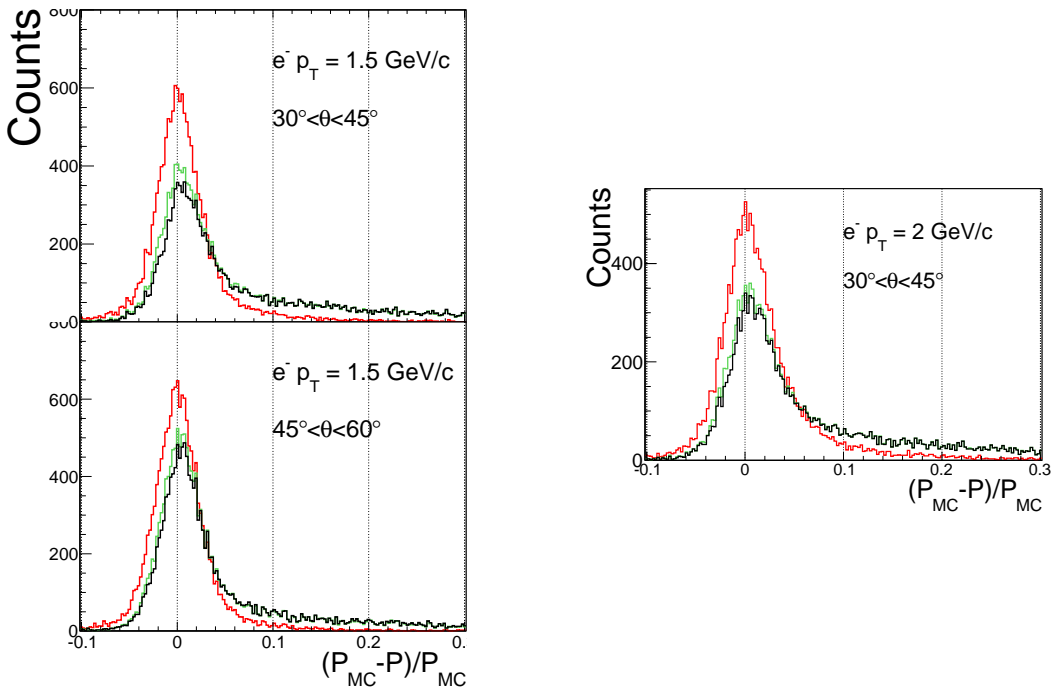


Figure 5.20: Same as figure 5.18 for  $p_T = 1.5 \text{ GeV}/c$  (Left) and  $p_T = 2 \text{ GeV}/c$  (Right).

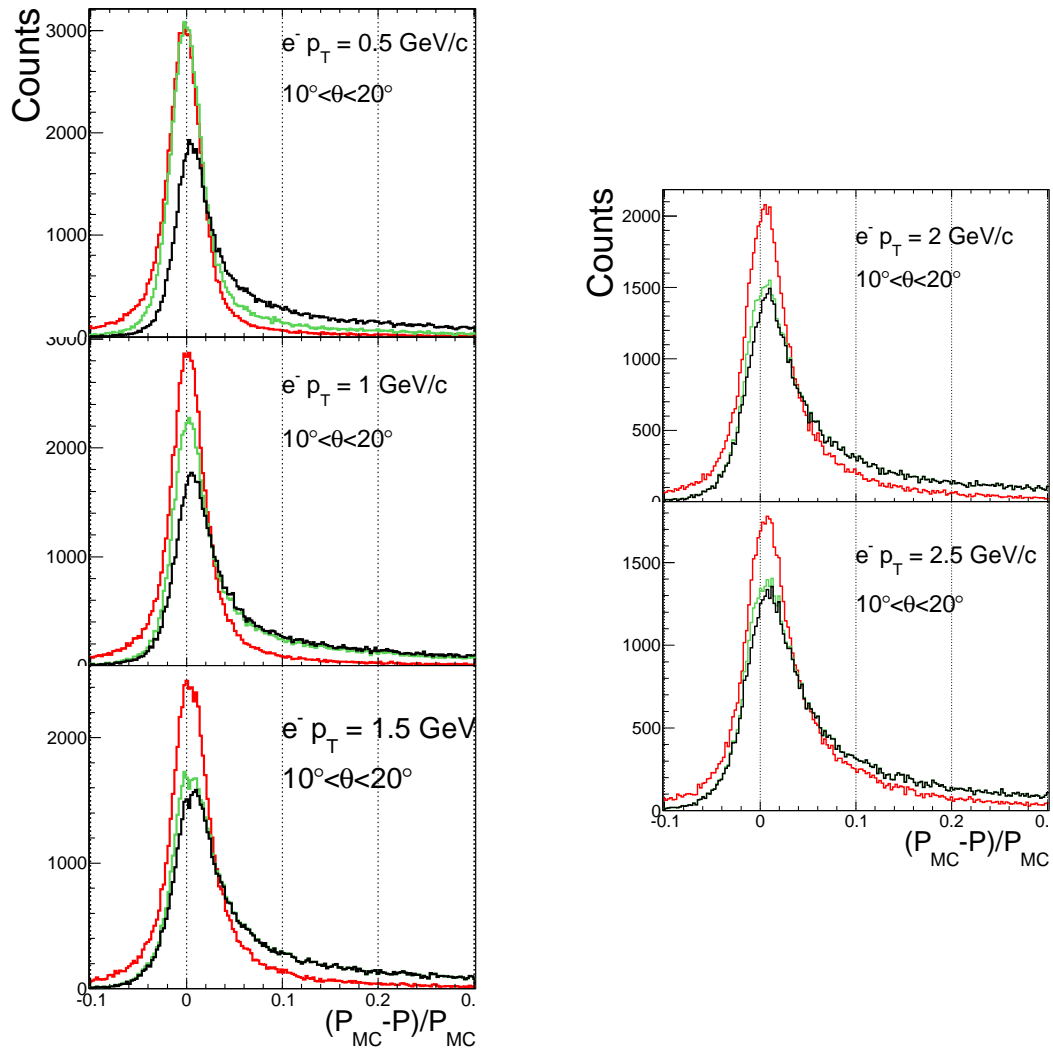


Figure 5.21: Comparison of the electron momentum resolution before (black) and after (red) using the bremsstrahlung correction method for the Forward Endcap region. The green line shows the result when only the separated  $\gamma$  bumps are used.

At 1.5 and 2 GeV/c, only merged bremsstrahlung photons are found. So, it can be noticed that the analysis of the shapes for merged bumps is important, crucially for  $p_T > 1$  GeV/c.

The improvement of the resolution in the Forward Endcap region is smaller than in the Barrel region and a tail is still present after applying the method. In addition, the width on the left hand side is slightly increased. This is due to the fact that more photons are emitted in the STT. As discussed in section 5.2, the validity of the method is based on the fact that photon emission occurs at the beginning of the track and adding the energy of a photon emitted at the end of the track leads to an overcorrection of the electron momentum. However, even in the Forward Endcap region, the improvement is significant.

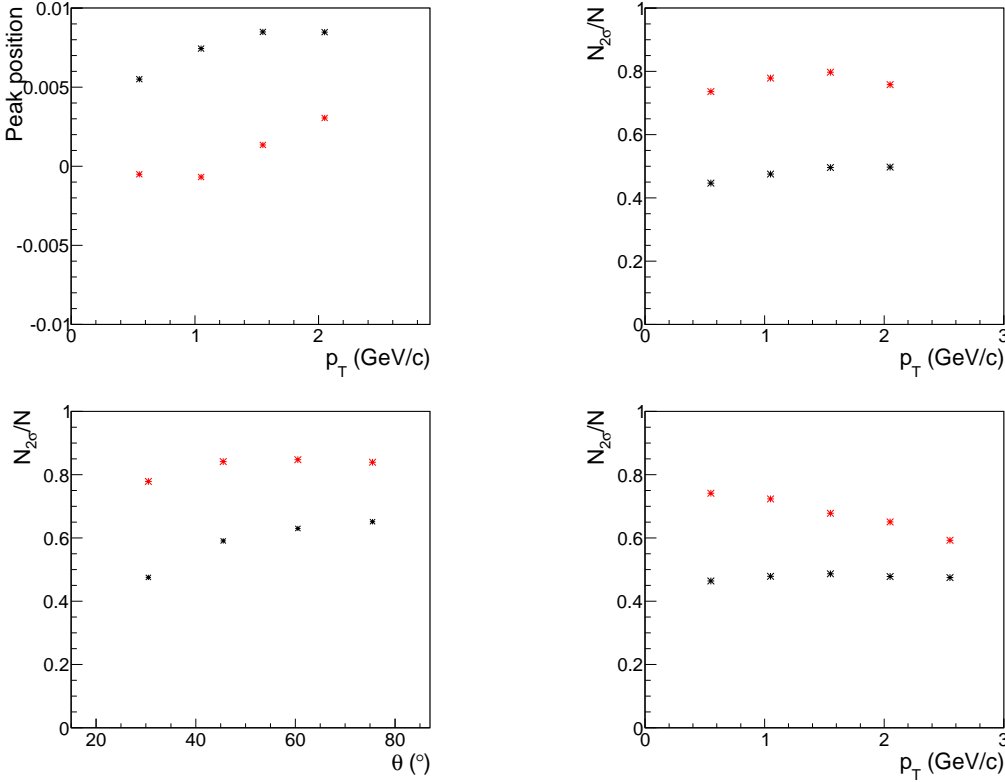


Figure 5.22: Improvement of the electron momentum reconstruction with the correction method in comparison to the reconstruction with Kalman Filter. Top left: position of the peak ( $\mu$ ) versus transverse momentum for electrons emitted at  $30^\circ$  to  $45^\circ$ . Top right: proportion of event inside  $2\sigma$  of a Gaussian fit versus transverse momentum for electrons emitted between  $30^\circ$  and  $45^\circ$ . Bottom left: proportion of events inside  $2\sigma$  of a Gaussian fit ( $N_{2\sigma}$ ) versus polar angle for electrons at 1 GeV/c. Bottom right: proportion of events inside  $2\sigma$  of a Gaussian fit versus transverse momentum for electrons emitted between  $10^\circ$  and  $20^\circ$ . The error bars on the extracted  $\mu$  and  $N_{2\sigma}$  are smaller than the size of the markers.

The improvement of the resolution introduced by the new method is quantified by studying the mean position and the number of events inside  $2\sigma$  of a Gaussian fit, as displayed in fig. 5.22.

### 5.3.2 Efficiency and purity of the bremsstrahlung photon reconstruction

The photon reconstruction efficiency of the method can be seen in table 5.5. The efficiency is defined as  $\epsilon = N_\gamma^{found}/N_\gamma^{MC}$  and the purity is defined as  $N_\gamma^{true}/N_\gamma^{found}$ , where  $N_\gamma^{MC}$  is

the number of photons emitted by electrons in the tracking system generated by Monte-Carlo,  $N_{\gamma}^{found}$  is the number of corresponding photons found by the correction method and  $N_{\gamma}^{true}$  is the number of true bremsstrahlung photons emitted in the tracking system and found by the correction method. A threshold is set on the photon energy at 1% of the total electron energy. Events with photons with an energy lower than this threshold are not considered for the efficiency and purity calculation.

Region	$e^{-} p_T$ (GeV/c)	$\epsilon$ (%)	Purity (%)
Barrel	0.5	79	94
	1	78	97
	2	46	98
	2.5	34	98
FW Endcap	1	63	96
	2	41	95

Table 5.5: Efficiency and purity to find a bremsstrahlung photon emitted before the DIRC with energy larger than 1% of the electron momenta.

From table 5.5, it can be seen that the method has a better efficiency ( $\epsilon$ ) in the low transverse momentum region where the electron and photon bumps are separated. However the efficiency is still significant at large  $p_T$ . The different efficiency observed in the Barrel and Forward Endcap regions is due to the different geometries. Firstly, the radius of the photon emission point in the Forward Endcap region is in average smaller than in Barrel region due to the different MVD geometry. This favors a larger separation in  $\phi$  between the photon and the electron. Secondly, the total track length in the transverse plane is smaller, which goes in the opposite direction. Finally, the global material budget is larger in the Forward Endcap region. Therefore, photons with larger energy (i.e. easier to reconstruct in the case of  $\phi$  bumps) are emitted. The method has a good purity: only a few percent of the reconstructed photons are not true Bremsstrahlung photons.

The distributions of the sum of the energies of all photons found by the correction method are also studied in figure 5.23 and compared to the distribution deduced from the Monte-Carlo. For the low  $p_T$  electrons, the efficiency of this correction method is good for all photon energies and for the two regions. This is because in this case, the photon and electron produce two separate bumps. When  $p_T$  is not sufficient to have separate bumps, the efficiency drops for low energy photons, due to the difficulty to distinguish them as a  $\phi$  bump. The average efficiency for photons of energy larger than 50 MeV, which affect the most the momentum resolution, is of the order of 50%.

The small peak observed in the Barrel region at  $\Sigma E_{\gamma} \sim p_T$  corresponds to electrons emitted close to  $90^{\circ}$  and hitting the target tube after a path in the tracking system long enough to reconstruct a track. Due to the large material thickness traversed by the electrons in this case, an electromagnetic shower can be produced and the electron loses in this case almost all its energy. These events are rejected in the  $\phi$ -bump search step, since in this case, there is most of the time only one single bump associated with this electromagnetic shower.

### 5.3.3 Limitations of the method

Several points need to be addressed concerning the limitations and the assumptions used by this correction method.

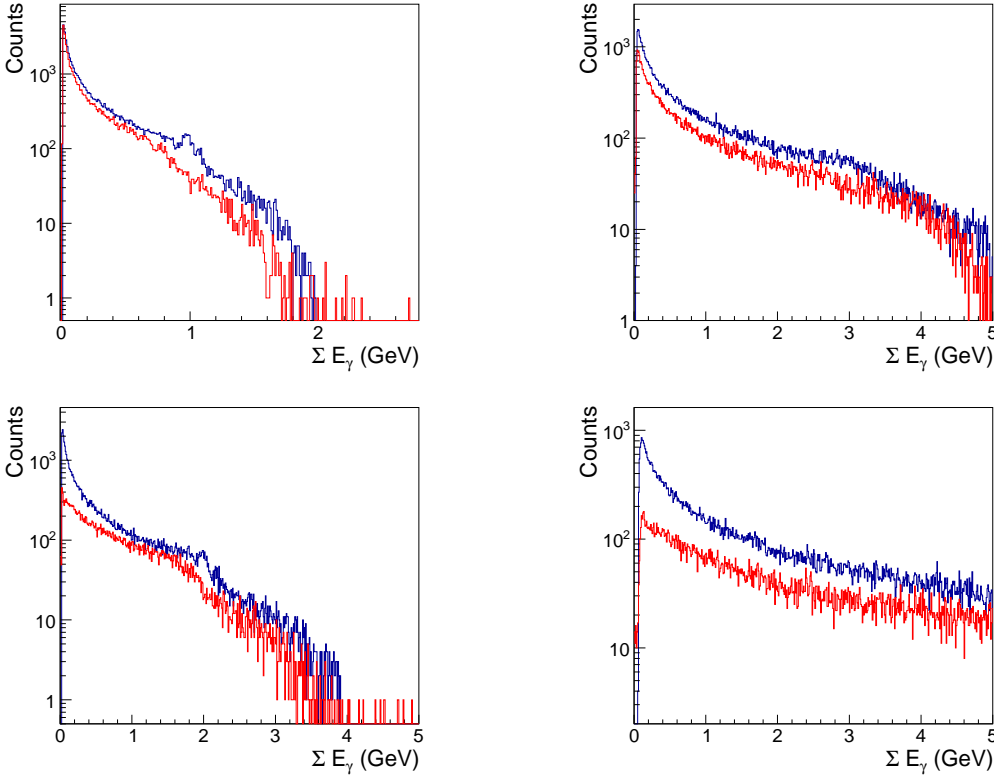


Figure 5.23: Distribution of the sum of the energies of bremsstrahlung photons emitted before the DIRC in one event for all reconstructed electrons (Blue) and for electrons associated with at least one photon found by the correction method (Red). Top left: Electron  $p_T = 1$  GeV/c in the Barrel region. Top right: Electron  $p_T = 1$  GeV/c in the Forward Endcap region. Bottom left: Electron  $p_T = 2$  GeV/c in the Barrel region. Bottom right: Electron  $p_T = 2$  GeV/c in the Forward Endcap region.

First of all, in the separated bremsstrahlung photon reconstruction, the threshold in  $\phi$  angle is potentially too loose. In the case of photon emission towards the end of the electron trajectory inside the tracking system or afterward, Kalman Filter can handle already the problem correctly. In case such photons pass the  $\phi$  angle cut, there is a risk of over-correction with the current threshold (equation 5.3 and equation 5.4).

Secondly, for the merged photon reconstruction, there also may be a need for an angular cut to limit the inclusion of secondaries from DIRC and EMC.

Thirdly, the result from the test with low energy electrons, for example, figure 5.18, shows that no improvement is observed when both the separated and merged photons are accounted with respect to the result obtained by using only the correction from the separated photons. So, perhaps a threshold energy on the electron needs to be included to obtain an optimal cut for when the merged photon reconstruction needs to be considered.

Last, the result from the test in Forward Endcap region (figure 5.21) show that in this region the method with the merged photon reconstruction introduces a tail on the left side of momentum resolution distribution. This most likely means that there is an over correction. This occurs when the photon is emitted in the middle or the end of the track, which is more frequent in the case of Forward Endcap region than in the case of the Barrel region.

These points should be the main focus of future work to improve the method.

## 5.4 Applications of the new method for different electromagnetic channels

For the proton structure studies, an important issue is the rejection of the hadronic background. Both Particle Identification (PID) and kinematical cuts are used. The latter are very sensitive to the electron momentum resolution. A larger efficiency for the kinematical cuts can be achieved by using the bremsstrahlung correction method.

The proton time-like form factor measurement in the  $\bar{p}p \rightarrow e^+e^-$  reaction with an anti-proton beam momentum of 3.3 GeV/c, is taken as an example to show the advantage of the method.

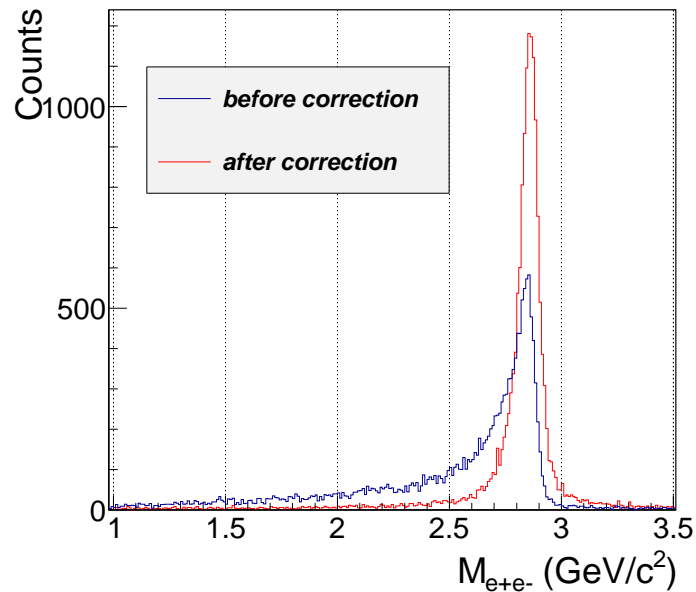


Figure 5.24: Distribution of the  $e^+e^-$  invariant mass before (blue) and after (red) using the bremsstrahlung correction method for the  $\bar{p}p \rightarrow e^+e^-$  reaction at  $\sqrt{s} = 2.865$  GeV

Figure 5.24 shows the  $e^+e^-$  invariant mass distribution after simulation and reconstruction with PANDARoot. For the  $\bar{p}p \rightarrow e^+e^-$  reaction, a selection of  $e^+e^-$  invariant mass larger than  $2.72 \text{ GeV}/c^2$  (corresponding to  $\sqrt{s} - m_{\pi^0}$ ) will be applied to suppress the background from the  $\bar{p}p \rightarrow e^+e^-\pi^0$  reaction, in addition to PID cuts. The efficiency of this cut on the signal ( $\bar{p}p \rightarrow e^+e^-$ ) selection is increased by a factor 1.7 when using the new method.

This method is also useful for other electromagnetic channels like the Transition Distribution Amplitude measurement in the  $\bar{p}p \rightarrow J/\Psi\pi^0$  reaction. The result will be given in the next chapter.

## 5.5 Conclusion

In this chapter, I have studied in detail the bremsstrahlung process for electrons and have shown the impact on the electron momentum reconstruction.

I presented a method to correct this effect, using the energy deposit of the bremsstrahlung photon in the EMC. I have shown the quantitative improvement provided by this method for signal reconstruction in the  $\bar{p}p \rightarrow e^+e^-$  reaction.

This method can also be successful for the  $\bar{p}p \rightarrow J/\Psi \pi^0 \rightarrow e^+e^-\pi^0$ , as will be shown in the next chapter, as well as for many other electromagnetic channels involving the production of an  $e^+e^-$  pair or charmonium decay of the type  $Y \rightarrow J/\Psi X \rightarrow e^+e^-X$ .

This method is now available in PANDARoot.

---

## Chapter 6

# Feasibility studies of $\pi$ -N TDAs for PANDA experiment

We have introduced the TDA formalism in the section 3.3, where we have also summarized the feasibility studies of the  $\bar{p}p \rightarrow e^+e^-\pi^0$  reaction. In this chapter, we will continue to discuss the feasibility studies of  $\pi$ -N TDAs in  $\bar{p}p \rightarrow J/\Psi\pi^0 \rightarrow e^+e^-\pi^0$  reaction.

### 6.1 The $\pi$ -N TDA in the $\bar{p} \rightarrow J/\Psi\pi^0$ reaction

Recently, a new model for TDAs measurement in the  $\bar{p}p \rightarrow J/\Psi\pi^0 \rightarrow e^+e^-\pi^0$  reaction was proposed [10]. The advantage of this reaction with respect to the non resonant  $\bar{p}p \rightarrow \gamma^*\pi^0$  reaction is the higher counting rate, as will be discussed in more details in section 6.2.5.5. In addition, as  $q^2$  is fixed to the squared  $J/\Psi$  mass ( $q^2 = M_{J/\Psi}^2 = 9.54 \text{ (GeV}/c^2)^2$ ) which is a relative high value, the factorization regime is likely to be reached. Indeed, it is well known that the  $J/\Psi \rightarrow \bar{p}p$  decay is well described by pQCD [85]. This process is a background for charmonium decay, for example  $\bar{p}p \rightarrow h_c \rightarrow J/\Psi\pi^0$  where  $h_c$  has a mass of  $3510 \text{ MeV}/c^2$ , which adds of the interest to this study.

#### 6.1.1 The model

Figure 6.1 depicts the factorization approach of the annihilation reaction  $\bar{p}p \rightarrow J/\Psi\pi^0$ . Three ingredients are needed: DA, TDA and  $J/\Psi$  wave function. The left picture corresponds to the backward kinematics with  $u \sim 0$  which gives access to  $\pi - N$  TDA, and the right one to the forward kinematics with  $t \sim 0$  which gives access to  $\pi - \bar{N}$  TDA.

In [10], the calculation of the  $\bar{p}p \rightarrow J/\Psi\pi^0$  amplitude follows the same steps as the classical calculation of the  $J/\Psi \rightarrow p\bar{p}$  amplitude in the pQCD framework. The only difference is the presence of the TDA in the amplitude of the  $\bar{p}p \rightarrow J/\Psi\pi^0$ .

The amplitude reads:

$$|\bar{M}_T|^2 = \frac{1}{4}|C|^2 \frac{2(1+\epsilon)}{\xi \bar{M}^8} (|I(\xi, \Delta^2)|^2 - \frac{\Delta_T^2}{m_N^2} |I'(\xi, \Delta^2)|^2). \quad (6.1)$$

Here,  $\xi$  and  $\Delta^2$  are the variables defined in section 3.3. The factor C is:

$$C = (4\pi\alpha_s)^3 \frac{f_N^2 f_\psi}{f_\pi} \frac{10}{81} \quad (6.2)$$

---

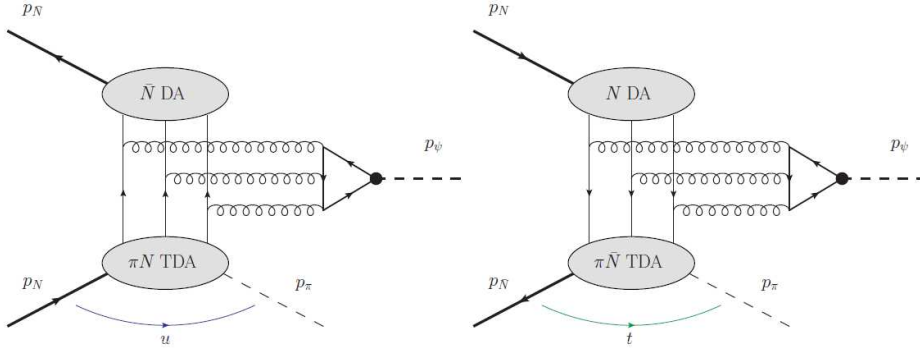


Figure 6.1: Factorization of the annihilation process  $\bar{p}p \rightarrow J/\Psi \pi^0$ . Left: backward  $\pi^0$  emission. Right: forward  $\pi^0$  emission.

here,  $f_\pi = 93$  MeV is the pion weak decay constant and  $f_N$  determines the value of the nucleon wave function at the origin. The normalization constant  $f_\psi$  is extracted from the charmonium leptonic decay width  $\Gamma(J/\Psi \rightarrow \bar{p}p)$ , the value is  $413 \pm 8$  MeV.  $\alpha_s$  stands for the strong coupling.

In eq 6.1, I and I' are the convolution integrals over the fractions  $x_i$  and  $y_i$  of the longitudinal momentum of the proton for each quark in the range allowed by the kinematics. I and I' contain:

- the hard kernels corresponding to the diagrams in fig 6.2
- the nucleon DAs
- the  $\pi N$  and  $\pi \bar{N}$  TDAs

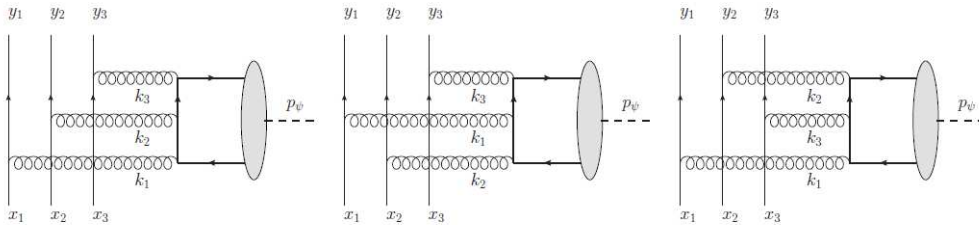


Figure 6.2: Feynman diagrams describing  $J/\Psi \pi$  production sub-process at the Born order.

As suggested in [62], the simple nucleon exchange model for  $\pi N$  TDAs is used to get a rough estimation of the cross section (see figure 3.17). For this model,

$$I(\xi, \Delta^2) = \frac{f_\pi g_{\pi NN} m_N (1 - \xi)}{(\Delta^2 - m_N^2)(1 + \xi)} M_0 \quad (6.3)$$

$$I'(\xi, \Delta^2) = \frac{f_\pi g_{\pi NN} m_N}{(\Delta^2 - m_N^2)} M_0 \quad (6.4)$$

The spectral part is omitted in the calculation since it is not the dominant part.  $g_{\pi NN} \simeq 13$  is the pion-nucleon coupling.  $M_0$  is related to the  $J/\Psi \rightarrow \bar{p}p$  decay width by:

$$\Gamma(J/\Psi \rightarrow \bar{p}p) = (\pi\alpha_s)^6 \frac{1280f_\psi^4 f_N^4}{243\pi\bar{M}^5} |M_0|^2 \quad (6.5)$$

$M_0$  can be calculated by using various DA models. However, this relation also depends on the value of  $\alpha_s$  which can not be fixed unambiguously. The procedure chosen in [10] is to fix  $\alpha_s$  for each DA model to reproduce the  $J/\psi \rightarrow \bar{p}p$  branching ratio. It means that  $\alpha_s^6 |M_0|^2$  does not depend on the DA model and neither does the cross section for the  $\bar{p}p \rightarrow J/\psi\pi^0$  reaction.

The situation is therefore very different from the case of  $\bar{p}p \rightarrow e^+e^-\pi^0$  where a strong dependence on the model had been observed (section 3.3, figure 3.14).

The general formula to calculate the cross section of the  $\bar{p}p \rightarrow J/\Psi\pi^0$  reaction is:

$$\frac{d\sigma}{d\Delta^2} = \frac{1}{16\pi\Lambda^2(s, m_N^2, m_N^2)} |\bar{M}_T|^2 \quad (6.6)$$

where  $\Lambda^2(x, y, z) = \sqrt{x^2 + y^2 + z^2 - 2xy - 2xz - 2yz}$  and  $|\bar{M}_T|^2$  is given by eq 6.1.

The physical kinematical domain for the reaction  $\bar{p}p \rightarrow J/\psi\pi^0$  reaction in the backward regime is determined by the requirement that the transverse momentum transfer should be space-like:  $(p_\pi - p_{\bar{N}})_T^2 \equiv \Delta_T^2 \leq 0$ , where

$$\Delta_T^2 = \frac{1 - \xi}{1 + \xi} \left( t - 2\xi \left[ \frac{m_N^2}{1 + \xi} - \frac{m_\pi^2}{1 - \xi} \right] \right) \quad (6.7)$$

In principle, the model is valid only for small  $\Delta_T^2$  (i.e. forward or backward angles). However, it is impossible to predict the exact range of validity, since the corrections can not be calculated. The philosophy will be to compare the experimental angular distribution to the measured one to test how the model works.

## 6.1.2 Cross section estimation

### 6.1.2.1 Numerical results

The differential cross section  $d\sigma/d\Delta^2$  obtained with this model is given in figure 6.3 for  $\Delta_T^2 = 0$  as a function of  $W^2$ . Since, it decreases with  $W^2$ , the reaction will be easier to measure at lower  $W^2$ . However, it will be necessary to measure the reaction at different  $W^2$  to check the factorization. With the antiproton beams at FAIR, values of  $W^2$  from 10.4 GeV<sup>2</sup> (which is the reaction threshold) up to 28 GeV<sup>2</sup> can be achieved. It will be interesting to measure the reaction at different  $W^2$  to check the factorization approach and also to measure the TDAs for different  $\xi$ .

### 6.1.2.2 Comparison with the data

The existing data from Fermilab (E760, E835) [86] [87] show a total cross section of the  $J/\psi$  production reaction in the range [0.09 nb, 0.23 nb] for the total energy of reaction about 3.5 GeV in  $\bar{p}p$  annihilation (figure 6.4). Despite the large error bars, these measurements give a very useful constraint for the model. For this reason, we chose  $s = 12.25$  GeV<sup>2</sup> for the feasibility study within the TDA model. The result of differential cross section as a function of  $t$  is shown in figure 6.5 for  $s=12.25$  GeV<sup>2</sup>.

If we integrate the differential cross section in figure 6.5, for this TDA model we find a total cross section for the  $t$  channel ( $\pi^0$  emission at the forward direction) of 105.8 pb. Considering also the backward pion emission, the cross section will be doubled, giving a value of 210 pb, which is comparable with the existing data.

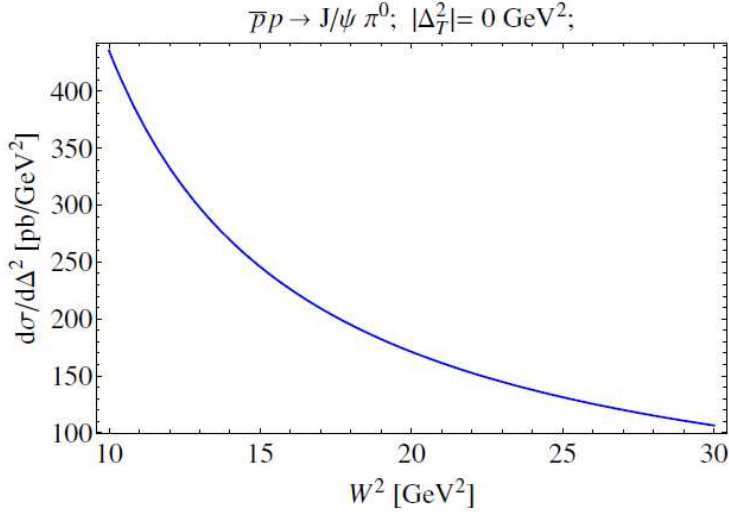


Figure 6.3: Differential cross section  $d\sigma/d\Delta^2$  for the  $\bar{p}p \rightarrow J/\Psi\pi^0$  reaction at  $\Delta_T^2 = 0$  as a function of  $W^2$ .

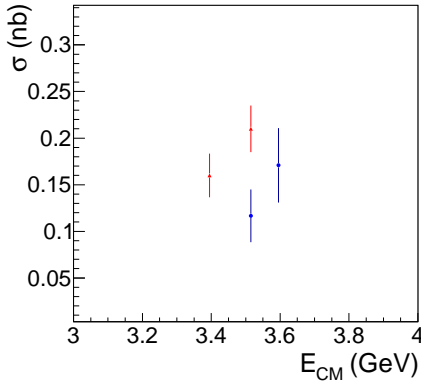


Figure 6.4: The cross section from the E760 (blue) and E853 (red) experiments at Fermilab.

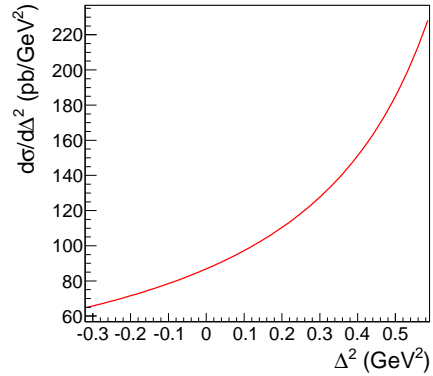


Figure 6.5: Differential cross section for  $\bar{p}p \rightarrow J/\Psi\pi^0$  reaction as a function of  $\Delta^2=t$  at  $W^2 = 12.25 \text{ GeV}^2$ .

### 6.1.3 Alternative models

The  $J/\psi$  production by the  $\bar{p}p$  annihilation reaction can also be described by the effective Lagrangian calculation [88] [89] following the graphs in figure 6.6. A recent calculation has been performed in Orsay by J. Van de Wiele and S. Ong ([88]). In this model, the hadronic form factors at the  $NN\pi$  vertex are introduced to take into account the offshellness of the nucleon.

Due to the spin 1 of the  $J/\Psi$ , the Lagrangian depends on two coupling constants  $K$  and  $\kappa$ , which are complex quantities. The known  $J/\Psi \rightarrow \bar{p}p$  branching ratio ( $2.17 \pm 0.08 \cdot 10^{-3}$ ) and angular distribution ( $1 + \alpha \cos^2\theta$  with  $\alpha = 0.595 \pm 0.012$ ) put constraints on the values of these parameters.

Two forms can be used for the  $\pi NN$  Lagrangian, a pseudo-scalar, or a pseudo-vector (see [88] for details).

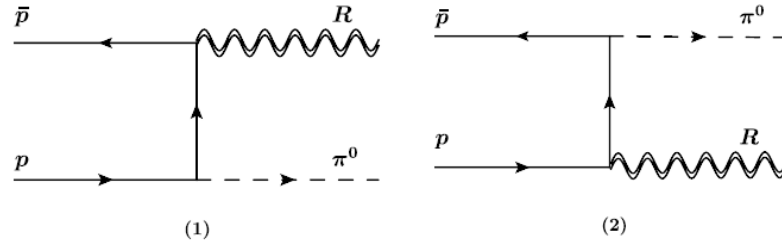


Figure 6.6: Feynman diagrams for the nucleon-pole model in  $\bar{p}p \rightarrow J/\Psi \pi^0$  reaction using the hadronic form factors. Here  $R$  is the  $J/\Psi$ .

As can be seen in figure 6.7, the magnitude and the evolution of the cross section with energy depends on the choice of pseudo-vector or pseudo-scalar couplings. It can also be observed in figure 6.8 that the shape of the angular distribution also strongly depends on the choice of the  $\pi NN$  coupling.

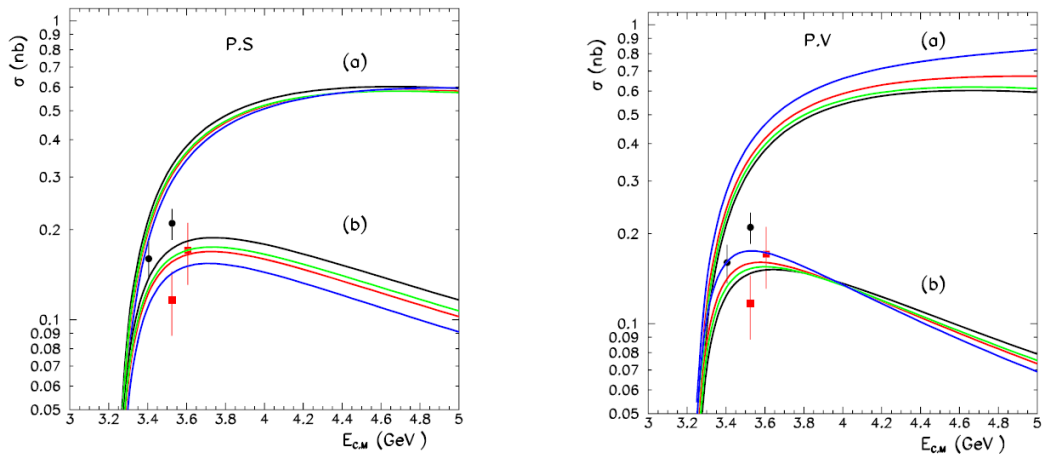


Figure 6.7: Total cross section versus  $E_{cm}$  for the  $\bar{p}p \rightarrow J/\Psi \pi^0$  reaction in the model of [88], assuming pseudo-scalar ( $\pi NN$ ) coupling (left) and pseudo-vector ( $\pi NN$ ) coupling (right). The color line of different curves corresponds to the different Lagrangian parameter values. Model without hadronic form factor: (a), and with dipole form factor: (b)

This approach, as well as other existing calculations, give additional motivation to study the  $\bar{p}p \rightarrow J/\Psi \pi^0$  reaction [90] [91] [92]. The main goal here is to test a description in terms of meson-nucleon couplings and nucleon-antinucleon annihilation into charmonium.

## 6.2 Feasibility study for $\bar{P}$ ANDA

### 6.2.1 Event generator

A new event generator model for the  $\bar{p}p \rightarrow J/\Psi \pi^0$  reaction is constructed in the PANDARoot framework based on the TDA model [10].

In this generator, the rejection Monte Carlo method is used. Two pseudo variables, the 4

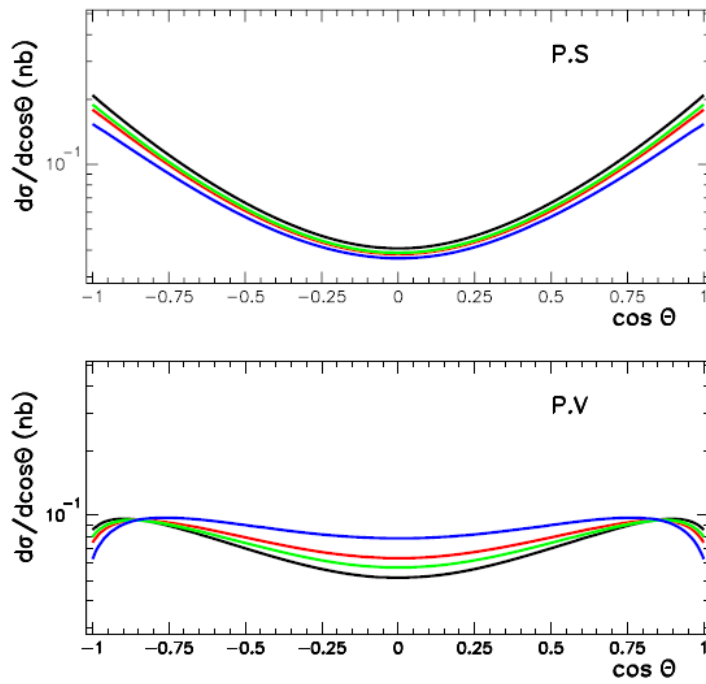


Figure 6.8: Angular distribution of the differential cross section for  $E_{cm} = 3.5$  GeV and for  $\bar{p}p \rightarrow J/\Psi\pi^0$  with hadronic form factors ( $\theta = \theta_{\pi^0} - \theta_p$ ).

momentum transfer  $t$  and the probability  $p$  at this  $t$ , are generated. If the probability is smaller than the value calculated with the formula mentioned in section 6.1.1, it is accepted, otherwise rejected.

The generator uses  $s$ , the total energy of the reaction, as input parameter and can work for either  $t$  or  $u$  channel.

To test the generator, we first generate 10000 events of  $\bar{p}p \rightarrow J/\Psi\pi^0$  at  $s = 12.25 \text{ GeV}^2$ . The distribution of 4 momentum transfer between antiproton and pion is shown in figure 6.9. The shape of the distribution is the same as the differential cross section in figure 6.5. The minimum and maximum value of  $t$  corresponds to the pion emission at  $90^\circ$  and  $0^\circ$  in the center of mass system, respectively.

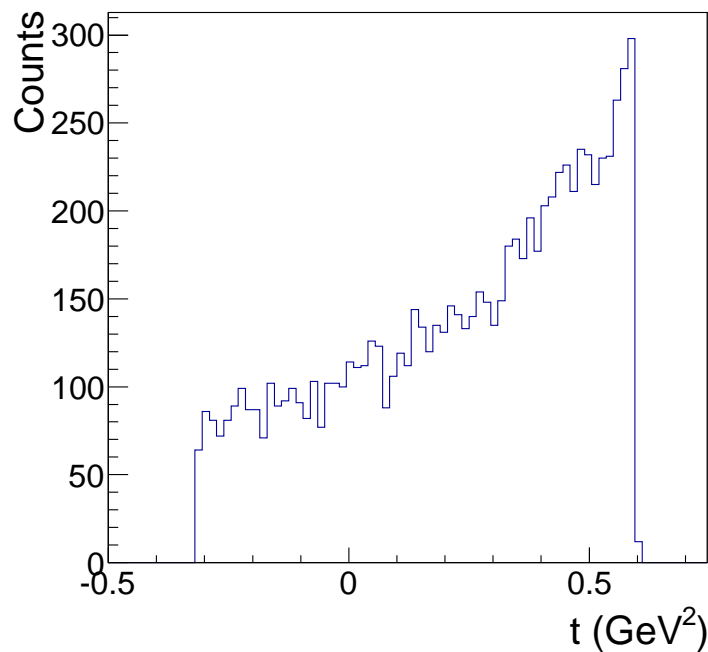


Figure 6.9: Distribution of squared four-momentum transfer  $t$  using the TDA event generator for 10000 events at  $W^2 = 12.25 \text{ GeV}^2$ .

### 6.2.2 Counting rate study

The counting rate for the  $\bar{p}p \rightarrow J/\Psi\pi^0$  reaction is estimated using the formula:

$$N = \sigma \cdot I \cdot t \cdot \epsilon \cdot Br \quad (6.8)$$

Here,  $\sigma$  is the total cross section of this reaction. For the forward pion emission, this value is 105.8 pb for  $s = 12.25 \text{ (GeV/c)}^2$  as discussed in section 6.1.2.1.  $I \cdot t$  is the integrated luminosity. In the  $\bar{P}$ ANDA experiment, assuming the nominal luminosity of  $2 \cdot 10^{32} \text{ cm}^{-2} \text{ s}^{-1}$  the integrated full luminosity for four months is about  $2 \text{ fb}^{-1}$ .  $\epsilon$  is the detection efficiency which contains the efficiency of  $e^+e^-$  detection (79.2%), the efficiency of  $\pi^0$  reconstruction (80%), the  $e^+e^-$  invariant mass cut (64%) and the efficiency of PID (50%). We will assume here a signal efficiency of 20%.  $Br$  is the branching ratio of  $J/\Psi$  decaying to  $e^+e^-$ , the value is  $5.94 \pm 0.06\%$ .

After numerical application, the counting rate for the t channel, forward  $\pi^0$  emission, is about 2600 events. Considering also the backward pion emission, the value is doubled, so we expect 5200 events.

Figure 6.10 shows the number of expected counts in the conditions described above in bins of t. The bin size here is  $0.015 \text{ GeV}^2$ .

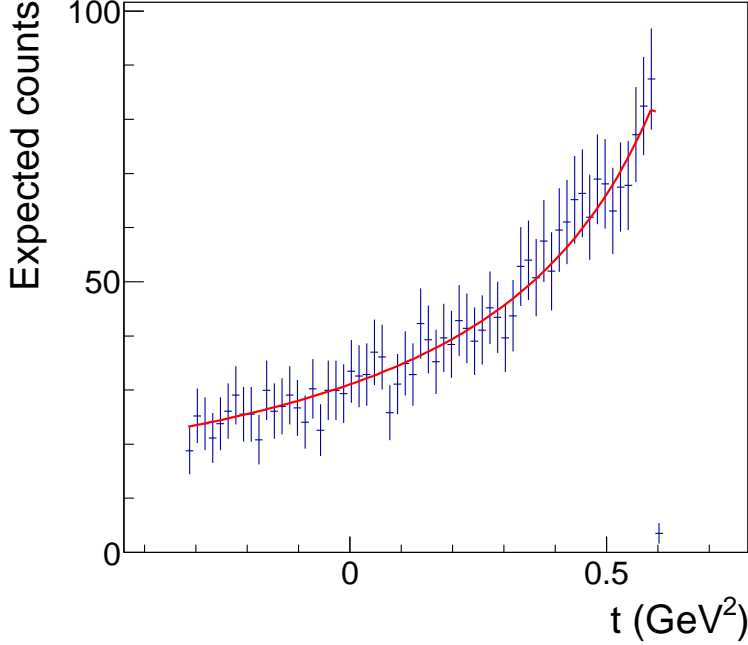


Figure 6.10: Expected counting rates for an integrated luminosity of  $2 \text{ fb}^{-1}$  for the near forward regime of the  $\bar{p}p \rightarrow J/\psi \pi^0$  reaction in bins of t (bin width of  $0.015 \text{ GeV}^2$ ) taking into account the experimental efficiencies (see text). The red line shows the shape of the theoretical prediction from the TDA model.

This shows that the statistics is large enough to study this signal.

### 6.2.3 Kinematics consideration

Since the performance of the reconstruction of the signal depends on the kinematics of the reaction, it is instructive to study its main characteristics first, as shown in figure 6.11. All the figures are obtained using a phase space decay model. Due to its large mass, the  $J/\psi$  is emitted at the very forward direction with a maximum angle of  $4^\circ$ . For a given laboratory angle, the  $J/\psi$  can be found with two energies corresponding to the forward and backward emission in the center of mass.

The  $e^+$  and  $e^-$  from the  $J/\psi$  decay are emitted at all angles. Their energy is strongly correlated to their angle, the width of the correlation is related to the distribution of the emission angle. For a given laboratory angle, the lowest energy corresponds to the emission of  $J/\psi$  at  $180^\circ$  in the center of mass and the highest energy to the emission at  $0^\circ$ . However this effect is relatively small and the correlation is relatively narrow. The kinematics is in fact very close to the one of a decaying  $J/\psi$  at rest in the laboratory. The detection is more important in the target spectrometer. The fraction of electrons in the forward spectrometer is very small.

The  $\pi^0$ s are emitted in all directions. Their energy is correlated to the angle according to the 2-body kinematics. They have rather low energy.

The opening angle of the two  $\gamma$ s is always larger than  $12^\circ$ , which corresponds to more than 5 crystals in EMC. The discrimination of the two photons is therefore very easy.

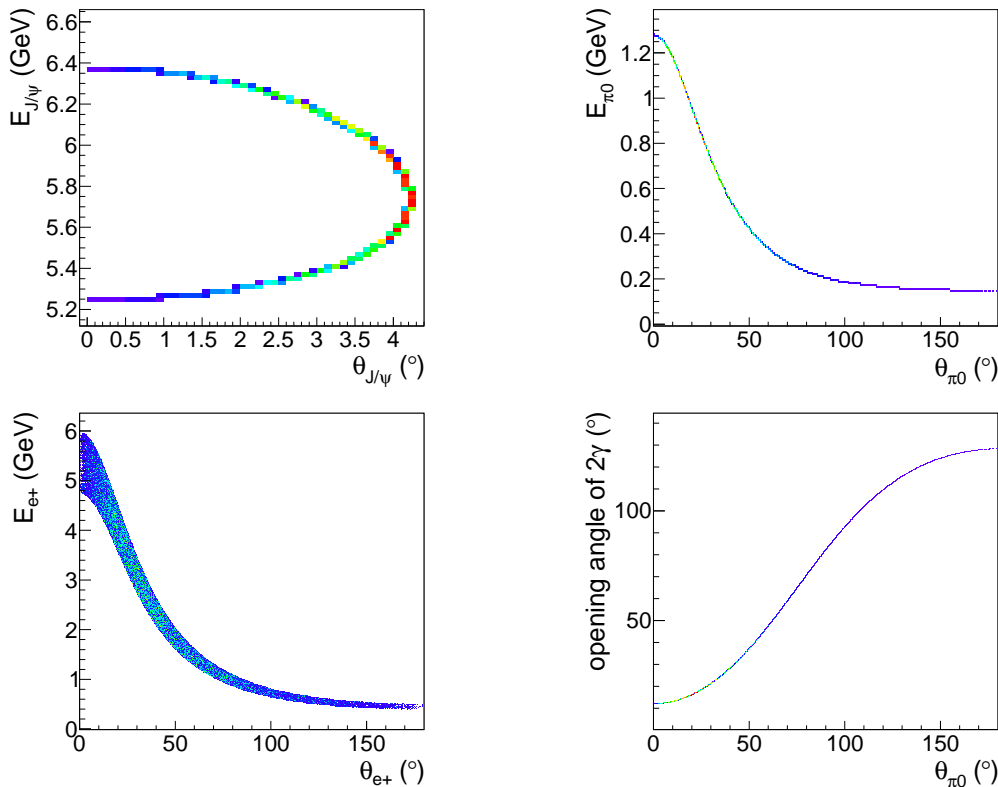


Figure 6.11: Kinematic consideration for the  $\bar{p}p \rightarrow J/\Psi\pi^0$  reaction. Top-Left:  $J/\psi$  total energy as a function of its polar angle. Top-right:  $\pi^0$  total energy as a function of its polar angle. Bottom-left: Positron total energy as a function of its polar angle. Bottom-right: the minimum opening angle of the two photons from  $\pi^0$  decay.

#### 6.2.4 Effect of bremsstrahlung correction method on the signal detection

As the invariant mass of  $e^+e^-$  is useful for the signal selection, a correct electron momentum reconstruction is important. So the Bremsstrahlung correction method, presented in section 5.2, can also be used in this channel to improve the electron momentum reconstruction.

To show this, a full simulation of 10000 events of the  $\bar{p}p \rightarrow J/\Psi\pi^0 (J/\Psi \rightarrow e^+e^-)$  reaction using the generator described in section 6.2.1 is done. Figure 6.12 shows the comparison of the distribution of  $e^+e^-$  invariant mass with and without using the bremsstrahlung correction method. As can be seen in the figure and table 6.1, the peak position is perfectly centered after the correction, and most importantly, the number of events inside  $2\sigma$  is increased by a factor 1.5. It is very important to have a narrow peak with reduced tails. Indeed, to reject as much as possible background events, a narrow window around the  $J/\Psi$  mass will be applied. With the correction method, 64% of the events have an  $e^+e^-$  invariant mass in the range  $[2.96, 3.22]$   $\text{GeV}/c^2$ , which corresponds to an improvement of a factor 1.7.

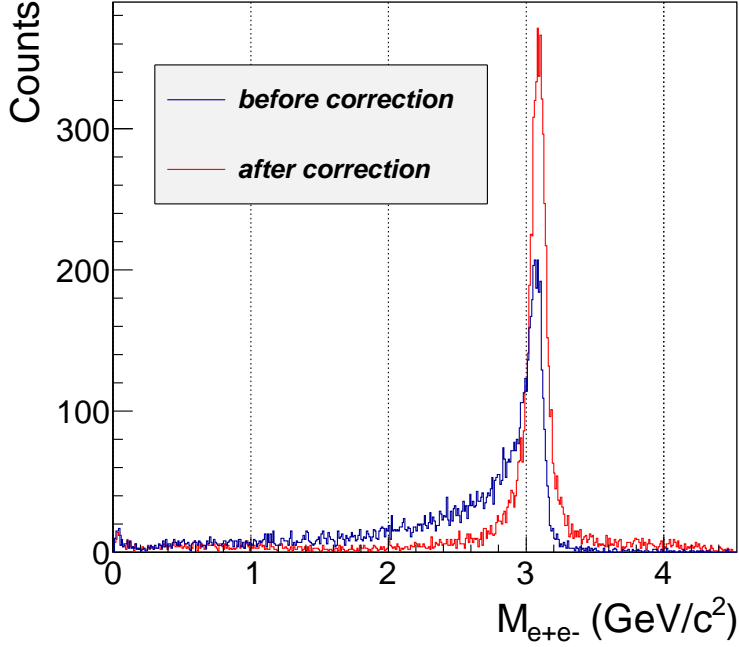


Figure 6.12: Distribution of the  $e^+e^-$  invariant mass before (blue) and after (red) using the Bremsstrahlung correction method for  $\bar{p}p \rightarrow J/\Psi \pi^0$  reaction.

	peak position	$\sigma$	$N_{2\sigma}$	$N_{\Delta M}$
before correction	$3.045 \pm 0.002 \text{ GeV}/c^2$	$70 \pm 1 \text{ MeV}/c^2$	42%	37%
after correction	$3.086 \pm 0.001 \text{ GeV}/c^2$	$65 \pm 1 \text{ MeV}/c^2$	64%	64%

Table 6.1: The peak position correction and signal selection improvement using the Bremsstrahlung correction method. Here, the peak position and  $\sigma$  are from a Gaussian fit.  $N_{2\sigma}$  is the number of events inside the  $2\sigma$  of the Gaussian fit.  $N_{\Delta M}$  is the number of events inside the cut  $[2.96, 3.22] \text{ GeV}/c^2$ .

### 6.2.5 Background consideration

The main contribution to the background for the measurement of the  $\bar{p}p \rightarrow J/\psi \pi^0$  cross section comes from  $\bar{p}p \rightarrow \pi^+ \pi^- \pi^0$ . This is due, as will be described in the following, to the large cross section for this reaction and the possibly misidentified charged pions as electrons. The event topology and kinematics of these two reactions are very similar. Achieving a significant rejection of charged pions while keeping a good efficiency of electron identification is absolutely essential for this measurement as will be illustrated below.

In the following, we will try to estimate the signal over background ratio that can be expected after data analysis. We first introduce the needed inputs for this estimate and then explain how they can be determined.

Background (corresponding to  $\bar{p}p \rightarrow \pi^+ \pi^- \pi^0$ ) and signal (corresponding to  $\bar{p}p \rightarrow J/\Psi \pi^0 \rightarrow e^+ e^- \pi^0$ ) events will be produced with cross sections  $\sigma_S$  and  $\sigma_B$  respectively. When processing the data, the signal and background events will be reconstructed with efficiencies respectively  $\epsilon_{rec,S}$  and  $\epsilon_{rec,B}$ . Then, PID cuts will be applied, with efficiencies respectively  $\epsilon_{PID,S}$  and  $\epsilon_{PID,B}$  as well as a cut on the  $e^+e^-$  invariant mass around the  $J/\Psi$  mass, with efficiencies  $\epsilon_{J/\psi,S}$  and  $\epsilon_{J/\psi,B}$ . Br is the  $J/\Psi \rightarrow e^+e^-$  branching ratio.

The signal over background ratio in the selected events can be written as:

$$\frac{S}{B} = \frac{Br \times \epsilon_{rec,S} \times \epsilon_{PID,S} \times \epsilon_{J/\psi,S} \times \sigma_S}{\epsilon_{rec,B} \times \epsilon_{PID,B} \times \epsilon_{J/\psi,B} \times \sigma_B} \quad (6.9)$$

#### 6.2.5.1 Total cross section of the $\pi^+ \pi^- \pi^0$ background

Although existing measurements of  $\bar{p}p \rightarrow \pi^+ \pi^- \pi^0$  given in [93], and shown in Figure 6.13 in the relevant kinematic range relevant for PANDA have high uncertainties, they can still be used as a reasonable estimate of the total cross section of this background to expect.

The two closest measurements to the energy chosen for our study have been obtained respectively at 4.6 GeV/c ( $\sigma=0.19 \pm 0.03$  mb) [94] and at 5.7 GeV/c ( $\sigma=0.12 \pm 0.01$  mb) [95]. Based on that, we estimate a cross section at  $p=5.51$  GeV/c of  $0.2 \pm 0.05$  mb. This value is in agreement with the DPM and FTF models, which are two hadronic models commonly used in the PANDA energy range.

Since the cross section for the  $\bar{p}p \rightarrow J/\Psi \pi^0$  is in the range [0.09, 0.2 nb] (see section 6.1.2.2), it means that, taking into account the  $J/\Psi \rightarrow e^+e^-$  branching ratio of  $5.94 \pm 0.06\%$ , the cross sections of the signal reaction  $\bar{p}p \rightarrow J/\Psi \pi^0 \rightarrow e^+e^- \pi^0$  is in the range [5.4, 12 pb], i.e, a factor  $1.3\text{-}4.6 \cdot 10^7$  lower than the background. However, as will be discussed later, the cross section of the  $\bar{p}p \rightarrow \pi^+ \pi^- \pi^0$  integrated over the kinematic region relevant for the  $\bar{p}p \rightarrow J/\Psi \pi^0$  reaction is about a factor 10 lower.

#### 6.2.5.2 Reconstruction efficiency

As mentioned in section 6.2.2, the reconstruction efficiency for an  $e^+e^-$  pair, which also includes the geometrical acceptance is of the order of 79.2%. In addition, the  $\pi^0$  reconstruction efficiency is of the order of 80% for momenta below 3.5 GeV/c (private communication with R. Kunne). Based on these numbers, we expect a signal reconstruction efficiency of  $\epsilon_{rec,S} = 63\%$ .

We have seen in section 4.3.3 that the reconstruction efficiencies for charged pions and charged electrons differ only by a few %. Since, the kinematics of the background and signal events is also similar, there is no reason to expect a large difference in the efficiencies for the

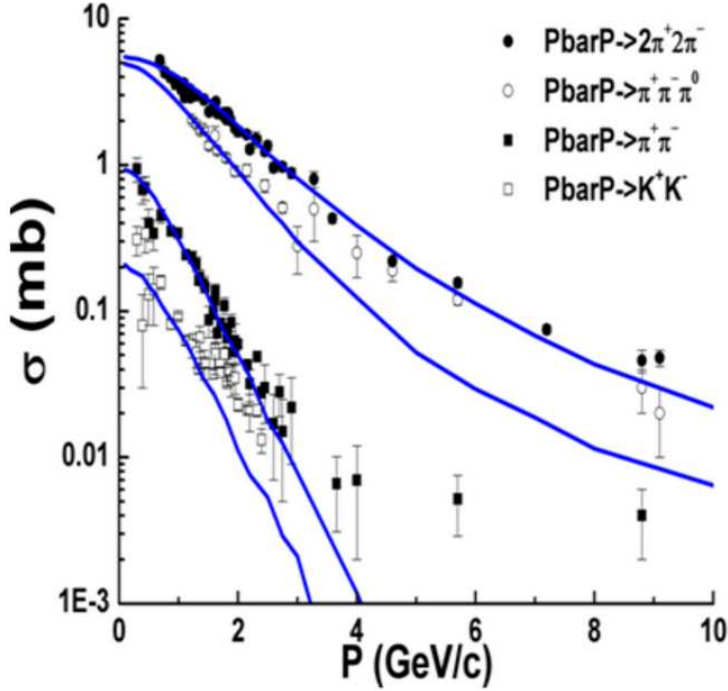


Figure 6.13: Various antiproton induced multi pion reaction cross sections as a function of momentum of antiprotons.

$e^+e^-\pi^0$  and  $\pi^+\pi^-\pi^0$  events, especially for the events with invariant mass of the charged pair inside the  $J/\Psi$  mass window.

For our estimate, we therefore take  $\epsilon_{rec,S}=\epsilon_{rec,B}$ .

### 6.2.5.3 PID efficiency

According to equation 6.9, we need to have reasonable estimates for signal and background efficiencies after the PID cuts ( $\epsilon_{PID,S}$  and  $\epsilon_{PID,B}$ ). Since we did not perform full scale simulations of signal and background reactions, we will estimate the needed numbers based on the single track PID performance plots shown in section 4.2.5.4. According to fig.4.15, a residual pion contamination  $\epsilon_{PID,\pi}$  better than  $3\cdot 10^{-4}$  can be reached at all momenta by applying a condition on the PID probability to be larger than 99%. With this condition, the electron single track efficiency  $\epsilon_{PID,e}$  increases from 70% for  $p > 1$  GeV/c to 90% for  $p=4.5$  GeV/c. Unfortunately, the study was limited to  $p < 5$  GeV/c. However, according to fig.4.14, the performance for electron/pion identification should be rather similar at higher energies. Concerning the lower energies, the electron efficiency is slightly lower (about 40% at 0.5 GeV/c which is the minimum energy allowed by the kinematics of the  $\bar{p}p \rightarrow J/\Psi \pi^0$  reaction). However, the pion efficiency is also significantly lower (better than  $10^{-4}$  between 0.5 and 1 GeV/c), so a different cut on the global PID probability could probably produce an increased electron efficiency, while keeping the pion rejection rate to a value lower than  $3\cdot 10^{-4}$ . In addition, the contribution of electrons with laboratory momenta lower than 1 GeV/c is small and these electrons will be emitted together with a partner at high momenta. As we need for our very simple background estimates an average single track efficiency, a reasonable guess is  $\epsilon_{PID,e}=0.7$  and  $\epsilon_{PID,\pi}=3\cdot 10^{-4}$ .

We then deduce:  $\epsilon_{PID,S} = \epsilon_{PID,e}^2 = 0.7 \times 0.7 = 0.49$  and  $\epsilon_{PID,B} = \epsilon_{PID,\pi}^2 = 3 \cdot 10^{-4} \times 3 \cdot 10^{-4} = 9 \times 10^{-8}$ .

#### 6.2.5.4 Effect of the $e^+e^-$ invariant mass cut

Since a cut on the  $e^+e^-$  invariant mass centered at the  $J/\Psi$  mass will be applied to select the signal, it is important to study the distribution of background events as a function of this variable. There is no useful experimental information available. However, we can use different models.

I simulated  $10^5$  events using the phase space models, and I used  $10^5$  events generated with the DPM model [96], and also  $10^5$  events generated with the FTF model [97] [98] by Aida Galoyan (Dubna). As introduced in section 4.2.1, DPM and FTF are two models suited for high energy simulations of hadronic processes and fitted to existing data.

The results for the invariant mass of the  $\pi^+\pi^-$  pair is shown in Figure 6.14 for the phase space model and in Figure 6.15 for the FTF and DPM models. As expected the phase space model shows no structures, whereas one can see clear resonance peaks ( $\rho$  and  $f_2$ ) in the DPM distribution. Although a bump is visible on the FTF invariant mass distribution, its width is too large to be accounted for by resonances. In all three cases, there is no rapid change of cross section as a function of the invariant mass. Therefore for a signal peaked on a small invariant mass window such as  $J/\psi \rightarrow e^+e^-$  the invariant mass cut will contribute to the improvement of signal to background.

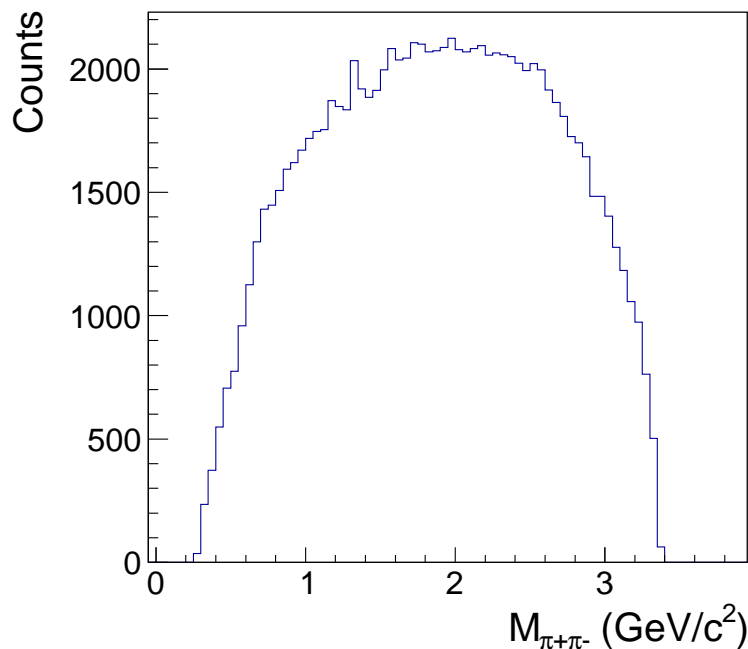


Figure 6.14: Distribution of the  $\pi^+\pi^-$  invariant mass for the  $\bar{p}p \rightarrow \pi^+\pi^-\pi^0$  reaction using the simulation of phase space ( $s = 12.5 \text{ GeV}^2$ ).

There is no peak in the region of the  $J/\Psi$  mass. This is due to the very small branching ratio of  $J/\Psi \rightarrow \pi^+\pi^-$  ( $1.47 \pm 0.23 \cdot 10^{-4}$ ). Since the  $J/\Psi \rightarrow e^+e^-$  signal is peaked in a small invariant mass window around the  $J/\Psi$  mass, it is clear that the signal over background ratio will be improved significantly by a cut on the invariant mass. To make this more quantitative, we

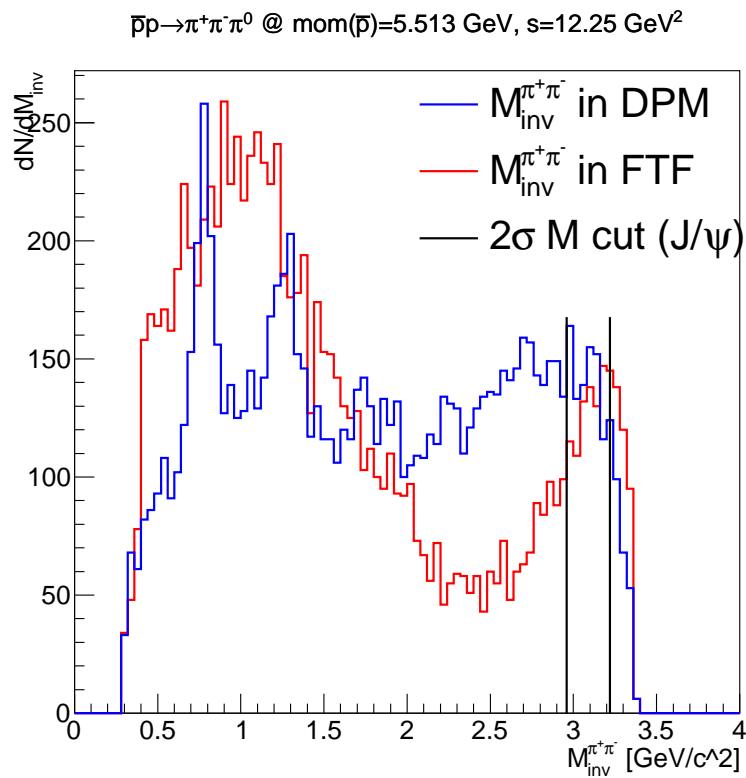


Figure 6.15: Distribution of the  $\pi^+\pi^-$  invariant mass for  $\bar{p}p \rightarrow \pi^+\pi^-\pi^0$  reaction using the simulation of DPM and FTF ( $s = 12.5 \text{ GeV}^2$ ).

calculate for each model, the number of  $\pi^+\pi^-\pi^0$  events inside a cut  $[M_{J/\psi}-0.13, M_{J/\psi} +0.13]$ . Following these results, we estimate  $\epsilon_{J/\psi,B} = 0.08$ .

As shown in section 6.2.4, the efficiency of this cut on the signal is  $\epsilon_{J/\psi,S} = 0.64$ .

### 6.2.5.5 Numerical application

Combining all the information given above, a rough quantitative estimate of the signal to background ratio can be obtained using Eq.6.9. We find S/B  $\sim$  2.6.

In the feasibility study of the form factor measurement [45], where the signal consisted in  $\bar{p}p \rightarrow e^+e^-$  and the main background in  $\bar{p}p \rightarrow \pi^+\pi^-$ , an additional background rejection factor of the order of 50 is attainable by using kinematic constraints. Although kinematic constraints may not be as effective with the  $\bar{p}p \rightarrow e^+e^-\pi^0$  channel as much as in the form factor measurement case ( $\bar{p}p \rightarrow e^+e^-$  channel), we expect that some improvement of the above estimation of the signal to background ratio will be attainable. Further investigation of the effectiveness of the kinematic cuts is ongoing at IPN.

Finally, the non resonant  $\bar{p}p \rightarrow e^+e^-\pi^0$  reaction can also be a background. Using fig. 3.16, we can estimate a differential cross section  $d^2\sigma/dtdQ^2 \sim 0.03$  pb/GeV/GeV<sup>2</sup> for  $s=12.25$  GeV/c<sup>2</sup> and  $Q^2=9.54$  GeV/c<sup>2</sup>. By integrating it over a  $t$  region corresponding to the forward hemisphere (i.e. about 1 GeV), we obtain  $d\sigma/dQ \sim 0.03$  pb/GeV<sup>2</sup>. We then integrate this value over a  $Q^2$  range of 1.61 GeV/c<sup>2</sup> corresponding to  $[M_{J/\psi}-0.13$  GeV,  $M_{J/\psi} +0.13$  GeV] (see section 6.2.5.4) and found a value of 0.048 pb, i.e. less than 1% of the J/ $\psi$  signal.

We can notice that, in this range of  $Q^2$  and  $s$ , we find a ratio of the cross sections

$$\sigma(\pi^+\pi^-\pi^0)/\sigma_{nonres}(e^+e^-\pi^0) \sim 3 \cdot 10^8$$

, which is much larger than the value of  $10^6$  assumed for the studies of [66].

### 6.2.5.6 Angular distribution

The above estimates are averaged over all  $\pi^0$  angles. However, it will be needed to estimate the background in bins of  $t$  or of  $\theta_{\pi^0}$ .

The polar angular distribution of the  $\pi^0$  in the CM frame is shown in Figure 6.16 for the two string fragmentation models. Both models predict a distribution with a minimum at  $\theta = \pi/2$  that increases rapidly at small and large angles, but they differ by about a factor 2 in some regions. This confirms that it will be necessary to measure the  $\bar{p}p \rightarrow \pi^+\pi^-\pi^0$  reaction before studying the  $\bar{p}p \rightarrow e^+e^-\pi^0$  reaction.

Once, the total cross section and the angular distribution will be precisely measured, it will be possible to use these data to calculate the contamination and subtract it from the measured events.

## 6.3 Conclusion

In this chapter, an investigation of the feasibility of  $\pi$ -N TDA measurements was described. To perform this study, an event generator based on a TDA model was implemented inside the PandaRoot framework and used to calculate the count rate estimates for the  $\bar{p}p \rightarrow J/\Psi\pi^0$  reaction with forward  $\pi^0$  emission. Some ideas were put forward in order to get an estimate of the level of background to expect taking into account measured cross section of the main background source as well as the rejection power available using PID cuts and kinematical constraint. Using this information, the measurement of the  $\bar{p}p \rightarrow J/\Psi\pi^0$  signal is within reach, but

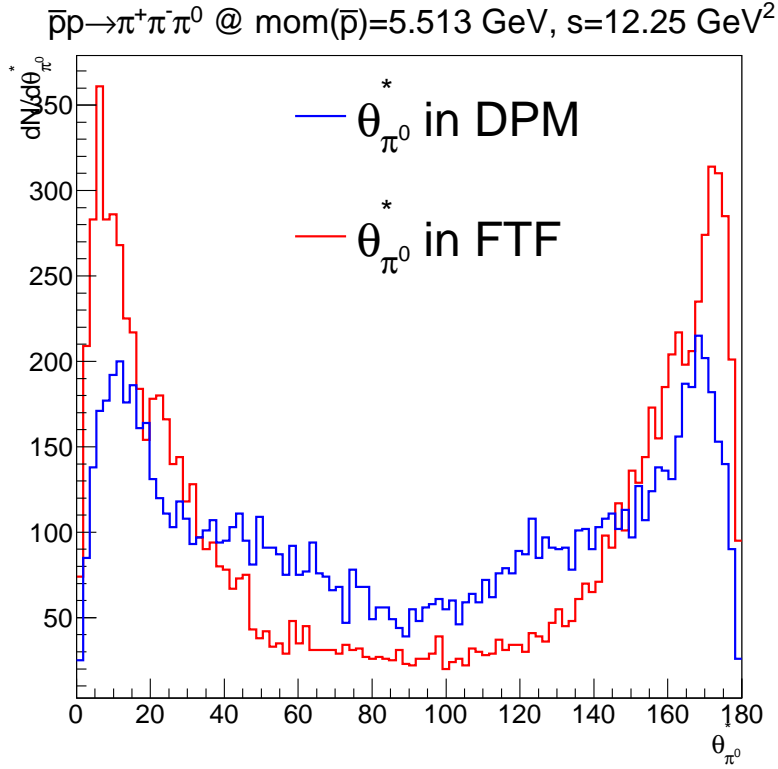


Figure 6.16: Distribution of the  $\pi^0$  polar angle  $\theta$  in the CM reference frame for the  $\bar{p}p \rightarrow \pi^+\pi^-\pi^0$  reaction in simulations based on the DPM and FTF models.

further investigation of the rejection power from kinematical constraints is needed to complete the work and further investigate the background contamination. In addition, the electron angular distribution needs to be studied in order to check the sensitivity to the  $1+\cos^2(\theta_e)$  trend expected for the factorization approach. It has to be mentioned that no real extraction of TDA is possible in these experiments, but the philosophy is to compare the data to calculations based on the factorization approach and a given TDA model.

---

## Chapter 7

# Conclusions and outlook

The  $\bar{\text{P}}\text{ANDA}$  (AntiProton ANnihilation at DArmstadt) experiment is one of the key projects at the future Facility for Antiproton and Ion Research (FAIR), which is currently under construction at GSI, Darmstadt. This experiment will perform precise studies of antiproton-proton annihilation reactions. It will benefit from antiproton beams with unprecedented intensity and quality in the momentum range between 1.5 and 15 GeV/c.

One of the important physics goals for the PANDA experiment is to perform studies of the internal structure of nucleons. Some aspects of this physics were investigated in this thesis through several studies.

First, the performance of the track finding has been investigated, as well as the momentum resolution and the Particle Identification using Pandaroot, the software for simulation and analysis for PANDA experiments. As main tracking detectors for the signal reconstruction for the PANDA experiment, a good acceptance and efficiency of MVD and STT detectors can give a better efficiency for the signal selection in the physics channels. So the determination of the efficiency and acceptance of the STT and MVD accurately is the first step. In this thesis, the STT acceptance and efficiency for different particles (muons, electrons and pions) are studied. The simulations of pion, electron and muon single events with PANDARoot framework show a good acceptance of STT except at the target pipe and very low momentum (less than 0.15 GeV/c) region. The tracking system efficiency has also a homogeneous distribution in the region of STT acceptance. The reason of the inefficiency for each type of particle is also studied, and found to be due to the differences in the type of interaction with the material of the detector components.

The second part focused on the development of a method for the correction of the effect of electron bremsstrahlung on momentum reconstruction. A momentum resolution study showed a sub-optimal result for electrons if bremsstrahlung effect is not handled properly. The resolution distribution exhibits a large tail and the center of the peak is also shifted. This was demonstrated to be due to the electron energy loss through bremsstrahlung. This is because the energy loss by bremsstrahlung has a non-Gaussian distribution, whereas the tracking algorithm using GEANE as a track follower treats the uncertainties as Gaussian. A new method based on an event by event treatment is developed. For each event, the signal of the photon that is emitted in the tracking system is searched in the EMC. Then a new electron momentum is calculated by adding the sum of the energies of such photons to the reconstructed momentum of the electron. In this method, the photon energy is reconstructed by using two algorithms. For photons emitted by the electron with small transverse momenta, the radius of curvature of the electron track is small, so it is easy to distinguish the electron and photon clusters in the EMC. For the photon emitted by the electron with large transverse momenta, the radius of curvature of the electron

---

track is large, so the clusters of the electron and the photon in the EMC are merged. A new algorithm based on the analysis of the azimuthal distribution of the energy deposited in the EMC crystals in the electron bumps was developed. With these two algorithms, the performance of electron reconstruction is improved significantly. The number of events inside  $2\sigma$  is improved by a factor of 1.33 in the Barrel region and 1.2 in the Forward Endcap region. The test for the electromagnetic form factors and TDA measurements demonstrate that the method is well suited to increase the signal reconstruction efficiency for electromagnetic channels.

Finally the third study was done to investigate the feasibility study of the baryon-to-meson transition distribution amplitudes (TDAs) measurement in the  $\bar{p}p \rightarrow J/\Psi\pi^0$  reaction within the PANDA experiment. TDAs are universal non-perturbative objects describing the transition between two different particles. The  $\pi - N$  TDAs parameterize the pionic content of the nucleon wave function. In this study, a new event generator based on the theoretical model [10] is developed and implemented in the PANDARoot framework. This event generator has been used for counting rate studies and background estimates, in combination with simulations of the  $\bar{p}p \rightarrow \pi^+\pi^-\pi^0$  background reaction. It was shown that for  $s = 12.25 \text{ GeV}^2$ , a statistics of 5200 signal events can be obtained with an integrated luminosity of  $2 \text{ fb}^{-1}$ . This number is obtained with a set of cuts on PID providing an electron pair efficiency of about 50% together with a signal over background ratio smaller than 3. Taking into account the fact that kinematic cuts can further reduce the background, this result is taken as very promising. Such studies need however to be continued to establish the final proof of the feasibility of TDA measurements. Such measurements are very challenging since they can potentially bring the very first results on hard exclusive electromagnetic processes in  $\bar{p}p$  annihilation. It has also to be noted that the  $J/\Psi\pi^0$  reaction is also interesting in other aspects, since theoretical calculations with hadronic models also exist. As a summary, this work is a contribution to the preparation of the measurement of electromagnetic channels with the PANDA detector. These measurements are very difficult, due to the low cross sections and the huge hadronic background. They are therefore very demanding in terms of performance of the detector and reconstruction software. The effort is worth it since such measurements would allow to access nucleon observables in a completely new kinematic domain, complementary to the one explored in electron scattering experiments.

---

# Bibliography

- [1] E. Rutherford, Phil. Mag. **6th series 37:222**, 581 (1919), *Collision of alpha particles with light atoms. an anomalous effect in nitrogen.*
  - [2] J. Chadwick, Nature **129**, 312 (1932), *Possible existence of a neutron.*
  - [3] R. Estermann, I. and Frisch and O. Stern, Nature **132**, 169 (1933), *Magnetic moment of the proton.*
  - [4] R. Hofstadter, H. Fechter, and J. McIntyre, Phys.Rev. **91**, 422 (1953), *Scattering of High-Energy Electrons and the Method of Nuclear Recoil.*
  - [5] R. Hofstadter, Rev.Mod.Phys. **28**, 214 (1956), *Electron scattering and nuclear structure.*
  - [6] M. Gell-Mann, Phys.Lett. **8**, 214 (1964), *A Schematic Model of Baryons and Mesons.*
  - [7] G. Zweig, *An SU(3) model for strong interaction symmetry and its breaking. Version 2* (eds D.B. Lichtenberg and S. P. Rosen, Hadronic Press, ADDRESS, 1964), p. 22.
  - [8] J. Bjorken and E. A. Paschos, Phys.Rev. **185**, 1975 (1969), *Inelastic Electron Proton and gamma Proton Scattering, and the Structure of the Nucleon.*
  - [9] R. P. Feynman, Phys.Rev.Lett. **23**, 1415 (1969), *Very high-energy collisions of hadrons.*
  - [10] B. Pire, K. Semenov-Tian-Shansky, and L. Szymanowski, Phys.Lett. **B724**, 99 (2013), *QCD description of charmonium plus light meson production in antiproton-nucleon annihilation.*
  - [11] <http://www.fair-center.eu/>.
  - [12] W. Erni *et al.*, Eur.Phys.J. **A49**, 25 (2013), *Technical Design Report for the: PANDA Straw Tube Tracker.*
  - [13] Conceptual Design Report: An International Accelerator Facility for Beams of Ions and Antiprotons, GSI, 2001.
  - [14] FAIR Baseline Technical Report, <http://www.gsi.de/fair/reports/btr.html>, 2006.
  - [15] P. Spiller *et al.*, Conf.Proc. **C070625**, 1419 (2007), *Status of the FAIR SIS100/300 synchrotron design.*
  - [16] R. Toelle *et al.*, Conf.Proc. **C070625**, 1442 (2007), *HESR at FAIR: Status of technical planning.*
  - [17] C. Dimopoulou *et al.*, [http://www-win.gsi.de/fair-eoi/PDF/TDR\\_PDF/TDR\\_NESR.pdf](http://www-win.gsi.de/fair-eoi/PDF/TDR_PDF/TDR_NESR.pdf) (2008), *Technical Design Report New Experimental Storage Ring (NESR).*
-

- [18] M. Lutz *et al.*, (2009), *Physics Performance Report for PANDA: Strong Interaction Studies with Antiprotons*.
- [19] R. Maier, D. Prasuhn, R. Stassen, H. Stockhorst, and T. Katayama, Conf.Proc. **C110904**, 3432 (2011), *Status of Stochastic Cooling Predictions at the HESR*.
- [20] W. Erni *et al.*, Technical Design Report for the PANDA Micro Vertex Detector, arXiv:1207.6581 [phys.ins-det], 2012.
- [21] W. Erni *et al.*, Technical Design Report for PANDA Electromagnetic Calorimeter (EMC), arXiv:0810.1216 [phys.ins-det], 2008.
- [22] The PANDA Collaboration: W. Erni, I. Keshelashvili, B. Krusche, M. Steinacher, Y. Heng, Z. Liu, H. Liu, X. Shen, O. Wang, H. Xu, and *et al.*, ArXiv e-prints (2009), *Technical Design Report for the PANDA Solenoid and Dipole Spectrometer Magnets*.
- [23] CMS Electromagnetic Calorimeter Group, P. Adzic, N. Almeida, D. Andelin, I. Anicin, Z. Antunovic, R. Arcidiacono, M. W. Arenton, E. Auffray, S. Argiro, and *et al.*, Journal of Instrumentation **5**, 3010 (2010), *Radiation hardness qualification of PbWO<sub>4</sub> scintillation crystals for the CMS Electromagnetic Calorimeter*.
- [24] P. Coyle, H. Kawahara, A. Lu, G. Lynch, G. Mueller, D. Muller, B. Ratcliff, and C. Simopoulos, Nuclear Instruments and Methods in Physics Research Section A: Accelerators, Spectrometers, Detectors and Associated Equipment **343**, 292 (1994), *The DIRC counter: a new type of particle identification device for B factories*.
- [25] N. Akopov *et al.*, Nuclear Instruments and Methods in Physics Research Section A: Accelerators, Spectrometers, Detectors and Associated Equipment **479**, 511 (2002), *The HERMES dual-radiator ring imaging Cherenkov detector*.
- [26] V. Khachatryan *et al.*, JHEP **1101**, 079 (2011), *Charged particle multiplicities in pp interactions at  $\sqrt{s} = 0.9, 2.36, \text{ and } 7 \text{ TeV}$* .
- [27] R. K. K. Götzen, D. Kang and F. Nerling, Present Status of the PANDA Software Trigger, <http://www-panda.gsi.de/framework/docsearch.php?subject=&notes=on>, 2014.
- [28] P. Kroll and A. Schafer, Eur. Phys. J. **A26**, 89 (2005), *The Process  $p\bar{p} \rightarrow \gamma\pi^0$  within the handbag approach*.
- [29] A. Denig and G. Salme, Prog. Part. Nucl. Phys. **68**, 113 (2013), *Nucleon Electromagnetic Form Factors in the Timelike Region*.
- [30] R. G. Sachs, Phys. Rev. **126**, 2256 (1962), *High-Energy Behavior of Nucleon Electromagnetic Form Factors*.
- [31] G. A. Miller, Phys. Rev. Lett. **99**, 112001 (2007), *Charge Density of the Neutron*.
- [32] C. E. Carlson and M. Vanderhaeghen, Phys. Rev. Lett. **100**, 032004 (2008), *Empirical transverse charge densities in the nucleon and the nucleon-to-Delta transition*.
- [33] A. Zichichi, S. M. Berman, N. Cabbibo, and R. Gatto, Nuovo Cimento **24**, 170 (1962), *Proton-antiproton annihilation into electrons, muons and vector bosons*.

- 
- [34] S. J. Brodsky and G. R. Farrar, Phys. Rev. **D11**, 1309 (1975), *Scaling Laws for Large Momentum Transfer Processes*.
- [35] E. Titchmarsh, *Theory of functions* (Oxford university Press, London, 1939), p. 179.
- [36] C. F. Perdrisat, V. Punjabi, and M. Vanderhaeghen, Prog. Part. Nucl. Phys. **59**, 694 (2007), *Nucleon electromagnetic form factors*.
- [37] V. Punjabi and C. F. Perdrisat, EPJ Web Conf. **66**, 06019 (2014), *The Proton Form Factor Ratio Measurements at Jefferson Lab*.
- [38] A. I. Akhiezer and M. P. Rekalo, Sov. Phys. Dokl. **13**, 572 (1968), *Polarization phenomena in electron scattering by protons in the high energy region*.
- [39] A. V. Belitsky, X.-D. Ji, and F. Yuan, Phys. Rev. Lett. **91**, 092003 (2003), *A perturbative QCD analysis of the nucleon's Pauli form factor  $F_2(Q^2)$* .
- [40] A. Puckett *et al.*, Phys. Rev. **C85**, 045203 (2012), *Final Analysis of Proton Form Factor Ratio Data at  $Q^2 = 4.0, 4.8$  and  $5.6 \text{ GeV}^2$* .
- [41] A. Puckett *et al.*, Phys.Rev.Lett. **104**, 242301 (2010), *Recoil Polarization Measurements of the Proton Electromagnetic Form Factor Ratio to  $Q^2 = 8.5 \text{ GeV}^2$* .
- [42] A. Gramolin *et al.*, Nucl.Phys.Proc.Suppl. **225-227**, 216 (2012), *Measurement of the two-photon exchange contribution in elastic ep scattering at VEPP-3*.
- [43] Y. M. Bystritskiy, E. A. Kuraev, and E. Tomasi-Gustafsson, Phys. Rev. **C75**, 015207 (2007), *Structure function method applied to polarized and unpolarized electron-proton scattering: A solution of the  $GE_p/GMp$  discrepancy*.
- [44] J. C. Bernauer and R. Pohl, Sci.Am. **310**, 18 (2014), *The proton radius problem*.
- [45] M. Sudol *et al.*, Eur.Phys.J. **A44**, 373 (2010), *Feasibility studies of the time-like proton electromagnetic form factor measurements with PANDA at FAIR*.
- [46] J. Lees *et al.*, Phys.Rev. **D87**, 092005 (2013), *Study of  $e^+e^- \rightarrow p\bar{p}$  via initial-state radiation at BABAR*.
- [47] G. Bardin *et al.*, Nucl. Phys. **B411**, 3 (1994), *Determination of the electric and magnetic form-factors of the proton in the timelike region*.
- [48] B. Aubert *et al.*, Phys. Rev. **D73**, 012005 (2006), *A Study of  $e^+e^- \rightarrow p\bar{p}$  using initial state radiation with BABAR*.
- [49] J. Haidenbauer, X. W. Kang, and U. G. Meiner, Nucl.Phys. **A929**, 102 (2014), *The electromagnetic form factors of the proton in the timelike region*.
- [50] V. Druzhinin, Int. J. Mod. Phys. Conf. Ser. **35**, 1460425 (2014), *Measurement of the proton electromagnetic form factors at BABAR*.
- [51] A. Dbeyssi, *Study of the internal structure of the proton with the PANDA experiment at FAIR*, PhD thesis Paris-Sud university, France, 2013.

- [52] E. Tomasi-Gustafsson, F. Lacroix, C. Duterte, and G. I. Gakh, *Eur. Phys. J.* **A24**, 419 (2005), *Nucleon electromagnetic form factors and polarization observables in space-like and time-like regions.*
- [53] M. P. Rekalov, *Soviet. Jour. of Nucl. Phys.* **1**, 760 (1965), *On a possibility of determining nucleon form factors for time-like measurements.*
- [54] J. Boucher, *Feasibility studies of the  $pp \rightarrow e^+e^+\pi^0$  electromagnetic channel at PANDA*, Paris-Sud Orsay and Johannes Gutenberg Mainz Universities, PhD thesis, 2011.
- [55] C. Adamuscin *et al.*, *Phys. Rev.* **C75**, 045205 (2007), *Testing axial and electromagnetic nucleon form factors in time-like regions in the processes  $\bar{p} + n \rightarrow \pi^- + l^- + l^+$  and  $\bar{p} + p \rightarrow \pi^0 + l^- + l^+$ ,  $l = e, \mu$ .*
- [56] H. Fonvieille and V. A. Karmanov, *Eur. Phys. J.* **A42**, 287 (2009), *Antiproton-nucleus electromagnetic annihilation as a way to access the proton timelike form factors.*
- [57] S. Boffi and B. Pasquini, *Riv.Nuovo Cim.* **30**, 387 (2007), *Generalized parton distributions and the structure of the nucleon.*
- [58] L. Frankfurt, P. Pobylitsa, M. V. Polyakov, and M. Strikman, *Phys.Rev.* **D60**, 014010 (1999), *Hard exclusive pseudoscalar meson electroproduction and spin structure of a nucleon.*
- [59] Y. Aoki, C. Dawson, J. Noaki, and A. Soni, *Phys. Rev.* **D75**, 014507 (2007), *Proton decay matrix elements with domain-wall fermions.*
- [60] B. Pire and L. Szymanowski, *Phys. Lett.* **B622**, 83 (2005), *QCD analysis of  $\bar{p} N \rightarrow \gamma^* \pi$  in the scaling limit.*
- [61] J. P. Lansberg, B. Pire, and L. Szymanowski, *Phys. Rev.* **D76**, 111502 (2007), *Production of a pion in association with a high- $Q^2$  dilepton pair in antiproton-proton annihilation at GSI- FAIR.*
- [62] J. Lansberg, B. Pire, K. Semenov-Tian-Shansky, and L. Szymanowski, *Phys. Rev.* **D85**, 054021 (2012), *A consistent model for  $\pi N$  transition distribution amplitudes and backward pion electroproduction.*
- [63] J. Lansberg, B. Pire, K. Semenov-Tian-Shansky, and L. Szymanowski, *Phys. Rev.* **D86**, 114033 (2012), *Accessing baryon to meson transition distribution amplitudes in meson production in association with a high invariant mass lepton pair at GSI-FAIR with PANDA.*
- [64] A. Kubarovskiy, *AIP Conf. Proc.* **1560**, 576 (2013), *Electroproduction of  $\pi^0$  at high momentum transfers in non-resonant region with CLAS.*
- [65] A. T. Goritschnig, S. Kofler, and W. Schweiger, *J.Phys.Conf.Ser.* **503**, 012032 (2014), *First results of proton antiproton annihilation into a pion pair at large scattering angles within the handbag approach.*
- [66] M. C. Mora Espi, *Feasibility studies for accessing nucleon structure observables with the PANDA experiment at the future FAIR facility*, 2012.
- [67] S. Spataro, *J. Phys. Conf. Ser.* **396**, 022048 (2012), *Event reconstruction in the PandaRoot framework.*

- [68] I. Hrivnacova, J. Phys. Conf. Ser. **396**, 022024 (2012), *The Geant4 virtual Monte Carlo*.
- [69] R. Brun, F. Bruyant, M. Maire, A. C. McPherson, and P. Zancarini, *GEANT 3: user's guide Geant 3.10, Geant 3.11; rev. version* (CERN, Geneva, 1987).
- [70] S. Agostinelli *et al.*, Nucl. Instrum. Meth. **A506**, 250 (2003), *GEANT4: A simulation toolkit*.
- [71] J. Allison *et al.*, IEEE Trans. Nucl. Sci. **53**, 270 (2006), *Geant4 developments and applications*.
- [72] T. Sjostrand, S. Mrenna, and P. Z. Skands, JHEP **0605**, 026 (2006), *PYTHIA 6.4 Physics and Manual*.
- [73] I. Fröhlich *et al.*, J.Phys.Conf.Ser. **219**, 032039 (2010), *Design of the Pluto Event Generator*.
- [74] I. Fröhlich *et al.*, PoS **ACAT2007**, 076 (2007), *Pluto: A Monte Carlo Simulation Tool for Hadronic Physics*.
- [75] [https://geant4.cern.ch/collaboration/working\\_groups/electromagnetic/physlist.shtml](https://geant4.cern.ch/collaboration/working_groups/electromagnetic/physlist.shtml).
- [76] [http://geant4.web.cern.ch/geant4/support/proc\\_mod\\_catalog/physics\\_lists/referencePL.shtml](http://geant4.web.cern.ch/geant4/support/proc_mod_catalog/physics_lists/referencePL.shtml).
- [77] R. E. Kalman, Journal of Basic Engineering 35 (1961), *A New Approach to Linear Filtering and Prediction Problems*.
- [78] V. Innocente, M. Maire, and E. Nagy, GEANE: Average Tracking and Error Propagation Package, CERN Program Library, 1991.
- [79] A. Fontana *et al.*, J. Phys. Conf. Ser. **119**, 032018 (2008), *Use of GEANE for tracking in virtual Monte Carlo*.
- [80] R. Kunne, Particle ID with the EMC, private communication, 2012.
- [81] M. Berger and S. Seltzer, NASA **SP 169**, 285 (1968), *Penetration of electrons and associated bremsstrahlung through aluminum targets*.
- [82] Y.-S. Tsai, Rev.Mod.Phys. **46**, 815 (1974), *Pair Production and Bremsstrahlung of Charged Leptons*.
- [83] W. Adam, R. Frühwirth, A. Strandlie, and T. Todor, (2005), *Reconstruction of Electrons with the Gaussian-Sum Filter in the CMS Tracker at the LHC*.
- [84] M. Elsing *et al.*, ATLAS Detector Paper Back-Up Note: Electrons and Photons, ATLAS NOTE, 2008.
- [85] G. P. Lepage and S. J. Brodsky, Phys. Rev. **D22**, 2157 (1980), *Exclusive Processes in Perturbative Quantum Chromodynamics*.
- [86] T. Armstrong *et al.*, Phys.Rev.Lett. **69**, 2337 (1992), *Observation of the p wave singlet state of charmonium*.
- [87] M. Andreotti *et al.*, Phys.Rev. **D72**, 032001 (2005), *Results of a search for the  $h_c^1 P_1$  state of charmonium in the  $\eta_c$  gamma and  $J/\psi\pi^0$  decay modes*.

- 
- [88] J. Van de Wiele and S. Ong, Eur. Phys. J. **C73**, 2640 (2013), *Study of associated charmonium  $J/\Psi$  production in  $\bar{p}p \rightarrow \pi^0 + J/\Psi$ .*
- [89] T. Barnes and X. Li, Phys. Rev. **D75**, 054018 (2007), *Associated Charmonium Production in Low Energy  $p$  anti- $p$  Annihilation.*
- [90] A. Lundborg, T. Barnes, and U. Wiedner, Phys. Rev. **D73**, 096003 (2006), *Charmonium production in  $p$  anti- $p$  annihilation: Estimating cross sections from decay widths.*
- [91] T. Barnes, X. Li, and W. Roberts, Phys.Rev. **D77**, 056001 (2008), *Evidence for a  $J/\psi$   $p$  anti- $p$  Pauli Strong Coupling?*
- [92] M. K. Gaillard, L. Maiani, and R. Petronzio, Phys. Lett. **B110**, 489 (1982), *Soft Pion Emission in  $p\bar{p}$  Resonance Formation.*
- [93] D. M. V. Flaminio, W.G. Moorhead and N. Rivoire, CERN-HERA **84-01**, (1984).
- [94] D. Everett *et al.*, Nucl. Phys. **B73**, 440 (1974), *High Transverse Momenta and anti- $p$   $p$  Annihilations.*
- [95] H. Braun, J.-P. Gerber, G. Maurer, A. Michalon, B. Schiby, R. Strub, and Z. Strachman, Nucl. Phys. **B95**, 481 (1975), *Isospin analysis of  $\bar{N}N \rightarrow \bar{N}N\pi$  reactions at 5.7 GeV/c.*
- [96] Capella, A. and Sukhatme, U. and Tan, C.-I. and Tran Thanh Van, J., Physics Reports **236**, 225 (1994), *Dual parton model.*
- [97] B. Andersson, G. Gustafson, and H. Pi, Z. Phys. **C57**, 485 (1993), *The FRITIOF model for very high-energy hadronic collisions.*
- [98] H. Pi, Comput. Phys. Commun. **71**, 173 (1992), *An Event generator for interactions between hadrons and nuclei: FRITIOF version 7.0.*

---

## Chapter 8

# Abstract

The multi-purpose detector  $\bar{\text{P}}\text{ANDA}$  (antiProton Annihilation at Darmstadt) will be built at the antiproton storage ring of the FAIR accelerator complex that is under construction in Darmstadt and is expected to provide its first beam in 2019. The fixed target experiment  $\bar{\text{P}}\text{ANDA}$  is a state of the art hadronic physics detector. With  $\bar{\text{P}}\text{ANDA}$ , one can explore a wide range of topics including meson spectroscopy, search for new states of matter such as glue balls and hybrids, charmed and multi-strange baryon spectroscopy, hyper-nuclei, and properties of hadrons in nuclei. Proton antiproton annihilation reactions will also allow to study the structure of nucleons, in particular by exploiting the electromagnetic channel of electron-positron pair production which is the subject of this thesis.

One major problem with studies of electromagnetic channels is the hadronic background with cross-sections at least six orders of magnitude larger than the signal, requiring excellent particle identification and good momentum resolution. However the momentum reconstruction for electrons and positrons is degraded due to the emission of Bremsstrahlung photons along their path. In the first part of this thesis, I studied this problem and developed a method based on the correction of the momentum of electrons and positrons event by event, using Bremsstrahlung photons detected in the electromagnetic calorimeter. This method, which has been integrated into PANDARoot, the official  $\bar{\text{P}}\text{ANDA}$  reconstruction code, provides a significant improvement of momentum resolution for electrons, and will be exploitable by any measurement with electron-positron pair in the exit channel.

In the second part, I performed a feasibility study of measuring the reaction  $\bar{p}p \rightarrow J/\Psi \pi^0$  using predictions from a model based on pion-nucleon TDAs (Transition Distribution Amplitudes). TDAs are non-perturbative objects that describe the transition between two particles of different nature. For example, pion-nucleon TDAs contain information about the pionic components in the nucleon's wave function. For this study, I relied on the TDA model to create an event generator, and studied the capability to reject hadronic background. The improvement of the efficiency for the signal due to the Bremsstrahlung correction method was quantified. This study can be used as basis for a proposal of an experiment with  $\bar{\text{P}}\text{ANDA}$ .

---



---

## Chapter 9

# Résumé

Le multi-détecteur  $\bar{P}$ ANDA (antiProton ANnihilation at DArmstadt) équipera lanneau de stockage dantiprotons du complexe daccélérateurs FAIR (Facility for Antiproton and Ion Research), en construction Darmstadt et dont les premiers faisceaux sont prévus en 2019. L'expérience cible fixe  $\bar{P}$ ANDA est un outil du futur pour la physique hadronique. Avec  $\bar{P}$ ANDA, on peut étudier par exemple la spectroscopie des mésons, rechercher de nouveaux états de la matière, comme les boules de glue et les hybrides, étudier la spectroscopie des baryons charmés et multi-étranges, les hypernoyaux, les hadrons dans la matière nucléaire. Les réactions d'annihilation antiproton-proton permettent aussi d'étudier la structure du nucléon, en particulier en utilisant les canaux électromagnétiques de production de paires électron-positron, qui constituent l'objet d'étude de cette thèse.

Un problème majeur de l'étude des canaux électromagnétiques, est le bruit de fond hadronique, qui est au moins six ordres de grandeur plus grand que le signal et qui nécessite une excellente identification de particules et une bonne résolution en impulsion. Or, la reconstruction de l'impulsion des électrons et positrons est dégradée par l'émission de photons de Bremsstrahlung le long de leur trace. Dans la première partie de la thèse, j'ai étudié ce problème et développé une méthode, basée sur une correction de l'impulsion des électrons et positrons événement par événement, en utilisant la détection des photons de Bremsstrahlung dans le calorimètre électromagnétique. Cette méthode, qui a été intégrée dans le code de reconstruction officiel de  $\bar{P}$ ANDA, `PANDA-root`, permet une amélioration très significative de la résolution en impulsion des électrons dont peuvent bénéficier toutes les études de canaux de production de paires électron-positron.

Dans la deuxième partie, j'ai effectué une étude de faisabilité de la mesure de la réaction  $\bar{p}p \rightarrow J/\Psi \pi^0$  dans un modèle utilisant des TDAs (Transition Distribution Amplitudes) pion-nucléon. Les TDAs sont des objets non-perturbatifs qui décrivent la transition entre deux particules différentes. Par exemple, les TDAs pion-nucléon donnent des informations sur les composantes pioniques dans la fonction d'onde du nucléon. Pour cette étude, j'ai utilisé le modèle de TDA pour créer un générateur d'événements, puis j'ai étudié les capacités de réjection du bruit de fond hadronique. L'amélioration de l'efficacité du signal, due à la méthode de correction de Bremsstrahlung a pu aussi être quantifiée. Cette étude pourra être utilisée pour une proposition d'expérience pour  $\bar{P}$ ANDA.

---